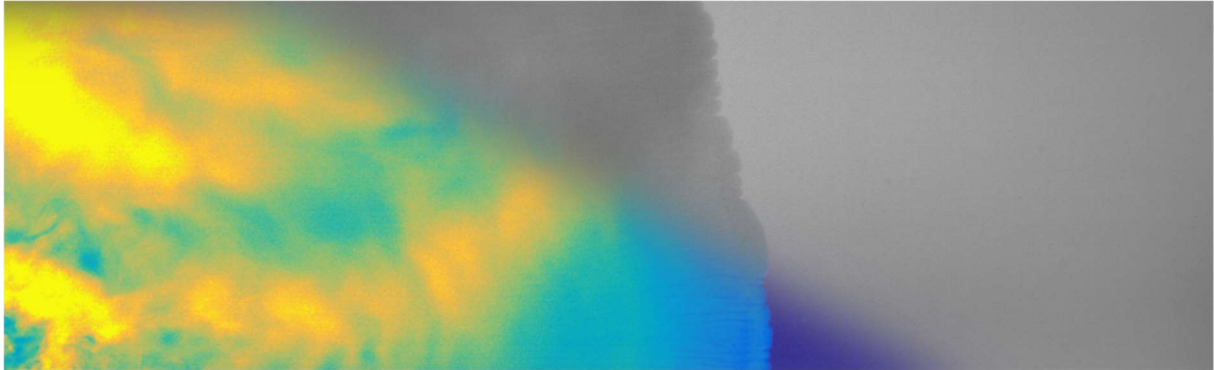




TÉCNICO
LISBOA



**The structure of gravity currents propagating in
finite domains**

Nuno Filipe Grenho Silvestre

Thesis to obtain the Master of Science Degree in

Civil Engineering

Supervisors:

Prof. Rui Miguel Lage Ferreira

Prof. Ana Fonseca Galvão

Examination Committee

Chairperson: Professor Rodrigo de Almada Cardoso Proença de Oliveira

Supervisor: Professor Rui Miguel Lage Ferreira

Member of the Committee: Doctor Ana Margarida da Costa Ricardo

July 2017

To my parents, Agostinho and Glória, and to my brother, Tomás.

Thanks for everything!

Aos meus pais, Agostinho e Glória, e ao meu irmão, Tomás.

Obrigado por tudo!

Acknowledgments

This thesis was developed at Instituto Superior Técnico - Technical University of Lisbon, Portugal and represents the end of a long journey during which I met incredible people with whom I learned a lot and whom I will never forget.

My first words of gratitude are addressed to my supervisors, Professors Rui Ferreira and Ana Galvão, whom I met in 2015 within the scope of a research initiation scholarship supported by the Portuguese Foundation for Science and Technology (FCT). Since then, several great opportunities were given to me, including the development of the present work. In particular, I would like to express my sincere gratefulness to Professor Rui Ferreira for the support, knowledge and, above all, for his constant encouragement, dedication and enthusiasm. He revealed to be such an inspiring human being and words cannot describe the immense privilege I feel for having worked with him.

I also want to express my many thanks to all the people from the Hydraulics Laboratory of the Civil Engineering Department. In particular, to João Pedro Caetano, Federica Antico, Luís Mendes, Maria João, Olga Birjukova and João Delgado for their friendly contact and fellowship. A very special word of gratitude is addressed to Pedro Sanches for his friendship and willingness to help every single day (even after he “left our flume”). More than solving a lot of problems, he always did it in a funny way with a lot of jokes and I really appreciated that good mood during our work in the laboratory.

In the same way, thank you to all those from the Hydraulics Department that were not present in the laboratory so often but also gave me support through their sound advice and friendship, especially Ana Margarida, Ricardo Canelas, Ana Quaresma and Nuno Martins. Of course, I could not fail to mention Dulce Fernandes, not only for her administrative support but also for her endless kindness and warm smile.

Among the incredible people I met in the Hydraulics Department, I would particularly like to express my gratefulness to Dora Salgueiro and Daniel Conde. Definitely, this work would not be possible without their contribution and I will never forget their friendship through which I found tremendous support and energy to keep going. I really thank them for their part in my journey.

I also want to thank my fellow colleagues and friends of Instituto Superior Técnico, namely João Paulo, João Sio, Sebastião and Stefano. We spent long (really long) hours in classes, studying, working, laughing and, in one way or another, we have been there in the good and bad moments of each other.

My most heartfelt thanks are addressed to my family for all the support and affection. In particular, I am grateful to my uncles, Jacinto and Xana, and my cousin, Ruben, for their kindness and positivity, even when things do not go as well as they should. I will always remember the enjoyable moments we have had together so far, and I will do my best to have much more in the future.

I also want to express gratitude to my godparents, Tina and Zé, for all the encouragement and trust. Likewise, to my cousin, Bruno, who will ever be my older “brother” and who, I am sure, will continue to inspire me as he always did. I would like them to know that no matter how long or how far they are away from me, I will never forget them.

My thankfulness is also addressed to my grandparents, Urbano and Joaquina, for their priceless advice and constant support. Although we cannot see each other on a daily basis, their such different life experiences have always inspired me and their example drives me to keep giving my best in everything I do. As well, to my grandmother, Maria, for the eternal affection and to my grandfather, Manuel, whose memory will last forever.

I am also grateful to my beloved girlfriend, Cristiana, for entering and changing my life in such a good (and unexpected) way. Her endless support and encouragement have been crucial during the final sprint of this roller coaster ride and I thank her for some of the best moments that I have had so far.

Last, but by no means least, I express the deepest gratitude to my parents, Agostinho and Glória, for their patience, support, guidance and love throughout my entire existence. Also to my brother, Tomás, who added a new dimension to our lives, definitely a much richer one. They are the most important figures I have in my life and nothing would be possible without them by my side.

That being said, it would take forever to thank everyone that in one way or another contributed for such an important moment in my life. To all those I have not mentioned in the lines above, my apologies and sincere thanks.

Abstract

Gravity currents are primarily horizontal flows driven by density differences between two or more contacting fluids which can be found in both natural and man-made environments. These currents have been widely studied since the second half of the XX century. However, most of the contributions have focused on the role of the density imbalance, and only recently some works have drawn attention to other factors such as the bed roughness.

The main goal of this work is to analyse the effect of complex geometries and different roughness beds in the propagation of gravity currents through laboratory experiments. These comprised a point and continuous release of a *NaCl* solution ($\rho_c = 1.027 \text{ g.cm}^{-3}$) into a tank with resting freshwater ($\rho_a = 0.999 \text{ g.cm}^{-3}$). The transport and mixing processes were assessed through image analysis techniques and Particle Image Velocimetry was employed in the study of the velocity fields.

The results showed that geometry constraints induce flow patterns that generate complex reflection waves which in turn interact with the structures at the current's front. They are also responsible for recirculation flows and zones of lower dilution. Regarding the effects of bed roughness, it can be observed a decrease in the propagation velocity in which the flow of dense fluid between the voids on the bed seems to be an important mechanism for that loss of momentum. It also induces more fragmented instability structures at the current's front.

Keywords: Gravity Currents, Geometry Effects, Bed Roughness, Image Analysis Techniques, Particle Image Velocimetry

Resumo

As correntes de densidade são escoamentos essencialmente horizontais gerados por diferenças de densidade entre dois ou mais fluidos em contacto, podendo ser encontradas quer em ambientes naturais quer antropogénicos. Estas correntes têm sido amplamente estudadas desde a segunda metade do século XX. No entanto, a maioria dos trabalhos tem-se focado na influência do gradiente de densidade e apenas recentemente alguns estudos levaram em linha de conta outros factores, tais como a rugosidade do fundo.

O principal objectivo deste trabalho é a análise dos efeitos de geometrias complexas e diferentes rugosidades de fundo na propagação de correntes de densidade através de ensaios experimentais. Estes consistiram numa descarga contínua e pontual de uma solução de $NaCl$ ($\rho_c = 1.027 \text{ g.cm}^{-3}$) num tanque com água limpa em repouso ($\rho_a = 0.999 \text{ g.cm}^{-3}$). Os processos de transporte e mistura foram estudados através de técnicas de análise de imagem e a metodologia de *Particle Image Velocimetry* foi usada no estudo dos campos de velocidade.

Os resultados mostraram que a geometria conduz a padrões de escoamento que geram ondas de reflexão complexas as quais interagem com as estruturas na frente da corrente. São também responsáveis por recirculações e zonas de menor diluição. Quanto aos efeitos da rugosidade, os resultados sugerem uma diminuição da velocidade de propagação na qual o escoamento de fluido denso por entre os vazios do fundo parece ser um mecanismo importante nessa perda de quantidade de movimento. A presença de estruturas mais fragmentadas na frente de onda mostra-se estar relacionada também com maiores rugosidades de fundo.

Palavras-chave: Correntes de Densidade, Efeitos de Geometria, Rugosidade de Fundo, Técnicas de Análise de Imagem, *Particle Image Velocimetry*

Notation

D_m	Bed particles' mean diameter	[m]
d_r	Height of the roughness layer	[m]
f_e	Fractional excess density	[kg.m ⁻³]
F_e	Depth-averaged excess density	[kg.m ⁻³]
Fr_d	Densimetric Froude number	-
g	Acceleration of gravity	[m.s ⁻²]
g'	Reduced gravitational acceleration	[m.s ⁻²]
G	Mean grey value	-
h	Ambient fluid depth	[m]
H	Depth of the current	[m]
M_c	Mass of contaminant (salt and rhodamine)	[kg]
Re	Reynolds number	-
P_i	Coefficients of the relation $M_c(G) = P_1(G - P_2)^{-P_3} - P_4$	-
q	Unit width discharge of the current	[m ² .s ⁻¹]
t	Time after the beginning of the discharge	[s]
t_0	Time of current's arrival at the far field ($x = 100$ cm)	[s]
u	Longitudinal flow velocity	[m.s ⁻¹]
U	Depth-averaged current velocity	[m.s ⁻¹]
U_f	Mean velocity of the front	[m.s ⁻¹]
w	Vertical flow velocity	[m.s ⁻¹]
x	Longitudinal spatial coordinate	[m]
x_o	Longitudinal spatial coordinate of the outlet	[m]
y	Transversal spatial coordinate	[m]
y_o	Transversal spatial coordinate of the outlet	[m]
z	Vertical spatial coordinate	[m]
z_o	Vertical spatial coordinate of the outlet	[m]
ν	Kinematic viscosity	[m ² .s ⁻¹]

Δd_x	Particle's mean longitudinal displacement	[m]
Δd_z	Particle's mean vertical displacement	[m]
$\Delta \rho$	Excess density	[kg.m ⁻³]
Δt	Time between two laser pulses	[s]
ρ_c	Density of the gravity current	[kg.m ⁻³]
ρ_a	Density of the ambient fluid	[kg.m ⁻³]

Abbreviations

CCD	Charge-coupled device
CMOS	Complementary metal-oxide semiconductor
FOV	Field of view
IA	Interrogation area
IST	Instituto Superior Técnico
LASER	Light amplification by stimulated emission of radiation
LED	Light emitting diode
PCC	Pearson correlation coefficient
PIV	Particle image velocimetry

Table of Contents

- Acknowledgments i
- Abstract iii
- Resumo..... v
- Notationvii
- Abbreviations ix
- Table of Contents xi
- List of Figuresxiii
- List of Tables.....xvii

- 1 Introduction 1**

 - 1.1 Motivation and framework.....1
 - 1.2 Proposed objectives3
 - 1.3 Thesis outline4

- 2 Literature Review 5**

 - 2.1 What is a gravity current?.....5
 - 2.1.1 Fundamental characterization.....6
 - 2.1.2 The anatomy of a gravity current7
 - 2.2 The study of gravity currents9
 - 2.3 Definition of current depth11
 - 2.4 Bed roughness effects.....12

- 3 Experimental Methodology 15**

 - 3.1 Introduction 15
 - 3.2 Experimental facility 16
 - 3.2.1 Experimental setup.....16
 - 3.2.2 Experimental procedures and parameters19
 - 3.3 Particle image velocimetry.....25
 - 3.3.1 An introduction to the PIV technique25
 - 3.3.2 System components26
 - 3.3.3 The measuring principle29

3.4	The image analysis techniques.....	32
3.4.1	Mass distribution.....	32
3.4.1.1	Apparatus	35
3.4.1.2	Calibration procedure.....	36
3.4.2	Front detection	41
3.4.2.1	Radial propagation.....	43
3.4.2.2	Linear propagation	44
3.4.3	Depth of the current	46
4	Results	49
4.1	Flow visualization in the near field.....	49
4.1.1	Initial propagation.....	49
4.1.2	Effects on the front structures	52
4.1.3	Effects on the body of the current	54
4.2	Flow visualization in the far field	55
4.2.1	The behaviour of the front.....	55
4.2.2	The structure of the current's body.....	59
5	Conclusions	63
5.1	Summary	63
5.2	Guidelines for future work	64
	References	65
	Appendices	I
	Appendix A: Spectral analysis of the discharge.....	I
	Appendix B: Calibration maps.....	II
	Appendix C: Front detection.....	V

List of Figures

Figure 1.1: Examples of gravity currents in the atmosphere: (a) “Morning Glory” clouds photographed from an airplane over the Gulf of Carpentaria on 24th August 2009 by Mick Petroff; (b) dust storm engulfing the city of Phoenix, Arizona on 29th July 2012 and (c) pyroclastic eruption in Mount Merapi, Indonesia on 26th October 2010.2

Figure 1.2: Examples of sewage discharges: (a) situation of noncompliance with wastewater discharge permits along the Mississippi River, United States of America (courtesy of Google Earth) and (b) outfall around Malé, Maldives in the Indian Ocean.3

Figure 2.1: The general shape of a bottom-boundary gravity current of density ρ_c propagating over a horizontal surface in a less dense ambient fluid of density ρ_a7

Figure 2.2: Schematic representation of the three-dimensional motion in a gravity current head (from Batt, 2008) as a result of two types of instabilities: (a) Kelvin-Helmholtz billows forming behind the head and (b) clefts with lobes forming either side (from Simpson, 1997).8

Figure 2.3: Time-evolution of lobes drawn from shadowgraph series (from Simpson, 1972).8

Figure 2.4: Main parameters used to classify gravity currents from velocity and excess density (adapted from Sequeiros et al., 2010).11

Figure 3.1: Schematic overview of the facility (a) with closer views on the discharge system (b) and the Perspex wall near the outlet (c).16

Figure 3.2: Schematic views of the tank and the Cartesian reference system herein considered.16

Figure 3.3: The rough bed configurations: (a) semi-rough with a single layer of silica beads and (b) multi-rough with three layers of particles.17

Figure 3.4: Freshwater depth, h , and height of the outlet, z_o , for the three bed configurations: (a) smooth, (b) semi-rough and (c) multi-rough. Average thickness of the roughness layers represented by d_r18

Figure 3.5: Black fabrics placed over a steel structure built around the facility (a) for user protection against the high-power light emission from the PIV laser head (b) and for control of the light conditions during the high-speed video acquisition (c).19

Figure 3.6: Near and far fields of the top view recordings performed with (a) the high-speed video camera and (b) the PIV system.....	20
Figure 3.7: Schematic location and referencing of the PIV profiles with identification of the sidewalls of the tank.....	20
Figure 3.8: Instrumentation used for mixture preparation: (a) pycnometer and (b) precision scale.	21
Figure 3.9: Time-mass variation of brine released from the discharge system for three different runs with mean flow values of 7.60 g.s^{-1} (Run 1), 7.51 g.s^{-1} (Run 2) and 7.53 g.s^{-1} (Run 3).....	23
Figure 3.10: Sketch of a PIV system installation.	26
Figure 3.11: The PIV system components: (a) laser head and lens mounted on the sliding support, (b) laser beam generator, (c) digital camera, (d) timing unit and (e) controlling software.	27
Figure 3.12: Interior arrangement of a double cavity laser head (from Raffel et al., 2007).....	28
Figure 3.13: Plausible light conditions for top view recordings of different dense fluid configurations including (a) depth variation, (b) density contrasts or (c) a combination of both depth and density gradients.....	33
Figure 3.14: Grey value variation for 16 different volumes of brine dyed with Rhodamine WT®.	34
Figure 3.15: Grey value variation for 14 different concentrations of brine with constant mass of contaminant.....	34
Figure 3.16: Mean grey value comparison for the distribution of dense fluid in two configurations: (a) stratified and (b) mixed with the ambient fluid.	35
Figure 3.17: 30-seconds plots of the three-hour long LED panel test for the analysis of the light intensity decrease.	36
Figure 3.18: Example of calibration matrix placed along the bottom of the tank (each square has an area of 1 cm^2).....	37
Figure 3.19: Schematic of the mean grey value calculation for each calibration run.	37
Figure 3.20: Sample from the near field calibration (tank filled with freshwater only).....	38
Figure 3.21: Calibration points and curve-fitting for two pixels: (a) pixel (369;1013) in the near field and (b) pixel (320;200) in the far field.....	39
Figure 3.22: Plot of the Pearson correlation coefficient for the fitted calibration curve (a) and the matching P_3 coefficient (b) in the near field region.	40

Figure 3.23: Examples of baseline (a) and in-analysis (b) images for the smooth bed in the far field.....	41
Figure 3.24: Result of the baseline and in-analysis images subtraction (a) and conversion to black and white matrixes using a threshold of 255 (b) and 250 (c).....	42
Figure 3.25: Example of binary matrix resulting from the use of a low-pass filter on the images' subtraction.	42
Figure 3.26: Ring-section for current's front detection in the near field (smooth bed example).....	43
Figure 3.27: Output from the Bresenham's algorithm for three lines with the same length and origin, although different angles. The number of pixels and the selection pattern is distinct between the three examples.....	43
Figure 3.28: Region of detection in the far field (smooth bed example).....	44
Figure 3.29: Far field's example of binary matrix used for the current's front detection.....	45
Figure 3.30: Bright-enhanced sample of a raw PIV acquisition and identification of the following elements: (1) tank's bottom, (2) gravity current, (3) ambient fluid, (4) free surface and (5) the region above.....	46
Figure 3.31: Example of algorithm failure due to empty-column (a) and outlier (b) detections.....	48
Figure 3.32: Examples of automatic profile detections comprising the head region for the smooth configuration (a) and the body of the current propagating over the semi-rough bed (b).....	48
Figure 4.1: Front detection in the near field t seconds after the beginning of the discharge (smooth bed experiments).....	49
Figure 4.2: Front's mean velocity, U_f , and its spatial distribution in the region around the discharge for the three bed configurations: (a) smooth, (b) semi-rough and (c) multi-rough.....	50
Figure 4.3: PIV acquisition along the profile EE' for: (a) $t = 11$ s and (b) $t = 12$ s.....	51
Figure 4.4: Contaminant mass distribution in the near field t seconds after the discharge.....	51
Figure 4.5: Time-width distribution of the quasi-instantaneous velocities of the front in the near field for the (a) smooth, (b) semi-rough and (c) multi-rough beds.....	53
Figure 4.6: Contaminant mass distribution in the near field t seconds after the discharge.....	54
Figure 4.7: Horizontal velocity fields in the near field t seconds after the beginning of the discharge.....	55
Figure 4.8: Front detection in the far field t seconds after the beginning of the discharge (smooth bed experiments).....	56

Figure 4.9: Mean velocity of the front, U_f , for the (a) smooth, (b) semi-rough and (c) multi-rough beds (black line represents the moving average).	56
Figure 4.10: Power spectra plots (log-log) of the front's velocity for: (a) smooth, (b) semi and (c) multi-rough beds.....	57
Figure 4.11: Time-width distribution of the quasi-instantaneous velocities of the front in the far field for the (a) smooth, (b) semi-rough and (c) multi-rough beds.....	58
Figure 4.12: Current depth evolution for the (a) smooth, (b) semi-rough and (c) multi-rough bed configurations (black line represents the moving average).....	60
Figure 4.13: Velocity fields of the current propagating in the far field (smooth bed experiments).	61
Figure A.1: Power spectra plots (log-log) of the mass variation for: (a) Run 1, (b) Run 2 and (c) Run 3..I	
Figure B.1: Plots of the coefficients P_1 (a), P_2 (b) and P_4 (c) of the calibration curves adopted in the near field.	II
Figure B.2: Plots of the coefficients P_1 (a), P_2 (b), P_3 (c) and P_4 (d) of the calibration curves adopted in the far field.....	III
Figure B.3: Plot of the Pearson correlation coefficient of the calibration curves obtained in the far field.....	IV
Figure C.1: Front detection in the near field t seconds after the beginning of the discharge (semi-rough bed).	V
Figure C.2: Front detection in the near field t seconds after the beginning of the discharge (multi-rough bed).	V
Figure C.3: Front detection in the far field t seconds after the beginning of the discharge (semi-rough bed).	VI
Figure C.4: Front detection in the far field t seconds after the beginning of the discharge (multi-rough bed).	VI

List of Tables

Table 3.1: Pycnometer volume determination and error analysis.....	22
Table 3.2: Details on the preparation of the brine dyed with rhodamine.....	22
Table 3.3: Discharge characteristics.....	24
Table 3.4: Grey value variation for different freshwater depths.....	33
Table 3.5: Calibration of the pixel (369;1013) with the mass of contaminant being expressed in mg.cm^{-2} (a) and $\times 10^{-3} \text{ mg.px}^{-2}$ (b) while the mean light intensity (c) is expressed in values of grey.....	38

Chapter 1

Introduction

1.1 Motivation and framework

A gravity current is the primarily horizontal flow driven by the difference in specific weight between two or more contacting fluids. That heterogeneity may be due to chemical composition, temperature gradients, dissolved substances, particles in suspension or a combination of these (Simpson, 1997). A wide range of gravity currents can be observed in both natural and man-made environments, from large-scale geophysical flows to small industrial applications. Simpson (1997) provides a comprehensive description and illustration of gravity currents.

In the atmosphere, sea-breeze fronts are a well-known example of these currents, playing a major role in temperature regulation along coastal regions all over the world. However, the phenomenon has other major impacts such as the distribution of airborne pollution (Lalas et al., 1983, Ding et al., 2004). In turn, katabatic winds occur when the radiative cooling of air on the top of mountains, originates a high-density cold air that flows downwards. These fall winds, as they are also known, may flow through narrow valleys and are able to reach extremely high velocities (Parish and Cassano, 2003). Its accumulation in constraining topography may lead to the formation of the so-called cold air pools. For example, La Brevine, in Switzerland, which is surrounded by the Jura Mountains, holds the lowest temperature record ($-41.8\text{ }^{\circ}\text{C}$) in Swiss Meteorological (Vitasse et al., 2016). Besides the possibility of frost damage in agricultural fields, the threat for aviation is real as an aircraft flying through these pools may experience significant effects on performance, namely a sudden decrease once out of it.

The above-mentioned examples are mesoscale phenomena that often develop in a fairly shallow stratified layer near the ground. That said, their motion often produces perturbations that might evolve over time to a series of the so-called solitons. These latter are internal gravity (or solitary) waves that can travel over large distances with minimal change in form as the result of a balance being achieved between nonlinearity and horizontal linear dispersion (Rottman and Grimshaw, 2003). A particular example is quite easy to

observe near the southern coast of the Gulf of Carpentaria, Queensland, Australia since it is made visible as a propagating roll cloud that goes by the local name of “Morning Glory” (Figure 1.1a).

Despite usually invisible, the energy involved in these atmospheric flows might be enough, for instance, to stir up dust from the ground making them both visible and heavier. As depicted in Figure 1.1b, a dust storm is a dramatic example that occurs regularly in arid regions consisting of a wall of fine particles that can reach hundreds of meters in elevation and often travelling at velocities of tens of metres per second (Doronzo et al., 2016). Atmospheric particle-laden gravity currents also include other extreme natural events such as avalanches of airborne snow and pyroclastic flows from volcanic eruptions (Figure 1.1c).



Figure 1.1: Examples of gravity currents in the atmosphere: (a) “Morning Glory” clouds photographed from an airplane over the Gulf of Carpentaria on 24th August 2009 by Mick Petroff; (b) dust storm engulfing the city of Phoenix, Arizona on 29th July 2012 and (c) pyroclastic eruption in Mount Merapi, Indonesia on 26th October 2010.

Regarding the built environment, a common example is the flow established on the opening of a room’s doorway in which the temperature is different from the outside. The geometry of the surrounding elements plays a key role in the dynamics of these air exchanges which are of much interest in the field of natural ventilation and fire safety, still being an active topic of research (Linden, 1999, Phillips and Woods, 2004, Meng et al., 2016).

Gravity currents are also present in the water masses, having multiple effects in fauna, flora, climate and geomorphology. A large-scale example is the global ocean circulation which is crucial in the maintenance of Earth’s climate. While tides and winds are responsible for part of the heat transfer that results from the uneven warming of ocean waters, the thermohaline circulation is one of the most important driving mechanisms in the formation of the so-called global ocean conveyor belt. This latter consists of currents driven by differences in density that arise from temperature (*thermo*) and salinity (*haline*) gradients, being known that the role of the ocean circulation is that of a highly nonlinear amplifier of climatic changes (Rahmstorf, 2002).

The particle-laden gravity currents in water masses are known as turbidity currents. They are often observed in rivers and lakes during floods and after intense rainfall as the flow usually denotes high

concentration of suspended sediments. When entering the receiving water basins, the decrease of the flow's velocity induces the sedimentation of those particles, leading to problems of loss of storage capacity in reservoirs and outlets/intakes clogging which have been a major subject in the research of the sustainable use of such infrastructures (Cesare et al., 2001, Oehy and Schleiss, 2007).

Density currents are also caused by human activities; some examples include oil spillage, the discharge of industrial cooling waters and outflows from wastewater treatment plants. In this latter case, the phenomenon is also due to suspended material which may have sorbed potentially harmful substances and different chemicals. As shown in Figure 1.2, these flows typically propagate in shallow river's lower courses where several infrastructures are built (e.g., ports and outfalls).



Figure 1.2: Examples of sewage discharges: (a) situation of noncompliance with wastewater discharge permits along the Mississippi River, United States of America (courtesy of Google Earth) and (b) outfall around Malé, Maldives in the Indian Ocean.

Moreover, these physical barriers can also be found in the natural environment. For example, the Mediterranean outflow at Strait of Gibraltar is an exchange flow that takes place through a constraining topography generating very important internal processes which effects on the free-surface can be seen over large distances (Morozov et al., 2002). Hence, the study of gravity currents must be supported by further investigation on the interaction between these flows and the surrounding elements (Kneller and Buckee, 2000, Theiler and Franca, 2016).

1.2 Proposed objectives

The present work aims at contributing experimentally towards the understanding of the interactions that occur when gravity currents flow in the context of finite domains and different roughness beds. Therefore, the experimental facility has been designed to comprise different stages of the current's propagation and to generate a three-dimensional flow that leads to multiple reflections in the rigid boundaries.

In this sense, the specific objectives are:

- Understand the generation mechanism of reflections waves and their development through the stratified environment;
- Assess the interactions between reflected waves and the current, namely in what concerns the instability structures at the front;
- Characterize the influence of bed roughness in the propagation of the flows that result from the interactions mentioned above.

1.3 Thesis outline

This thesis is divided in five chapters and three appendices. The present chapter provides an introduction to the topic of gravity currents focusing on the ubiquitousness of the phenomenon and its multiple effects.

The first part of chapter 2 is devoted to the fundamental characterization of these flows and the different classifications applicable. Following, a brief literature review is presented covering the typical methodologies used in laboratory experiments and the known effects of bed roughness.

Chapter 3 addresses the experimental work and it is divided in three main sections. The first is dedicated to the description of the facility and the procedures regarding the dense fluid preparation. A second part focuses on the Particle Image Velocimetry including details on the equipment and measuring principle. The last section addresses the high-speed video techniques with emphasis on the image analysis techniques developed in the scope of the present work.

The results are discussed in chapter 4 which is divided in two sections – one for each region of analysis. The first is dedicated to the study of the three-dimensional current that propagates in the first moments of the discharge and to the interactions with the geometry and the main reflection waves formed. In the second part, focus is given to the propagation of these currents over different roughness beds, providing insights on the evolution of the front and current's depth.

The last chapter summarizes the main conclusions and provides recommendations for future works.

Chapter 2

Literature Review

The present chapter is intended to provide a general overview on the topic of gravity currents being divided in four main sections. The first is devoted to the general characterization of these flows, focusing on the physical attributes and the several classifications applicable. The second section presents a brief literature review on the experimental methodologies that are typically employed in the study of gravity currents. The third part addresses the ambiguity in what concerns the current's depth definition, which is a crucial parameter in the characterization of the phenomenon. Finally, a summary on the known effects of bed roughness is provided in the fourth section. A general compilation of fundamental knowledge on gravity currents can be found in Simpson (1997) or summarised in Huppert (2006).

2.1 What is a gravity current?

Given the smallest difference in the specific weight between two or more contacting fluids, the effect of the gravity acceleration on those bodies is enough to create pressure gradients which in turn are the driving force for mainly horizontal fluid displacements, commonly known as gravity (or density) currents. When a predominant vertical motion is present, different principles of fluid mechanics are involved and that phenomenon is more naturally described as a plume (Turner, 1973). That said, since the horizontal extent of these currents is typically much larger than the vertical length scale, it allows for the application of the shallow-water theory (i.e., a hydrostatic pressure distribution can be assumed if the vertical accelerations are small with comparison to the horizontal ones) which still represents a versatile and reliable prediction for gravity flows dynamics (Ungarish, 2007).

Gravity currents can occur with both liquids and gases that are in motion or quiescent. Moreover, the density contrast can be due to a wide range of factors; regarding the nature of the driving force it is common to distinguish between compositional (or conservative) and particle-driven (non-conservative) flows. The former classification is applied when the density difference is caused by temperature or a dissolved solute (e.g., salt). In this case, the total mass of the dissolved substance is conserved and variations in density are only due to entrainment of ambient fluid. By contrast, the extra weight of

suspended sediments is the driving force of non-conservative gravity currents. Hence, deposit and incorporation of particulate material contribute to density variations (Altinakar et al., 1990). In both cases, these currents of density ρ_c propagate within an ambient fluid of different density, ρ_a , and while the present work focuses on bottom-boundary saline gravity currents, in which $\rho_c > \rho_a$, the phenomenon can also occur in the form of top currents when $\rho_c < \rho_a$ or as intrusions at some intermediate level along a plane of neutral buoyancy in a stratified fluid (Ungarish, 2009).

Further classifications may be applied; for instance, different initiation mechanisms and supply are associated with distinct flow characteristics (Piper and Normark, 2009). The turbidity currents originated during seismogenic slumpings result in surge-type unsteady phenomena in which the characteristic variables are both space and time dependent. On the other hand, a turbidity current that results from the fluvial discharge into the ocean after an intense rainfall is typically an event that lasts for days or weeks. This latter case might be considered a steady or quasi-steady phenomenon as the constant supply of denser fluid tends to balance the density reduction due to sedimentation and mixing with the ambient fluid.

2.1.1 Fundamental characterization

One fundamental parameter that characterizes the gravity current is the excess density as it controls the importance of the buoyancy force which, in turn, rules the dynamics of the current counterbalanced by the inertial and viscous forces. This parameter appears in the dimensionless numbers characterizing the current through the definition of the buoyancy reduced gravitational acceleration, g' , given by:

$$g' = g \frac{\Delta\rho}{\rho_a} = g \frac{\rho_c - \rho_a}{\rho_a} \quad (2.1)$$

where g is the acceleration of gravity. Typical values of excess density, $\Delta\rho$, range from 5 to 80 kg.m⁻³ as it is due to temperature or particle concentration differences, for instance. Regarding the inertial and viscous forces mentioned before, the dimensionless ratio between them is represented by the Reynolds number, Re, which for gravity currents reads:

$$\text{Re} = \frac{UH}{\nu} \quad (2.2)$$

where U is the depth-averaged current velocity, H is the depth of the current and ν is the kinematic viscosity of the current's fluid. According to Roscoe (1952), this latter is approximately equal to that of water since the density difference between them is taken to be small.

When the Reynolds number is much greater than one, the inertial forces dominate the viscous forces and the current is said to be inviscid. In particular, Simpson (1997) suggested that for values of Reynolds numbers greater than 1000 viscous effects are neglectable.

Gravity current can also be characterized based on their behaviour. In this sense, the densimetric Froude number, Fr_d , represents the ratio between the current speed and the speed of a long wave propagating along the interface of both fluids. At the same time, it can be seen as the ratio of the destabilizing effects of velocity shearing (inertial forces) to the stabilizing effects (gravity/buoyancy forces) of vertical density stratification (Sequeiros et al., 2010). The formulation of this parameter is based on the parameter g' (Expression 2.1) as the action of gravity in these flows depends upon the density difference between the fluids (Kneller and Buckee, 2000) and it is given by:

$$Fr_d = \frac{U}{\sqrt{g' H}} \quad (2.3)$$

2.1.2 The anatomy of a gravity current

Despite the anatomy of a gravity current can be described in broad detail, it is not possible to define a universal profile since it is particularly complex and it depends on several physical factors (Simpson, 1982). The basic shape has been discussed and developed through observations in many studies and typically two regions can be identified. At the leading edge, a sharp dividing interface between the two fluids is formed, exhibiting the so-called head. This front advances into the ambient fluid and it is followed by the body of the current which is never deeper than the former (Middleton, 1993). The head and body regions are identified in the sketch of a typical gravity current presented in Figure 2.1.

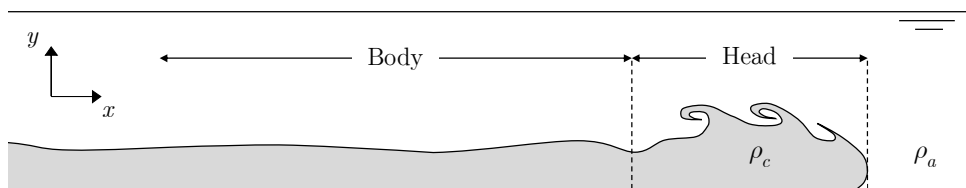


Figure 2.1: The general shape of a bottom-boundary gravity current of density ρ_c propagating over a horizontal surface in a less dense ambient fluid of density ρ_a .

At the head, a nose (the foremost point) can usually be observed raising a short distance above the ground and the following flow (Simpson, 1997). The frontal zone is characterized by a three-dimensional unsteady flow that results from shear and gravitational instabilities which in turn govern the mixing processes.

The two main modes involved are billows (resembling Kelvin-Helmholtz instabilities) and a complex shifting pattern of lobes and clefts (Simpson, 1969, 1972). These two entities are sketched in Figure 2.2.

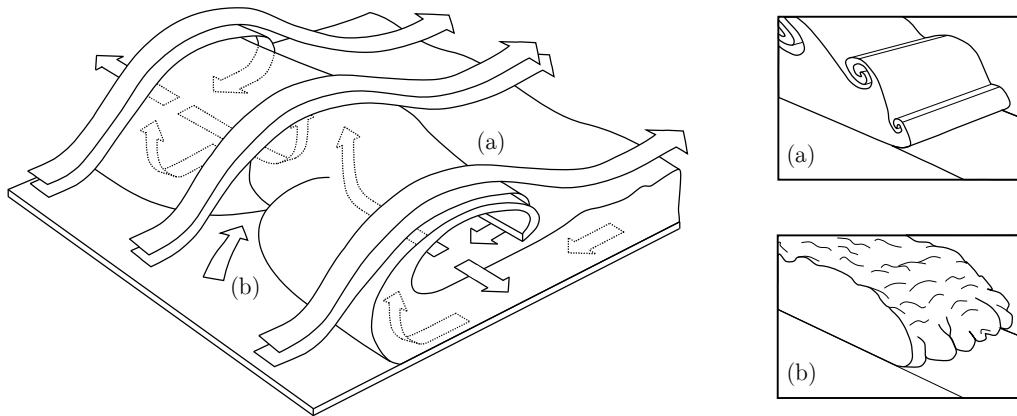


Figure 2.2: Schematic representation of the three-dimensional motion in a gravity current head (from Batt, 2008) as a result of two types of instabilities: (a) Kelvin-Helmholtz billows forming behind the head and (b) clefts with lobes forming either side (from Simpson, 1997).

Lobes and clefts result from a convective instability at the bottom boundary on the front. They are formed when the less dense ambient fluid is over-ridden by the current propagating along a no-slip lower boundary (Simpson, 1972). The buoyancy force induced by the lighter fluid forces itself upward through the gravity current causing a cleft to form. Using a shadowgraph technique, Simpson (1972) has traced the time-evolution of their formation. As shown in Figure 2.3, clefts appear by subdivision of large lobes but never disappear, being continually absorbed by neighbours.

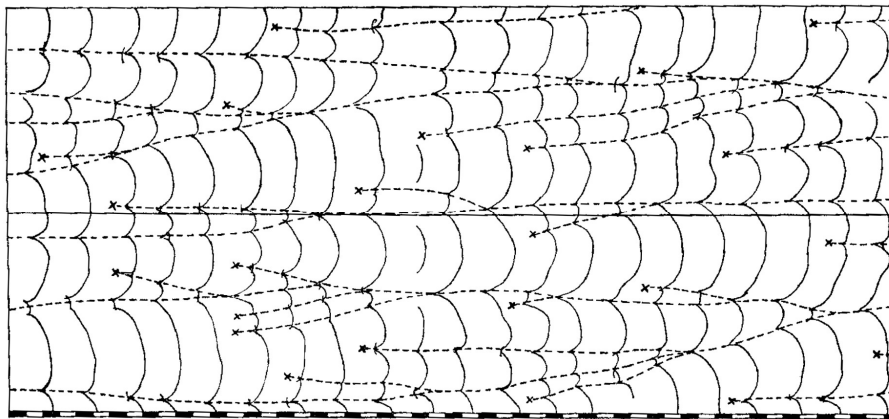


Figure 2.3: Time-evolution of lobes drawn from shadowgraph series (from Simpson, 1972).

On the other hand, Kelvin-Helmholtz billows are, in basic form, rolls of fluid along the density interface where the opposite movement induces the velocity shear. These remain quasi-steady in the current body, fading away due to continuous entrainment of ambient fluid. As established by Benjamin (1968), this latter mixing process is a consequence of the wave breaking at the rear of the head.

Britter and Simpson (1978), generated a steady state gravity current where Kelvin-Helmholtz billows were the only instability present. To do so, the cross-stream nonuniformities (lobes and clefts) were suppressed by advancing the floor beneath the head. Moreover, the front was brought to rest by an opposing uniform flow, resulting in a two-dimensional flow with regular billows. Three distinct layers have been identified in the head region: an upper layer of ambient fluid, a lower layer of undiluted dense fluid and a diluted layer in between where mixing takes place. Hallworth et al. (1996) investigated unsteady gravity currents developing over horizontal beds and observed a distinct inner structure, namely in what regards the extent of mixing. They concluded that steady gravity currents have a shorter mixing layer, near the upper boundary, while the undiluted layer below is continuously replenished by denser fluid from the tail.

2.2 The study of gravity currents

Gravity currents have been widely studied through both experimental and theoretical works since the second half of the XX century. Like what happens in other areas of science, it is expected that the main features of complex systems can be discovered by studying simpler cases. In what concerns the first approach (experimental research), most of the effort has been directed towards understanding these flows in rectangular tanks, typically with homogeneous ambient fluids that are initially at rest, or with a simple prescribed motion (Simpson, 1997).

In light of the above, a well-known technique is the so-called lock-exchange (Huppert and Simpson, 1980, Rottman and Simpson, 1983, Hacker et al., 1996, Shin et al., 2004, Cenedese et al., 2016). It consists of the sudden removal of a gate that causes the release of a fixed volume of dense fluid into another of less density. The two-dimensional (2D) flow that arises after the release exhibits a wide range of behaviours which are common to more complex gravity currents. Usually, three distinct phases can be observed: (1) the “slumping phase” during which the current develops at a constant speed and the head is formed, followed by (2) the self-similar phase governed by a buoyancy-inertia balance and (3) a final phase in which viscous effects become relevant. Since extensive research has been carried out over the years, the general dynamics of these flows are now thought to be well understood. In turn, the typical structure of gravity currents obtained with continuous releases denotes a steady flow in the body region. Therefore, they are usually performed to characterize the mean structure of the current in terms of density, velocity and turbulence (Simpson and Britter, 1979, Martin and García, 2009, Stagnaro and Pittaluga, 2014) and to study mixing processes and entrainment (Ellison and Turner, 1959, Parker et al., 1987, Cenedese and Adduce, 2010).

Apart from the release technique, some other variants have been also applied. For instance, the work of Ellison and Turner (1959) has been undertaken on different slopes and La Rocca et al. (2008) conducted laboratory experiments and numerical simulations on three-dimensional gravity currents (from an instantaneous release) developing over smooth and rough beds. As mentioned in section 1.1, real conditions are characterized by complex geometries for which reflections and other interactions may interfere with the density current propagation. Although the majority of the investigation in density currents does not take into account the effects of the receiving environment's configuration on the flow propagation.

In the laboratory environment, gravity currents are typically generated from a saline solution while freshwater is used as ambient fluid. This is a simple methodology as it produces conservative currents which density can be adjusted in a wide range by adding one of the two substances. Moreover, the viscosity of a current solution can also be increased by adding sugar to the current fluid as it has been performed by Simpson (1972). In any case, the fluids are visually similar which is not suitable for the application of photography and video capture techniques. Hence, the use of dyes or tracing particles is generally required. Regarding the former, the light attenuation promoted by the dye can be used to assess the density distribution within the gravity current (Nogueira et al., 2013b). This approach is usually applied to profile acquisitions (as the width of fluid penetrated by the light is known) and requires a calibration procedure. In what concerns the use of tracing particles, they are usually employed in techniques such as the Particle Image Velocimetry (PIV) and the Particle-Tracking Velocimetry (PTV) which are being increasingly used since the beginning of the 2000's. Despite they are typically used to investigate the inner velocity field of gravity currents (Thomas et al., 2003, Zhu et al., 2006), the combination of these methods with others such as the Laser-Induced Fluorescence (LIF) also allowed for the measurement of velocity and density simultaneously (Martin and García, 2009).

2.3 Definition of current depth

As shown before, the depth of the gravity current is a crucial parameter for the characterization of the phenomenon. However, a clear unambiguous definition remains an open question (Stacey and Bowen, 1988, Buckee et al., 2001, Shin et al., 2004). Despite the extensive research carried out since the 1950s, the most common definition is the one introduced by Ellison and Turner (1959), Parker et al. (1987), Altinakar et al. (1996), Sequeiros et al. (2010), Stagnaro and Pittaluga (2014) and Krug et al. (2015). It consists of evaluating the depth of the current as the height on which the excess density and velocity are approximated to be constant along the upward-normal to the bed, z , and respectively equal to the fractional depth-averaged excess density (F_e) and velocity (U). This definition corresponds to the solution of the following system:

$$\begin{cases} q = UH = \int_0^{\infty} u dz \\ U^2 H = \int_0^{\infty} u^2 dz \\ UF_e H = \int_0^{\infty} u f_e dz \end{cases} \quad (2.4)$$

where q is the unit width discharge of the current, u is the stream-wise flow velocity and f_e is the fractional excess density. This definition is also known as “top hat” assumption and is schematically represented in Figure 2.4 (Turner, 1973, Sequeiros et al., 2010).

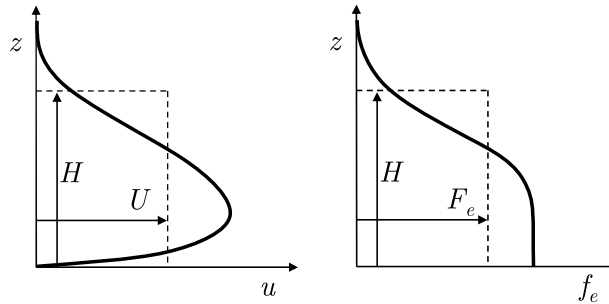


Figure 2.4: Main parameters used to classify gravity currents from velocity and excess density (adapted from Sequeiros et al., 2010).

Despite being ideally clear and convenient, this definition of current depth is not necessarily physical meaningful (Stacey and Bowen, 1988, Buckee et al., 2001, Shin et al., 2004) and may be an incorrect assumption for some flow regimes. Moreover, the computing of the integrals presented above (Expression 2.4) requires a finite value to the upper limit of the integration. Thus, since different criteria

have been applied to define that limit, the current depth definition remains ambiguous. For instance, as many experiments rely on the use of dyes to distinguish the gravity current from the colourless ambient fluid, the visual interface between them can be taken as the upper limit of the integration (Kneller et al., 1999, Lowe et al., 2002, Sequeiros et al., 2010). However, this interface is typically unstable and the mixing layer that is formed may lead to a subjective identification. Likewise, definitions based on density or velocity thresholds are also common. Stagnaro and Pittaluga (2014) set the depth of the current from the point at which the velocity is equal to 0.3 its depth-averaged value while Firoozabadi et al. (2009) consider the 1/4 of the maximum stream-wise velocity. A threshold approach is also taken by Nogueira et al. (2013a) when defining the current as the part of the flow with an excess density greater than 2%. In turn, Khavasi et al. (2012) dealt with turbidity currents and set the current-ambient interface for the points at which the particle concentration is null.

2.4 Bed roughness effects

Most of the investigation efforts deal with flows developing over smooth beds and only lately attention has been paid to the dynamics of gravity currents propagating over rough bed (Peters and Venart, 1999, Özgökmen et al., 2004, Batt, 2008, La Rocca et al., 2008, Sequeiros et al., 2010, Nogueira et al., 2013a, Bhaganagar, 2014) which is what normally occurs in nature. Peters and Venart (1999) investigated flow dynamics and mixing processes at the head of currents developing over regular square cross section elements with four different side dimensions, spanning the full width of the channel. Using a Laser-Induced Fluorescence (LIF) technique, they observed that roughness decreases the front velocity and induces higher dilution in the head region. This is due either to the additional resistance at the bottom (which promotes an earlier transition to the viscous/buoyant flow regime) or to the decrease of the buoyant driving force which is induced by the entrainment of ambient fluid trapped into the roughness spacing.

As previously touched on, with respect to the body (in which the resistance is mainly frictional), the current's head is subjected to an additional loss of energy associated with the displacement of the ambient fluid. Hence, its higher depth provides the more gravitational potential energy it needs to advance. As rough beds induce higher bottom resistance and the buoyant driving force decreases due to enhanced entrainment of ambient fluid, increases in size and mass of the head are generally observed (Hallworth et al., 1996, Peters and Venart, 1999). Moreover, large turbulence structures and billows are seen to be replaced by smaller structures so the head of the current looks shorter and less well defined (Batt, 2008). Likewise, La Rocca et al. (2008) carried out experiments with instantaneous three-dimensional gravity currents flowing over a thin layer of particles (glued to the bed) ranging from 0.7 mm

to 3.0 mm. The front velocity was seen to decrease with the increase of the mean diameter of the roughness elements. Although generally higher entrainment and dilution are associated with more rough beds, Nogueira et al. (2013a)'s results do not confirm this trend for all the roughness size. Therefore, despite previous contributions, the effect of the bed roughness in the kinematics of gravity currents is far from being completely understood.

Chapter 3

Experimental Methodology

3.1 Introduction

The present chapter provides the details for the experiments performed to assess both mass distribution and velocity fields of gravity currents propagating in confined geometries over different roughness beds. This experimental research was carried out at the Hydraulics Laboratory of Instituto Superior Técnico in Lisbon, Portugal.

The experiments comprise a point and continuous release of dense fluid (brine) into a tank of resting freshwater. The facility was designed with the aim of generating a complex three-dimensional flow pattern including shocks reflected from the rigid boundaries. Moreover, the influence of bed roughness in the dynamics of the current is assessed through three different bed configurations.

The use of a full-glass tank allows for the employment of Particle Image Velocimetry (PIV) and image analysis techniques from high-speed video recording. Both are used to measure different plan views of the phenomena, including profile and top views for two different regions (near and far from the discharge). While PIV is used with the main goal of studying the flow velocity fields, the raw images also allow for the measurement of the current depth evolution. In turn, for the high-speed video technique, a dye (Rhodamine WT[®]) is added to the *NaCl* solution and the transport and mixing processes are recorded. A pixel-by-pixel calibration method is herein fully developed and high-resolution mass distribution maps are provided. Furthermore, the same recording images are used for the current's front detection, allowing for the kinematic characterization of its propagation over the three different beds.

The experimental facility and the procedures regarding both types of measurements are detailed in section 3.2, including the main experimental parameters and a description of the runs performed. The Particle Image Velocimetry technique is presented in section 3.3, whereas section 3.4 is devoted to the image analysis techniques.

3.2 Experimental facility

3.2.1 Experimental setup

According to the overview of the installation shown in Figure 3.1, the experimental apparatus comprises the full-glass tank and support accessories, the discharge system and a tilted mirror for top view recordings.

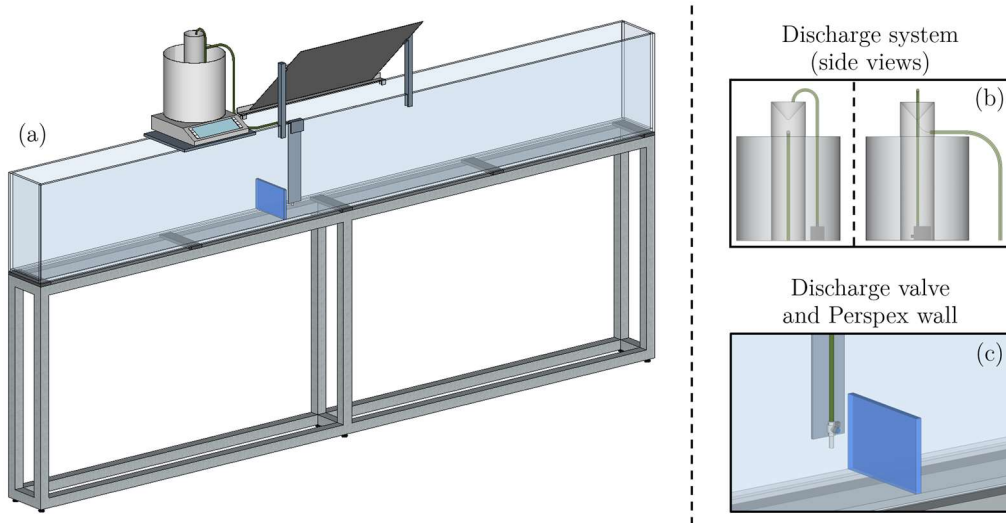


Figure 3.1: Schematic overview of the facility (a) with closer views on the discharge system (b) and the Perspex wall near the outlet (c).

The tank used for this study is 3000 mm long, 200 mm wide, 400 mm depth (outer dimensions) and it is made of 12 mm thick glass panels, allowing for a clear visualization of the gravity currents. Inside, there is a Perspex wall placed close to the outlet of the discharge system, dividing the tank in two different-length parts (see Figure 3.2). Since the experiments are performed on the longest side which has an area of $1800 \times 200 \text{ mm}^2$, the opposite one is used to support part of the accessories and the instrumentation further described in the text.

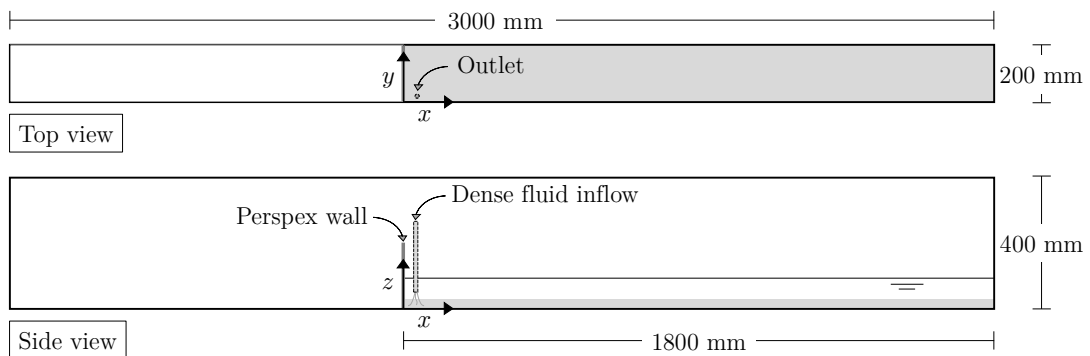


Figure 3.2: Schematic views of the tank and the Cartesian reference system herein considered.

The tank is supported by a 900-mm height steel structure with six adjustable feet that allow for keeping the tank's bottom horizontal for the duration of the experiments. Nonetheless, the present work makes use of an image analysis technique in which a LED panel is used for the illumination of the bottom. Hence, five movable Perspex bars were placed between the steel structure and the bottom glass to create “gaps” with a height of 12 mm that accommodate the LED panel and hold it in any position below the tank's bottom.

Concerning the bed roughness, three setups are tested. While the first consists of solely the tank's bottom glass panel (herein called as smooth bed), the two rough configurations result from the distribution of silica beads throughout the bottom. These particles have a mean diameter, D_m , of 3 mm and provide a quasi-transparent rough bed which is a key aspect for the application of the high-speed video techniques described in section 3.4. While one of the rough beds is formed by a single layer of beads (the so-called semi-rough bed), the second results from pilling and compacting three layers of them and it is herein named as multi-rough configuration. In both cases, the bed material was set uniformly all over the tank and particle movements or bed forms were not present for all the runs (see Figure 3.3). The average thickness of these layers, d_r , is illustrated in Figure 3.4.

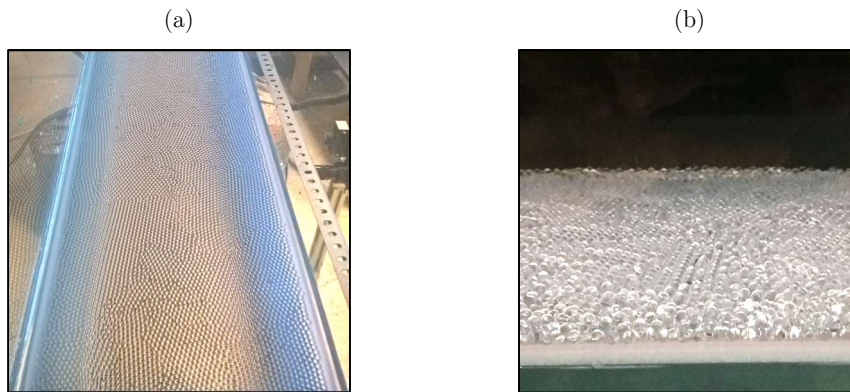


Figure 3.3: The rough bed configurations: (a) semi-rough with a single layer of silica beads and (b) multi-rough with three layers of particles.

The release of the dense fluid is performed by a discharge system (see Figure 3.1) that was developed with the aim of providing a constant flow and easy maintenance, namely for cleaning and mixture refilling operations. It comprises a bucket-like recipient that works as a supply tank with enough capacity for the volume discharged during each experiment. Inside, a pump (Heissner® P300-i) is installed and feeds a smaller concentric recipient placed 40 cm above. As this latter is connected to the outlet through a flexible pipe with 8 mm of inner diameter, an overflow (and thus a constant piezometric line) is established. The total head is about 90 cm, although the flow characteristics are detailed in section 3.2.2 below.

The outlet is placed perpendicularly to the bottom at a height, z_o , of 30 mm and its coordinates on the reference system of Figure 3.2 are $x_o = 35$ mm and $y_o = 25$ mm. Since three different types of roughness are studied, the valve support (installed in the sidewall of the tank) allows for adjustments on the vertical direction and the value of z_o is kept constant between different bed configurations¹. Likewise, the freshwater depth, h , is 50 mm as sketched in Figure 3.4. That being said, the discharge is always performed underwater, avoiding major free surface perturbations. The valve is installed above the free surface as close as possible to the outlet so that a minimum amount of air bubbles (that are eventually trapped in the short-length pipe after the body of the valve) is released during the first moments of the experiments.

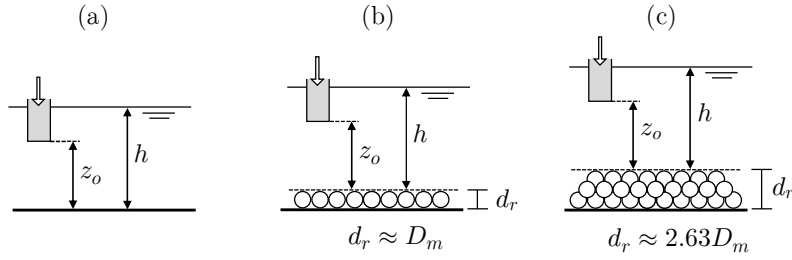


Figure 3.4: Freshwater depth, h , and height of the outlet, z_o , for the three bed configurations: (a) smooth, (b) semi-rough and (c) multi-rough. Average thickness of the roughness layers represented by d_r .

In what concerns the recording of the images with both PIV and high-speed video cameras, to take advantage of the maximum resolution of each one, the equipment must be placed considerably far from the tank. Since it was not possible to do it for top view measurements (due to structural and operational constraints), the actual solution is the use of a tilted mirror that allows for the placement of the equipment at the ground level.

The mirror has a surface area of 450×600 mm² and it is fixed to a mounting system which can be held at any point along the sidewall of the tank. However, this support does not allow for adjustments on the angle of the mirror, thus the exact top view must be achieved by adjusting the camera's position in both vertical and horizontal directions. By using the live view function available for both cameras and a glass cylinder placed in the centre of the interest area with the axis perpendicular to the bottom, the camera is correctly placed when the cylinder's borders (i.e., the two circles) were concentric in the live streaming.

¹ For the smooth bed, the value of z_o is the distance between the upper face of the bottom glass panel and the edge of the outlet. In turn, for the rough configurations, the top of the bed crests is used as the bottom reference (see Figure 3.4).

Finally, the experimental facility also includes a structure covered by black fabrics which surround all the elements mentioned above. This cover is used for user protection against the high-power light emission from the PIV system (as described in section 3.3) and to block the entering of ambient light during the calibration and recording for the image analysis techniques (detailed in section 3.4). Some photographs of the facility are shown in Figure 3.5.

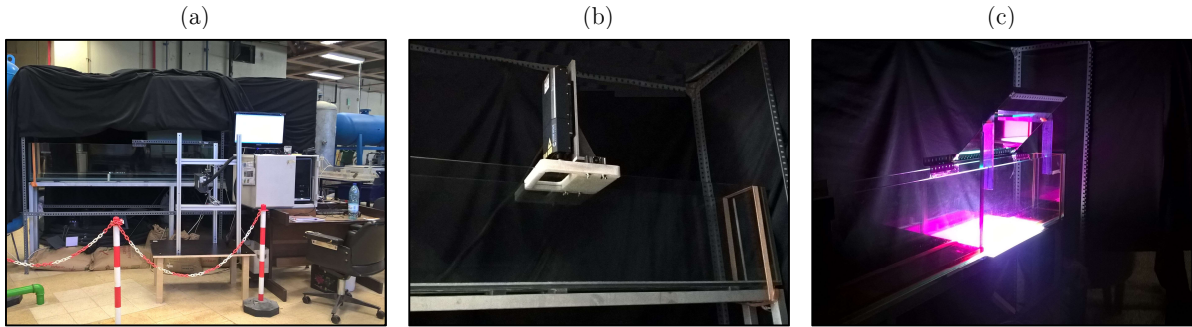


Figure 3.5: Black fabrics placed over a steel structure built around the facility (a) for user protection against the high-power light emission from the PIV laser head (b) and for control of the light conditions during the high-speed video acquisition (c).

3.2.2 Experimental procedures and parameters

According to the previous description of the facility, a highly 3D flow is present in the region of the discharge as a result of the outlet's non-symmetrical placement and the interactions of the gravity current with the surrounding walls. However, at a certain distance from the outlet, the flow is expected to be quasi-2D mainly developing along the xx direction (i.e., the length of the tank). To assess these different stages of the flow, both top view PIV and high-speed video recordings were performed in two regions, the so-called near and far fields. While the near field covers the discharge zone where the main three-dimensional events can be observed, the second field of view (FOV) starts one metre away from the Perspex wall.

In the case of the high-speed camera, each of the fields covers an area of about $60 \times 20 \text{ cm}^2$. In turn, the PIV acquisition must be performed closer to the tank and the covered area is limited to about $25 \times 20 \text{ cm}^2$. Nonetheless, as represented in Figure 3.6, the full-width of the channel can be observed in both cases.

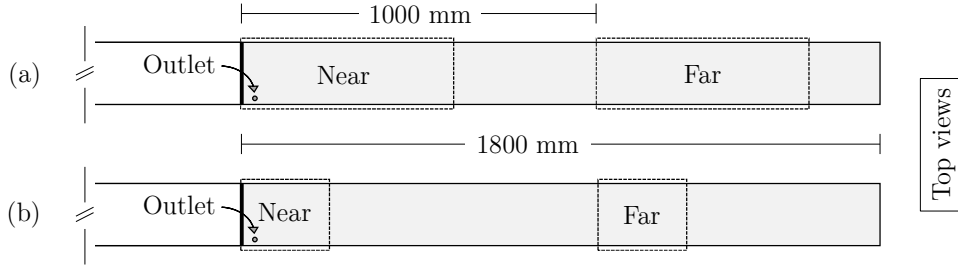


Figure 3.6: Near and far fields of the top view recordings performed with (a) the high-speed video camera and (b) the PIV system.

Regarding the dimensions above, it is important to note that, in contrast to the high-speed video recording, the PIV acquisition only comprises the “slice” of the flow that is illuminated by a thin laser sheet (see section 3.3). Therefore, when lighting the horizontal plans, the recordings must be performed sufficiently low to cross the gravity current during its propagation but also high enough to avoid the sealant along the bottom edges which have an average height of 4 mm. That said, the horizontal PIV acquisitions were performed 6 mm above the bottom² and the gravity current had a depth greater than that for all the runs during the entire duration of the experiments.

The PIV technique has been also applied for vertical acquisitions in which a mid-width profile for both near and far fields are recorded. Nonetheless, an additional section has been considered in the region of the discharge (near field) as the three-dimensional characteristics of the flow and the observed shocks on the surrounding boundaries demanded a further analysis. The coordinates of these plans are specified and schematically illustrated in Figure 3.7 while the corners of the tank have also been labelled for an easier referencing of the results.

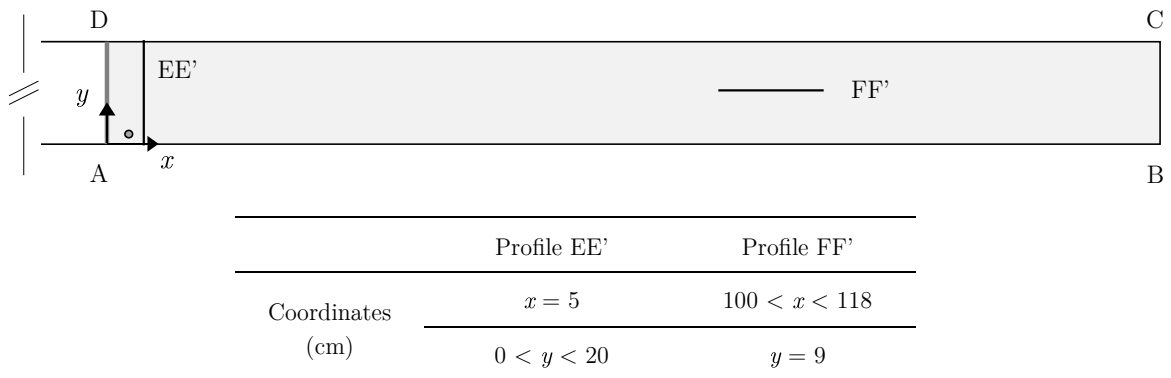


Figure 3.7: Schematic location and referencing of the PIV profiles with identification of the sidewalls of the tank.

² As mentioned for the outlet position and freshwater depth, this distance is measured from the upper face of the bottom glass (smooth bed) or from the crests of the silica beads (rough configurations).

Regarding the dense fluid (brine) that is discharged into the freshwater, two distinct volumes have been prepared (one for each technique). These mixtures differ only in the added tracers that are seeding particles for the PIV and Rhodamine WT[®] for the high-speed video recordings. In this way, when performing different experiments with the same camera, a single brine source is used and minor mixture differences due to the preparation procedures are avoided. Since both tracers were used in very small quantities, only the characterization of the mixture with rhodamine is herein presented.

Having said that, density measurements were performed through the pycnometer method. As depicted in Figure 3.8a, a pycnometer is a flask with a glass closure featuring a fine hole through so that a given volume can be accurately obtained. By measuring the mass of fluid inside this latter with a Precisa 180A[®] precision scale (Figure 3.8b) the density of the fluid could be determined with a very small error.

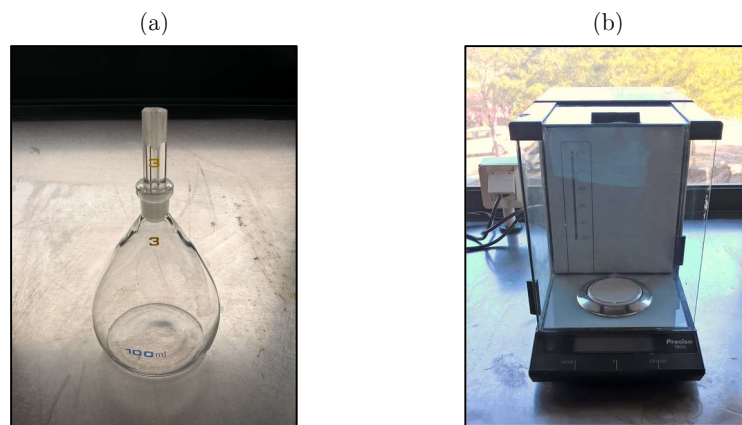


Figure 3.8: Instrumentation used for mixture preparation: (a) pycnometer and (b) precision scale.

The first step to apply this measuring technique is the determination of the pycnometer's volume. For that, an average value of the mass of the empty flask and the closure was obtained after keeping them in a dry cabinet for several hours. Then, the pycnometer was weighted with distilled water at a known temperature. Since the density of this fluid as a function of temperature is known (from Haynes, 2014), the volume of the pycnometer was found to be 95.6008 cm^3 . Table 3.1 presents the mean values and the error analysis linked to this approach. According to those records, the uncertainty about the pycnometer's volume is lower than 0.001 cm^3 for the range of temperatures operated in the laboratory (16 to 20 °C). From the reference values of the empty pycnometer's mass and volume (which are assumed to be constant), the density of other fluids can be determined by mass measuring only.

Table 3.1: Pycnometer volume determination and error analysis.

Distilled water temperature ($^{\circ}\text{C}$)	16.4 ± 0.5
Mass of the empty pycnometer (g)	39.5934 ± 0.00005
Mass of the pycnometer filled with distilled water (g)	135.0872 ± 0.00005
Mass of distilled water (g)	95.4938 ± 0.0001
Density of the distilled water ($\text{g}\cdot\text{cm}^{-3}$)	$0.99888835 < 0.99888 < 0.99887165$
Volume of the pycnometer (cm^3)	$95.5999 < 95.6008 < 95.6017$

To produce brine with a given density, freshwater and Kosher salt have been used. The density of the former was assessed through the pycnometer methodology and a mean value of $0.999 \text{ g}\cdot\text{cm}^{-3}$ was determined. For the salt, since the information from the manufacturer was not available, a value of $3.5 \text{ g}\cdot\text{cm}^{-3}$ was considered at first. Then, the salt density and the total volume of the mixture have been determined with more precision by measuring the density of the final mixture through the pycnometer methodology.

That said, the quantities used to produce around 50 L of brine dyed with the Rhodamine WT[®] and a density around $1.030 \text{ g}\cdot\text{cm}^{-3}$ (as first goal) are present in Table 3.2. As it can be seen below, the salt density was discovered to be lower, thus resulting in a higher volume of mixture (50.1 L) at a lower density ($1.027 \text{ g}\cdot\text{cm}^{-3}$).

Table 3.2: Details on the preparation of the brine dyed with rhodamine.

Freshwater density ($\text{g}\cdot\text{cm}^{-3}$)	0.999
Freshwater volume (L)	49.36
Rhodamine WT [®] density ³ ($\text{g}\cdot\text{cm}^{-3}$)	1.150
Rhodamine WT [®] volume (L)	0.005
Salt mass (g)	2132
Final density of the mixture ($\text{g}\cdot\text{cm}^{-3}$)	1.027
Final density of the salt ($\text{g}\cdot\text{cm}^{-3}$)	2.920
Final volume of the mixture (L)	50.1

The reference values above were kept for the production of the brine to be used in the PIV experiments; as previously mentioned, the rhodamine has been replaced by the seeding particles with a neglectable influence on the final density.

³ The actual value was obtained from the Keystone Aniline R&D Laboratories Technical Bulletin 89.

To ensure that the discharge system provided a constant flow, a scale has been placed below it and the temporal variation of brine mass was assessed through video recording of the values shown in the display of the scale. The mass variation for three different runs is shown in Figure 3.9.

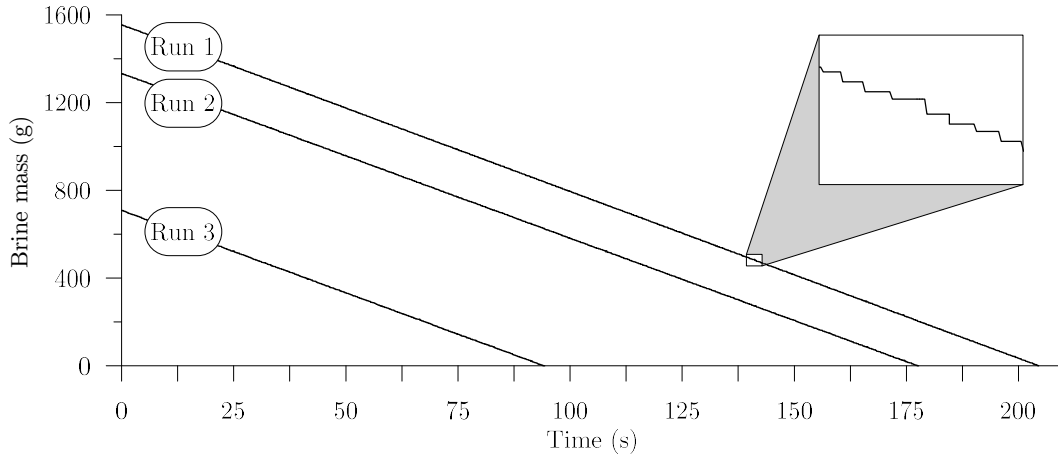


Figure 3.9: Time-mass variation of brine released from the discharge system for three different runs with mean flow values of $7.60 \text{ g}\cdot\text{s}^{-1}$ (Run 1), $7.51 \text{ g}\cdot\text{s}^{-1}$ (Run 2) and $7.53 \text{ g}\cdot\text{s}^{-1}$ (Run 3).

The mean slope of the lines plotted above suggests an average discharge of dense fluid at about $7.55 \text{ g}\cdot\text{s}^{-1}$ what leads to a combined flow rate of salt and Rhodamine WT[®] of $0.314 \text{ g}\cdot\text{s}^{-1}$. Since the refresh rate of the scale's display (2 Hz) is lower than the framerate of the video (30 fps), the output of the frame-by-frame analysis was necessarily a stepped signal as shown in the magnifier box. The non-constant mass decrease from step to step is believed to be produced by the impacts of fluid, i.e. by momentum transfer from the falling brine (caused by the overflow in the upper recipient) to the bottom of the supply tank and, consequently, to the plate of the scale. Since some oscillations on the current's front propagation have been detected (see section 4.2.1), it was necessary to characterize them and compare to the fluctuations from the discharge system. That analysis has been performed by calculating the periodogram of each signal, i.e. the significance of different frequencies, to identify any intrinsic periodic signals. The spectra for the actual discharge recordings can be found in Appendix A while those for the current's front propagation are available in section 4.2.1.

As it can be observed, the dominant spike for the current's front oscillations has a frequency of 0.2 Hz, being well marked in the three spectra (one for each type of bed). By contrast, any of the spectra regarding the discharge of dense fluid exhibits a peak for the same frequency and the overall shape of the periodogram is distinct. That being said, the oscillations of the front are believed not to be due to the discharge system.

According to the preparation of the dense mixture and the above-mentioned analysis, some discharge characteristics are summarized in Table 3.3.

Table 3.3: Discharge characteristics.

Total mass flow rate (g.s ⁻¹)	7.55
Contaminant flow rate (g.s ⁻¹)	0.314
Freshwater flow rate (g.s ⁻¹)	7.236
Outlet diameter (mm)	8.0
Cross-section area (mm ²)	50.27
Dynamic viscosity (kg.(ms) ⁻¹)	1.066×10 ⁻³
Kinematic viscosity (m ² .s ⁻¹)	1.04×10 ⁻⁶
Reynolds number (-)	1127

The dynamic viscosity was obtained from Kestin et al. (1981), based on a temperature of 20 °C, a pressure of 0.1 MPa and a molality of 0.74 mol.kg⁻¹. This latter value has been obtained from the ratio between the number of moles of salt and the mass of freshwater.

3.3 Particle image velocimetry

Particle image velocimetry (PIV) is an optical measurement technology that allows for the recording of quasi-instantaneous flow velocity fields. The technique relies on sophisticated equipment to illuminate small tracer particles within the fluid and capture their displacements in very short time periods. Due to its intrusiveness and ability to produce good results in a wide range of conditions, PIV is used in very different areas from aerodynamics to biology (Raffel et al., 2007). The aim of the present section is that of introduce the technique as it has been used in the actual experimental work. Therefore, a brief historical context precedes the description of the equipment and the details on the measuring principle.

3.3.1 An introduction to the PIV technique

PIV techniques have been applied in hydraulics since the early 1980s (Lauterborn and Vogel, 1984, Pickering and Halliwell, 1984). By measuring velocities in planar regions of the flow, PIV enables velocity measurements over a wide range of scales in length and velocity, to sense flows in more than one direction, to calculate velocity gradients and thus out-of-plane vorticity (Ferreira, 2011). According to Adrian (2005), during the early steps of the technology, the major issue concerned the energy necessary to illuminate fine particles and produce images of sufficient exposure and clarity. The use of reliable high-power light sources and advances in the fields of computer architecture and cameras promoted a significant development of the PIV technology, especially since the late 1990s (Ferreira, 2011).

In a typical PIV system, seeding particles are illuminated by a thin light sheet. Therefore, it can only measure the projection of the velocity into that plane. Since that measure is affected by perspective transformation and the out-of-plane velocity component is lost, there may be significant errors in highly three-dimensional flows (Raffel et al., 2007). For this reason, some techniques have been proposed aiming at the recovery of the third lost component, namely the stereoscopic and holographic PIV setups. Besides the employment of an additional camera (which increases the cost of the already expensive single-camera PIV systems), these approaches are not necessarily easy to implement. Details about these and other three-component PIV measurement techniques can be found in Raffel et al. (2007).

Although the setup and acquisition of raw data are relatively straightforward, PIV relies heavily on hardware and software for the synchronisation of all the instrumentation and the following data treatment.

3.3.2 System components

The description of a PIV system herein presented is based on the equipment used in the reported experimental work, which is commercialised by Dantec Dynamics[®]. In this section, a brief overview on the setup and some of the components is offered, while comprehensive reviews can be found in Raffel et al. (2007) and Tropea et al. (2007). A typical setup, as schematically represented in Figure 3.10, comprises the following elements:

- Laser head and lens (Figure 3.11a);
- Power supply or laser beam generator (Figure 3.11b);
- Digital camera (Figure 3.11c);
- Timing unit (Figure 3.11d);
- Acquisition and control software (Figure 3.11e);

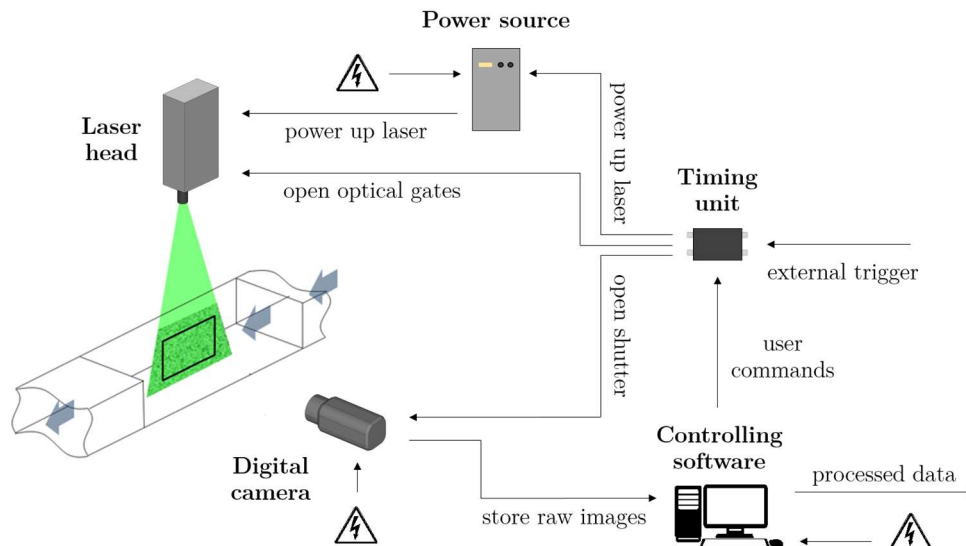


Figure 3.10: Sketch of a PIV system installation.

While the laser head emits a pulsed thin light sheet, the digital camera captures the light scattered by the particles onto subsequent image frames. For that, a timing unit is needed to ensure the synchronisation between the light emission and the image acquisition. At the same time, the production of the light is controlled by the laser beam generator which includes a water cooling system. This latter is an essential feature as stable temperatures are required due to the thermal sensitivity of some components (Raffel et al., 2007). The whole system is, usually, controlled by means of software which can also be used to perform the majority of the data treatment.

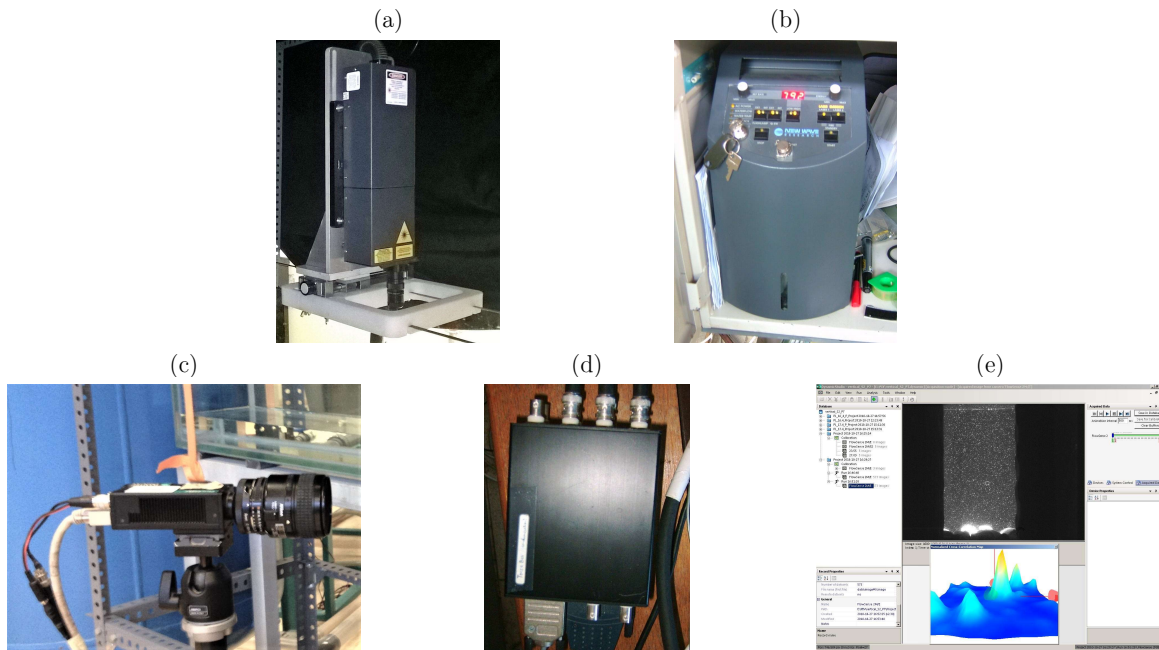


Figure 3.11: The PIV system components: (a) laser head and lens mounted on the sliding support, (b) laser beam generator, (c) digital camera, (d) timing unit and (e) controlling software.

The light source in a PIV system is a key aspect for the success of the technique. Some effort has been done in the research of an alternative solution to the laser technology (which term stands for light amplification by stimulated emission of radiation). These systems are expensive, their usage normally requires specific safety measurements and their versatility may be limited by the heavy and sensitive equipment that must be allocated. One of the alternatives is the light emitting diode (LED) technology which is being used with success in several areas of application (Willert et al., 2010). However, a laser-based solution ensures a high-energy density of monochromatic light which allows for the illumination of very small particles without chromatic aberrations.

Technically, the laser consists of a gain medium (atomic or molecular gas, semiconductor or solid material), a mechanism to energize it (also called pump source) and a resonator achieved by mirror arrangement that provides the optical feedback (Raffel et al., 2007). In this research project, it was used a double-cavity Nd:YAG laser (Neodymium-doped yttrium aluminium garnet) which is the most common type present in modern commercial PIV systems. These solid-state lasers consist of a crystalline medium that is modified (doped) with small concentrations of impurities to change its electrical properties. Despite of being sensitive to temperature, lasers subjected to optical pumping have good mechanical and thermal properties, emitting at the strongest wavelength (1064 nm) for standard operating temperatures. The actual equipment also includes a quality switch (Q-switch) inside the cavities, being operated in a software-controlled triggered mode and allowing for the production of a pulsed beam. Since Q-switches are generally associated to double oscillators, time between two consecutive flashes can be adjusted by the user independently of the pulse

strength. The emitted light which is in the infrared spectrum is not visible by human eye making it both difficult and dangerous to operate. Hence, a system of nonlinear optical materials doubles its frequency converting the infrared radiation to generally green light (532 nm) during the so-called phase matching (Raffel et al., 2007), although the use of protection goggles with green filter is mandatory. The conversion occurs in the laser head, which also comprises a system of mirrors, reflectors and shutters (as represented in Figure 3.12). They convey the laser beams to the output optics where a cylindrical lens also transforms the beam into a laser sheet that illuminates the flow field.

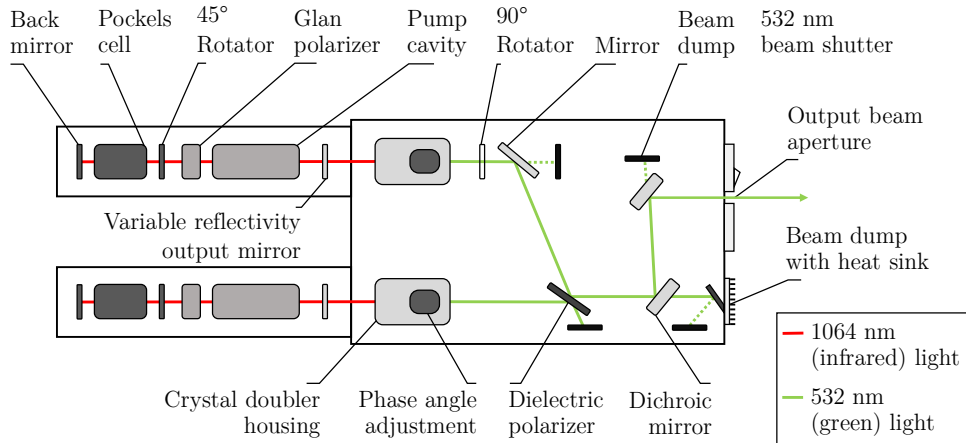


Figure 3.12: Interior arrangement of a double cavity laser head (from Raffel et al., 2007).

During the acquisition, the position of the small tracer particles is captured by a digital camera which has a direct influence on the technical possibilities of the system and the associated error sources. The most common camera's sensors are charge-coupled device (CCD) or complementary metal-oxide semiconductor (CMOS). While the former transfers, line-by-line, the charge of each pixel through the same output node, the latter has a charge-to-voltage conversion node connected to each pixel. That said, CCD sensors are relatively slow and susceptible to pixel burning due to well saturation but reliable, i.e. not prone to noise. On the other hand, CMOS devices are highly sensitive and fast but tend to be not only prone to noise but also susceptible to image deformation (Raffel et al., 2007). The system used in this research employs a Dantec Dynamics[®] 8-bit CCD camera with a resolution of 1600×1200 px² coupled to a fixed focal length lens (60 mm) as shown in Figure 3.11c. This latter is kept at a fixed perpendicular position to the laser sheet and the glass sidewalls to minimise the distortion effects.

Since the camera's sensor is only sensitive to light intensity, i.e. the amount of energy, the acquired raw images (ideally) consists of a black background with bright points representing the seeding particles. In this sense, the black fabrics cover around the facility not only improved the image contrast but also provided a much safer use of the PIV system for the user (who could stay outside during the acquisition).

The timing unit ensures the synchronisation between the light emission by the laser and the image acquisition by the camera (see Figure 3.10). This equipment is also connected to a computer through which it is possible to control a wide range of parameters regarding the laser properties, the acquisition process and the settings of the data analysis. The software used in the experiments is the DynamicStudio which, among several other options, allows for the selection of the time between two consecutive pulses, the acquisition frequency, the type of correlation in the data analysis, the size of the interrogation areas and the validation method. These terms are introduced and detailed further in this text.

3.3.3 The measuring principle

According to the aforementioned description of the PIV system, as the flow field is flashed with pulses of laser light, consecutive images are acquired. By means of evaluating the position of the seeding particles in those two instants, quasi-instantaneous velocity fields are generated. Each image is divided into small square areas known as interrogation areas (IA). Then, the displacements are obtained within each IA. In the case of a measurement parallel to the sidewalls of the tank, if the lightened particles' mean longitudinal and vertical displacements, Δd_x and Δd_z respectively, in a given IA centred at (x, z) are found, the longitudinal and vertical velocities (respectively, u and w) are determined by:

$$u(x, z) \simeq \frac{(x + \Delta d_x) - x}{\Delta t} \quad (3.1)$$

$$w(x, z) \simeq \frac{(z + \Delta d_z) - z}{\Delta t} \quad (3.2)$$

Where Δt is the time between two consecutive laser flashes, herein referred as time between pulses (Ferreira, 2011). That being said, the smaller the IA, the lower the smoothing effect and velocity fields with better spatial resolution can be obtained.

The determination of the mean planar displacements in each IA is the key issue in PIV data processing. The most likely particle displacements are determined by cross-correlation algorithms applied to the grey levels of each pair of images. A cross-correlation algorithm can be defined, in a simple way, as a statistical function that measures the degree of match between two samples for a given shift. The most straightforward approach consists in dividing each image into non-overlapping square IA with side length N and then perform the two-dimensional cross-correlation for each one.

The cross-correlation function, R , can be mathematically expressed for the preceding example by:

$$R(x, z) = \sum_{i=-M}^M \sum_{j=-N}^N I(i, j) I'(i + x, j + z) \quad (3.3)$$

where I is the light intensity level on the IA of the first image and I' is the matching level in the second frame. I is shifted around I' without extending over the edges of the latter. For each choice of sample shift (x, z) , the sum of the products of all overlapping pixel intensities produces one cross-correlation value $R(x, z)$. Note that x, z, i and j refer to the IA-centred frame of reference. According to (Raffel et al., 2007), by applying this operation for the range of shifts $-M \leq x \leq +M$ and $-N \leq z \leq +N$, a correlation plane is obtained, whose size is $(2M + 1) \times (2N + 1)$. The coordinates of the maximum value of R (the so-called correlation peak) are equal to the mean planar displacements Δd_x and Δd_z . Finally, velocity fields can be obtained since the time between pulses, Δt , is known.

While the explanation above is the simplest example of a cross-correlation algorithm application, it exposes the basics of the process required to obtain the velocity fields with the PIV technique. Correlation algorithms are constantly improving and they tend to be more complex and more efficient. Despite the wide range of algorithms available, the most common are those based on simple cross-correlation or adaptive correlation. According to Wereley and Meinhart (2000), adaptive algorithms have been gained popularity as they improve the spatial resolution while reducing velocity bias errors, in comparison to cross-correlation algorithms. The adaptive approach consists of employing a large IA that is subjected to simple cross-correlation. Then, the peak is used to re-centre (offset) a smaller IA which is again subjected to correlation. The process is repeated while an enough number of seeding particles can be distinguished in the IA. This way, the main streamlines of the flow are determined in the first steps while the last step finds the correct displacements.

Despite the use of powerful correlation algorithms, spurious velocity vectors can be obtained, namely for noisy acquisitions. Thus, to ensure good results, velocity maps are validated and optimised. The validation consists of a verisimilitude test between each vector and its neighbours. If the difference is greater than some predefined criteria, the considered erroneous vectors are replaced by interpolation of the valid neighbour vectors according to a weighted mean technique. A review on the validation methods for PIV data is presented by Westerweel (1994) and Nogueira et al. (1997).

The quality of PIV measurements depends on several aspects and the error sources can be linked to both experimental conditions or the processing method. Details on this topic are presented by Keane and Adrian (1990) and Raffel et al. (2007). In general, the major source of errors is the loss of pairs. As the name suggests, it is due to missing particles in one of the two frames. When particles are very close to the limit

of the IA, and leave or arrive in the interval between two pulses, it is called in-plane loss of pairs. One way of minimizing this effect is overlapping the interrogation areas by 25% to 75%. This way, particles that were not considered in the correlation process due to in-plane loss of pairs may be retrieved with this approach. However, it doesn't mean more accurate results inside the IA as this methodology consists of a generally oversampling that results in a denser vector map, only improving the visualisation of the flow field. By contrast, when particles enter or leave the laser sheet as a result of a highly 3D motion, that loss of pair is named out-of-plane.

The raw quality of PIV data is also controlled by three correlated parameters: the size of interrogation areas, the amount of seeding particles and the time between pulses (Δt). As previously mentioned, the size of IA defines the spatial resolution of the velocity measurements, which increases with the decrease of the IA's size. Smaller IA also improve the accuracy of measurements as they work as a filter removing the smallest scales of motion. On the other hand, in-plane loss of pairs increases for too small IA. Usually, for the adaptive correlation, a maximum displacement of particles around 25% the dimension of the final IA is recommended (Raffel et al., 2007). Regarding the amount of seeding particles, higher quantities usually have a positive impact; the drawback is that, in general, these tracers are too expensive. Finally, the time between pulses should be long enough to allow for the detection of the particles displacement and short enough to avoid both types of loss of pairs. However, even extremely careful PIV acquisitions lead to a certain percentage of outliers in the velocity maps that may be caused from inhomogeneous seeding (or light distribution), camera malfunctions, among others.

3.4 The image analysis techniques

In contrast to the PIV technology presented in section 3.3, the image analysis techniques herein described were specifically developed to the present work using algorithms performed on MATLAB® software. Since the main goal of using the high-speed video recording is the study of the mass distribution through light attenuation, focus is given to the apparatus and calibration methodology (section 3.4.1) – this technique is only applied in the smooth bed experiments.

The use of a dyed density current also allows for a kinematic analysis of the front propagation which is performed by a tracking algorithm detailed in section 3.4.2. As it makes use of the same high-speed camera images, the analysis has high temporal resolution in both regular (smooth bed) and non-regular (rough beds) backgrounds.

Finally, section 3.4.3 is devoted to the estimation of the current's depth. In this case, the detection of the density current (and the calculation of its height) is based on the seeding particles that can be observed in PIV raw images.

3.4.1 Mass distribution

The present section describes the methodology developed to assess the distribution of mass associated to the excess density of the gravity current. It consists of determining the mass of the so-called contaminant (combined salt and rhodamine) from the light intensity in the recorded images of the flow. This correlation is obtained from a pixel-by-pixel calibration which is detailed in section 3.4.1.2.

For the top view recordings mentioned in section 3.2.2 (near and far fields), a LED panel placed below the tank illuminates the flow and a high-speed video camera above captures the light transmitted through it. A key aspect of this approach is that the current depth is not directly determined. Therefore, the present technique measures the contaminant mass along verticals⁴ instead of density values. That said, mass gradients can be enhanced or vanished due to current depth variations, local density changes (e.g. by fluid compression) or a combination of both (see Figure 3.13). In this sense, the vertical PIV acquisitions aim at providing a better understanding of the data acquired with the present methodology.

⁴ The word vertical is used to illustrate the concept of a fluid column in which the top and bottom faces correspond to the square areas captured by each pixel.

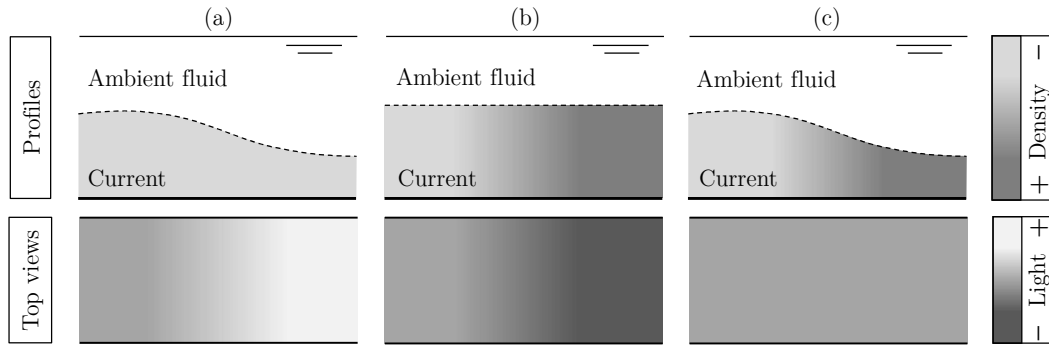


Figure 3.13: Plausible light conditions for top view recordings of different dense fluid configurations including (a) depth variation, (b) density contrasts or (c) a combination of both depth and density gradients.

The main hypothesis for the present technique is that the grey values from the images of the current are only dependent on the amount of salt and rhodamine particles in the path of the light from the panel to the camera sensor. Concerning the applicability of this approach, a set of tests were carried out.

To begin with, as the present experimental work deals with a continuous discharge of dense fluid, the final volume (dyed brine and freshwater) is slightly higher than the initial value (freshwater only). Therefore, the first test aimed at understanding if the exact same gravity current propagating in different freshwater depths yields considerable changes on light intensity. For that, the mean grey value (which results from the light intensity conversion performed by the camera's sensor), was measured for four different freshwater depths/volumes inside the tank.

Table 3.4: Grey value variation for different freshwater depths.

Volume (L)	1	1.5	2	15
Grey value (-)	173.8	171.0	169.8	166.8
Decreasing ratio (L^{-1})	(-)	-5.62	-2.43	-0.23

According to Table 3.4, a decrease of the mean grey value for higher freshwater depths can be observed. However, the ratio of that decrease is also smaller as the volume is increased inside the tank. For the range of depths and increments operated in the present work, the influence of ambient fluid in the grey value can be neglected⁵.

⁵ The volume discharged during the longest experiment (260 s) is around 1.9 L leading to a maximum depth increment inside the tank close to 0.6 cm. As the grey value decreasing ratio for the minimum depth (5 cm \approx 16 L) is lower than $0.23 L^{-1}$ (see Table 3.4), the expected maximum grey value decrease (considering the influence of the freshwater only) is $1.9 \times 0.23 \approx 0.44$. This value is smaller than the error associated to the discretization of the grey scale (which comprises integers between 0 and 255).

On the other hand, it was expected that the same test performed with dyed mixture only would lead to significant variations in the grey value. Figure 3.14 presents the result for sixteen different volumes of brine inside the tank.

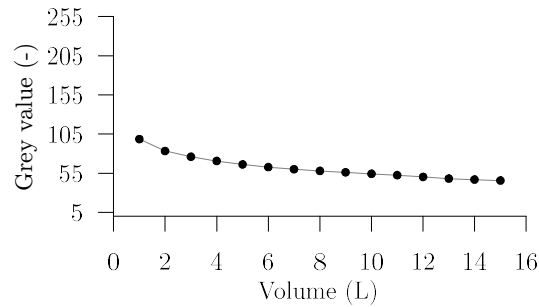


Figure 3.14: Grey value variation for 16 different volumes of brine dyed with Rhodamine WT®.

In the latter case, the mean light intensity decreases substantially when mixture volume is increased. To ensure that the grey value is a function of mass and not density, a third test was carried out. An initial volume of brine (1 L) was placed inside the tank and 1 L of freshwater has been added for 13 times. Between each dilution, the mixture has been fully mixed (to ensure homogeneity) and the grey value was recorded after the fluid was steady inside the tank. In this way, the density of the mixture was successively reduced while the mass of contaminant on each vertical remained constant.

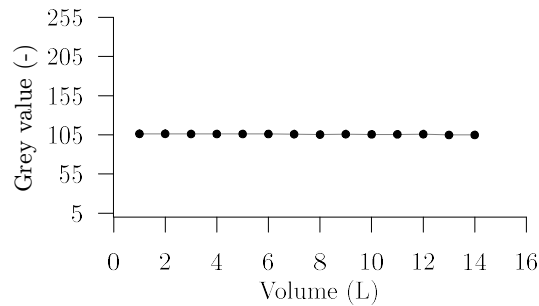


Figure 3.15: Grey value variation for 14 different concentrations of brine with constant mass of contaminant.

As shown in the plot of Figure 3.15, the grey value has minor variations for the set of 14 different mixture concentrations. Hence, one may consider that it is only dependent on the amount of Rhodamine WT® and salt particles captured by the camera. Regarding this latter conclusion, and according to the schematic example shown in Figure 3.13, it was crucial to understand if the net light intensity that arrives at the sensor would be influenced or not by the vertical distribution of those particles. Therefore, a final test has been performed in which a stratified fluid, produced by the slow release of dyed dense mixture into resting freshwater (Figure 3.16a), was recorded and compared to the result of fully mixing the same layer with the ambient fluid (Figure 3.16b). The schematic configuration and the mean grey value for both conditions are presented below.

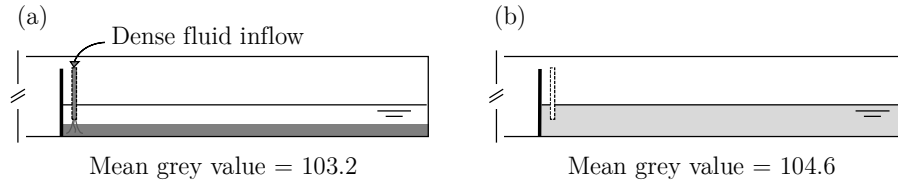


Figure 3.16: Mean grey value comparison for the distribution of dense fluid in two configurations: (a) stratified and (b) mixed with the ambient fluid.

As shown above, the result above is in accordance with the previous tests as there is no significant difference between the two configurations. That being said, mass evaluation can be performed from the analysis of the images (i.e., grey value) acquired with the high-speed camera.

3.4.1.1 Apparatus

A pixel-by-pixel approach was developed since (1) the light emission from the LED panel is not completely homogeneous and (2) the conversion from light intensity to grey values might not be exactly the same for all the pixels.

LED technology was selected for this experiment because it is a type of lighting that has reduced flickering, which has to be minimized for the present photometric methodology. The actual LED panel is 600 mm long, 300 mm wide and 11 mm deep, being installed between the tank and its support (as described in section 3.2.1). The unit produces a 6000 K colour-temperature light with a total luminous flux of about 1800 lm. Despite the benefits of LED technology, some heating is denoted when running for long-time periods. This effect reduces the panel efficiency and leads to a decrease of the light intensity which is directly denoted in the images' grey values. That said, some tests were carried out to assess this problem.

The LED panel was placed running for three hours in front of the camera at a distance similar to that of the experiments in the tank. As the LED panel was kept turned off for a long period before, it started operating at room-temperature. Using the same recording settings and the full-dark ambient provided by the black fabrics covering structure, it was possible to quantify the light decrease.

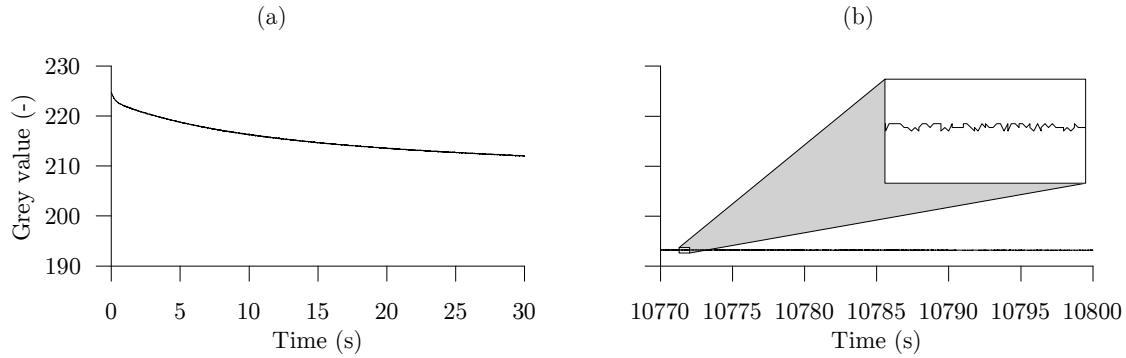


Figure 3.17: 30-seconds plots of the three-hour long LED panel test for the analysis of the light intensity decrease.

As shown in Figure 3.17a, the mean grey value decreased from 224 to 212 points during the first 30 seconds. However, as the unit gets warmer, the light intensity decrease ratio is lower. When the LED panel is operating at constant (warm) temperature, the light intensity does not decrease as it is observed in Figure 3.17b. In the end of the three-hour test, the mean grey value remained constant at 193.2 despite the noise observed in the magnifier box of Figure 3.17b. For all the experiments, since calibration is started only when the LED panel temperature is stable, the light intensity decrease has not a major influence. Moreover, the calibration is immediately followed by the experiment for which it has been performed while the unit is kept running (without interruptions, i.e., cooling). Therefore, one may consider that this effect can be neglected when applying the present technique.

Concerning the recording system, a high-speed camera and a custom-built computer are used. The camera is the AVT Bonito CL-400 set to a resolution of 2320×750 px² and a frame rate of 100 fps for all the runs. The records are performed with a fixed focal length lens (50 mm) with an aperture of F22 focused at a distance of about 1.8 m. This particular camera employs a global shutter CMOS sensor having high sensitivity due to the placement of micro lenses above each photodiode to redirect and focus the light onto the active detector regions. As mentioned before, the camera is connected to a computer which runs the software Norpix StreamPix6, enabling for the visualization, control and acquisition from the camera.

3.4.1.2 Calibration procedure

Following the tests presented in section 3.4.1, the calibration comprises several runs in which the mass of contaminant is increased by adding a known volume of dense mixture (brine with Rhodamine WT[®]) and the consequent light attenuation (i.e., grey value decrease) is analysed. In each acquisition, the mixture is uniformly spread along the tank's bottom. Thus, since the latter has been previously level, the mass of contaminant in each vertical can be assumed equal in all points.

The calibration covers a range of contaminant mass larger than that observed during the current propagation. Also, the condition of freshwater only (i.e., when the salt and rhodamine particles are not present) is calibrated for the initial depth of ambient fluid.

The first step in the calibration procedure is the calculation of the contaminant mass comprised in the area recorded by each pixel during each run. Since the area of the tank's bottom is known ($180 \times 17.5 = 31\,250 \text{ cm}^2$), the concentration of contaminant can be determined and expressed in g.cm^{-2} , for instance. The conversion of this mass per unit area to the corresponding value per pixel is done by applying a scale factor. This is obtained from a matrix of 1 cm^2 squares placed along the region captured by the camera (see Figure 3.18) and from different reference lengths (measured in pixels) a mean value for the scale factor is obtained.

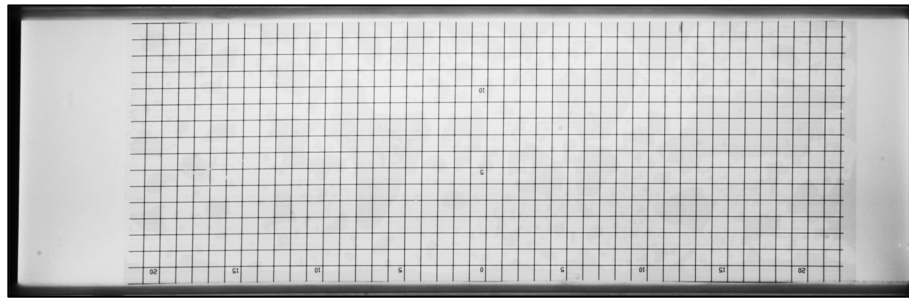


Figure 3.18: Example of calibration matrix placed along the bottom of the tank (each square has an area of 1 cm^2).

As the contaminant mass per pixel is known, the analysis of the grey attenuation is performed. For each calibration run, around 1000 images were acquired after the fluid could be considered fully steady inside the tank. Those sets of images were then used to determine the mean grey values for each pixel as it is depicted in Figure 3.19.

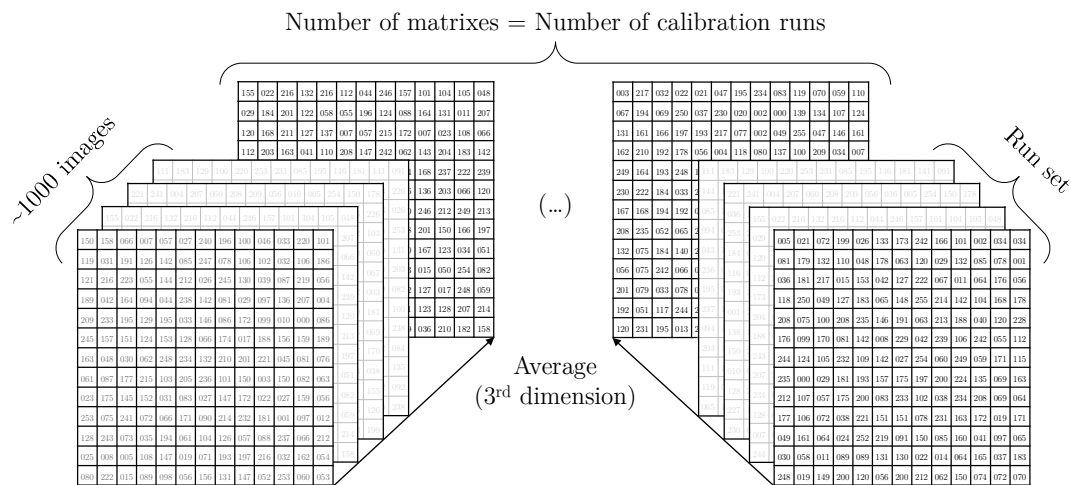


Figure 3.19: Schematic of the mean grey value calculation for each calibration run.

However, as the focal length of the camera is 50 mm, some distortion is denoted especially along the largest dimension of the image. Hence, the hypothesis of considering the exact same area for all the pixels (and consequently, the same mass of contaminant) is not fully correct. In the light of this, the procedures described above were only applied after performing distortion correction on both calibration and experiment images. To do that, a checkerboard of 1 cm² squares was placed in the study area in multiple positions and 25 images covering the entire field of view were acquired. These images were used as input in the *Camera Calibrator App* by MATLAB®, which calculates a set of distortion correction parameters. These latter are then used with the *undistortImage* function (also available in MATLAB® software) which generates the new undistorted sets of images.

That being said, taking the example of the near field, the mass of contaminant present in each pixel has a matching mean grey value which is illustrated in Table 3.5 by the cropped region shown in Figure 3.20.

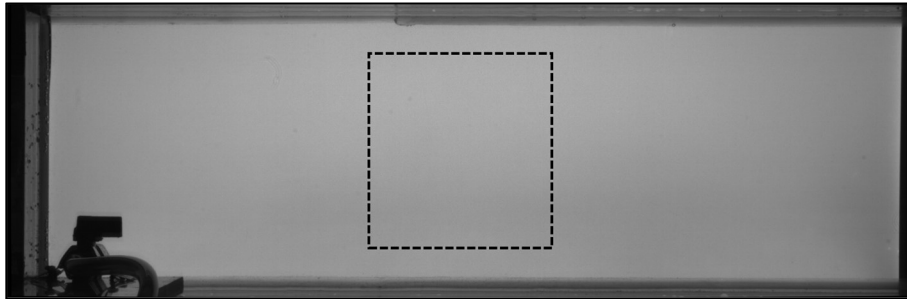


Figure 3.20: Sample from the near field calibration (tank filled with freshwater only).

Table 3.5: Calibration of the pixel (369;1013) with the mass of contaminant being expressed in mg.cm⁻² (a) and $\times 10^{-3}$ mg.px⁻² (b) while the mean light intensity (c) is expressed in values of grey.

								
(a)	0	13.55	27.09	40.64	54.19	67.74	81.28	94.83
(b)	0	8.60	17.19	25.79	34.38	42.98	51.57	60.17
(c)	160.45	101.93	86.78	78.81	73.19	68.73	64.92	61.86
								
(a)	108.38	121.93	135.47	149.02	162.57	176.11	189.66	203.21
(b)	68.76	77.36	85.95	94.55	103.15	111.74	120.34	128.93
(c)	59.17	56.68	54.40	52.46	50.70	48.96	47.35	46.04

By plotting the grey values against the mass of contaminant, the curve-fitting can be performed. According to the information shown in Table 3.5, the light attenuation is represented by a nonlinear monotonic curve as those in Figure 3.21. The first approach consisted on fitting different polynomial laws (with great results obtained for the third-degree). However, some difficulties were experienced due to the loss of the monotonic condition beyond the calibration range (which lead to erratic mass values when there was a non-single root). Also, the definition of thresholds and other validation approaches revealed to be inefficient from the computational demand point of view. That said, the generic power law given by Equation 3.4 was used. It relates the mass comprised in each pixel (M_c) and the mean grey value (G) with the same number of coefficients (P_i) as the third-degree polynomial function.

$$M_c(G) = P_1(G - P_2)^{-P_3} - P_4 \quad (3.4)$$

The curve-fitting was performed with a nonlinear least-squares solver. Despite the higher computational requirements when comparing to the polynomial function, the monotonic condition is always valid. The two examples shown in Figure 3.21 (for two pixels in the near and far fields) illustrate the accuracy of the above-mentioned function.

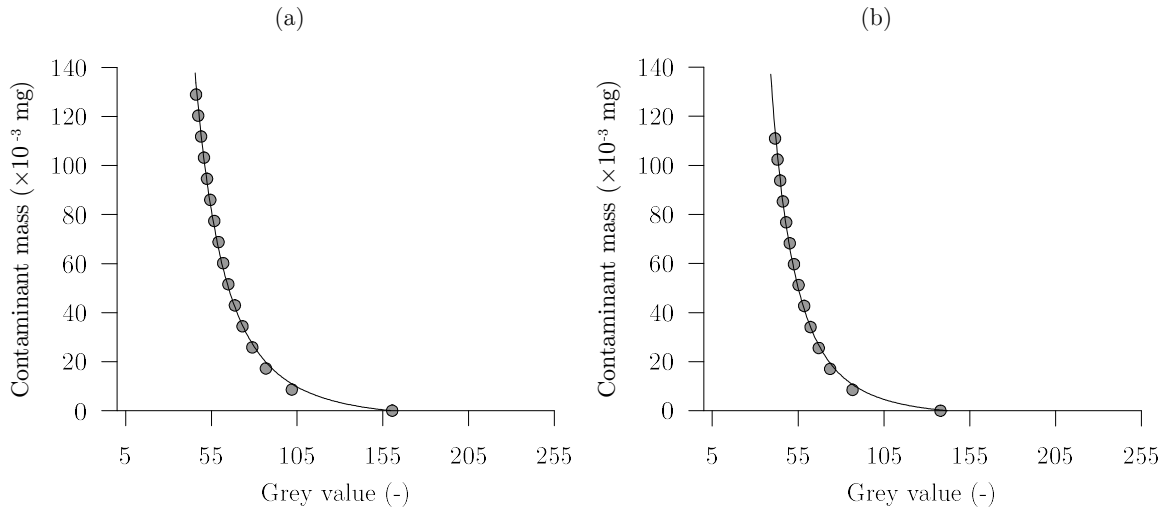


Figure 3.21: Calibration points and curve-fitting for two pixels: (a) pixel (369;1013) in the near field and (b) pixel (320;200) in the far field.

As all the aforementioned methodology is applied pixel by pixel, a large number of calculations have to be made and the overall procedure is particularly time-consuming. To minimize that, a mask is applied to both calibration and experiment images discarding all the pixels that are not comprised in the flow region. By masking those areas, the calculation time is shortened and mean statistics are not influenced by pixels out of the flow region.

Since a verification for each pixel calibration curve is not possible to be performed⁶, a visual methodology was adopted by plotting the Pearson correlation coefficient (PCC) and each P_i coefficient over the field of view. For the present example (near field), the PCC and P_3 values are shown in Figures 3.22a and b, respectively. The full set of plots including the coefficients P_1 , P_2 and P_4 for both near and far fields can be found in Appendix B.

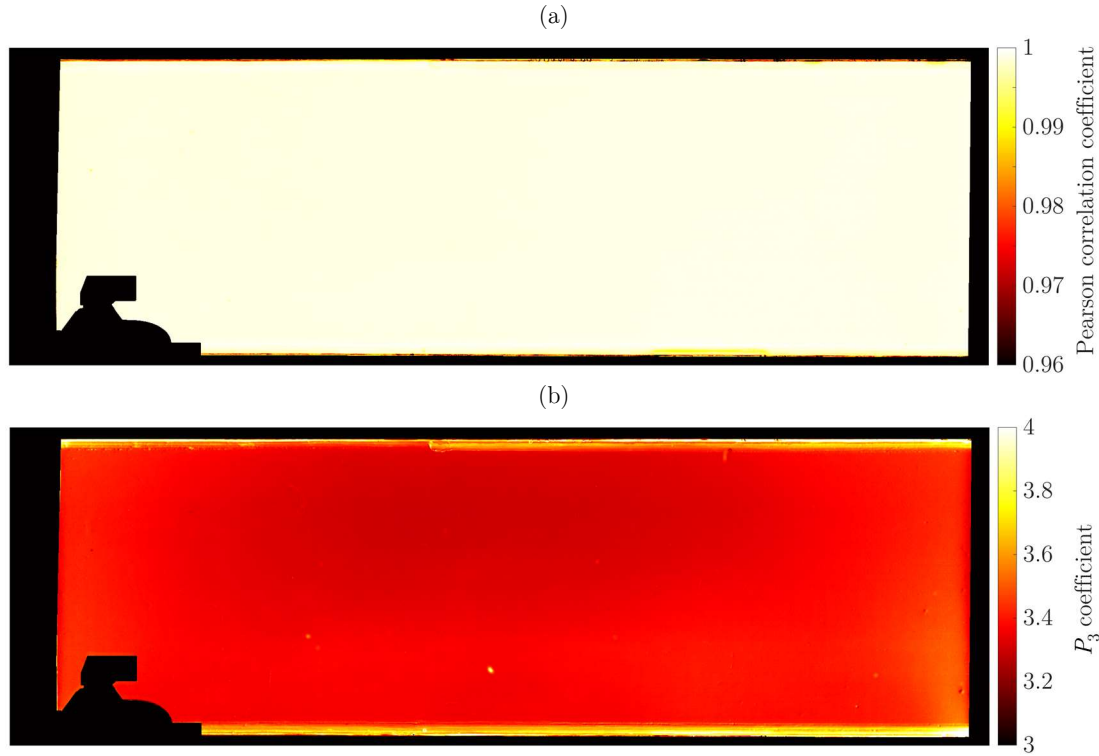


Figure 3.22: Plot of the Pearson correlation coefficient for the fitted calibration curve (a) and the matching P_3 coefficient (b) in the near field region.

As mentioned in section 3.4.1.1 and depicted in the function coefficients' maps, the conversion of grey values to mass of contaminant is not exactly the same for all pixels. Moreover, apart from the non-homogeneous light distribution, the present pixel-by-pixel calibration allows for the correction of local irregularities (marked by contrasting points on those maps). That said, and keeping the near field's example, it can be observed that the third coefficient (P_3) is comprised between 3.25 and 3.6. Similarly, coefficients P_1 and P_2 range between 75 to 125 and -13 to -10, respectively (see Appendix B). In light of this, a uniform calibration would lead to substantial deviations from the actual results. For instance, a pixel with a mean grey value of 90 would represent a mass of 9.59×10^{-3} mg in that scenario while for the pixel-by-pixel approach the output may be comprised between 0.42×10^{-3} and 35.70×10^{-3} mg.

⁶ The number of pixels processed in each image is about 1 500 000 ($2320 \times 750 = 1\,740\,000$ before masking).

3.4.2 Front detection

During the first moments of the experiments, the gravity current propagation is essentially radial. However, as the rigid walls are confining the current, the highly 3D motion gives rise to a straighter front shape (apart from the lobes and clefts formation). Actually, when the current reaches the far field, it can be considered as a quasi-2D flow. That being said, the present section is devoted to a front detection algorithm that is used in both near and far fields (i.e., when the current's propagation is either radial or linear). The technique herein detailed makes use of the raw images acquired for the mass distribution, being also based on the light attenuation caused by the dyed brine. As the high-speed video is acquired at 100 fps, it is possible to have a good estimation of the quasi-instantaneous velocity of the front over the three different bed configurations.

The first step to detect the front of the current consists of “detaching” it from all the other elements. As the tank is filled with ambient fluid since the beginning of all experiments and the recordings started before the release of the denser fluid, images of still clear water are available (Figure 3.23a). Therefore, these latter can be used as reference images (before the arrival of the current) and be subtracted to the set of images where the dyed brine can be observed, the so-called in-analysis images (Figure 3.23b). Ideally, this process should lead to a clear background with light grey zones corresponding to the density current. However, the grey variations are very small and effects like the flickering of the LED panel and the noise from the camera sensor contribute to not so accurate results, namely for the multi-rough bed configuration.

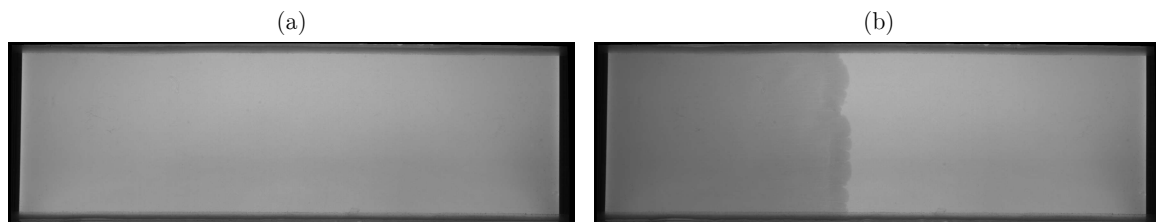


Figure 3.23: Examples of baseline (a) and in-analysis (b) images for the smooth bed in the far field.

Figure 3.24a illustrates the result of the subtraction mentioned above for a sample from the smooth bed experiments. In this example, all the pixels which difference is null (i.e., pixels that have the same grey value for both baseline and in-analysis images) are kept white with a grey value of 255. On the other hand, when the difference is not null (i.e., the difference results in a grey value lower than 255), those pixels are converted to full-black with a grey value of 0 (see Figure 3.24b). If a less sensitive threshold is chosen (considering full-white all the pixels which difference results in grey values higher than 250, for instance), the current can still be denoted while there is a substantial reduction of the noise in the ambient fluid regions (see Figure 3.24c).

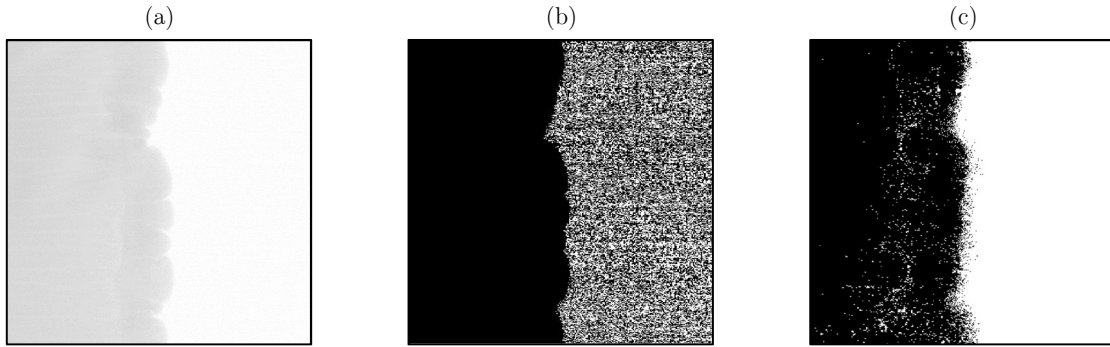


Figure 3.24: Result of the baseline and in-analysis images subtraction (a) and conversion to black and white matrixes using a threshold of 255 (b) and 250 (c).

Despite the current can be visually demarked in both cases, the front cannot be undoubtedly detected in any of them as there are some white pixels over the current (black region) or vice-versa. Hence, the last step of the “current detaching” process consists of applying a low-pass filter in which each pixel is compared to its “neighbours” and the spurious points in both white and black regions are corrected; in the present case, this moving-average takes into account the pixels comprised in a square of 12×12 px². This procedure results in images as that shown in Figure 3.25. However, the full set of frames were only processed after testing different thresholds for the subtraction (from 250 to 255 as they represent the two worst-case scenarios). This was done since for a higher threshold (when the current is fully black) the low-pass filter tends to draw the border slightly forward the actual position. By contrast, when the threshold is set to 250, the white pixels in the front region causes a slightly “delay” in the detection. That said, the most accurate results have been accomplished with a threshold of 254.

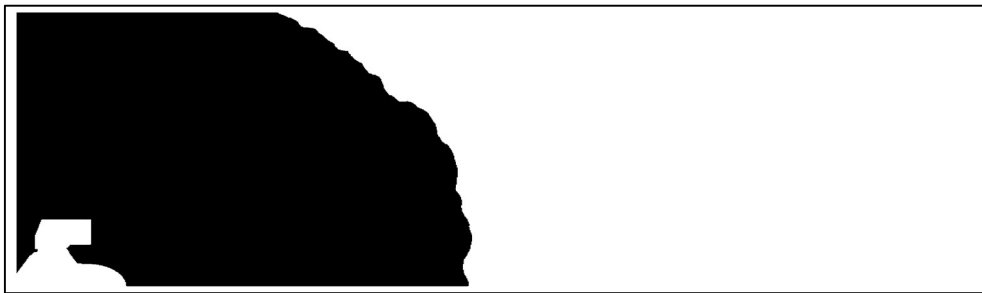


Figure 3.25: Example of binary matrix resulting from the use of a low-pass filter on the images’ subtraction.

After converting all the images in matrixes of black and white values (as shown above), the detection consists of finding a set of coordinates (x and y) along the border of the current (i.e., black region). From this point, two distinct approaches are considered. In the case of the near field, the analysis is focused only on the first moments in which the front is propagating from the valve outlet to the opposite sidewall DC (see Figure 3.7). By contrast, in the far field, where the current’s front might be considered perpendicular to the sidewalls, the detection is performed with a simpler linear method detailed further in this section.

3.4.2.1 Radial propagation

In the near field, the detection is performed inside a ring section as shown in Figure 3.26. That area is comprised by two concentric circles which centre is coincident with the valve outlet, point O , and two segments aligned with the directions xx and yy crossing that same point. In this sense, the algorithm runs in a polar coordinate system centred at O and each radius is considered to be closely aligned with the flow direction. This is a key aspect for the calculation of the quasi-instantaneous velocity as it is performed for pairs of detections along each radius.

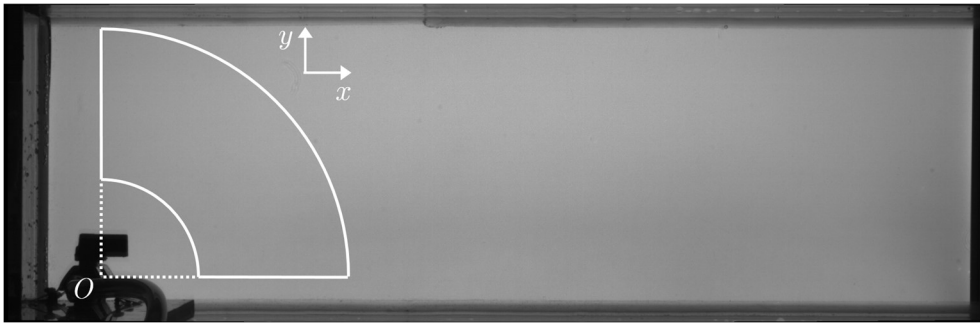


Figure 3.26: Ring-section for current's front detection in the near field (smooth bed example).

Since the images are matrixes (i.e., raster information), there is the need of determining which are the pixels that form a close approximation to a given radius. That was done through the Bresenham's line algorithm. In a simple way, when drawing an approximation of a line over a raster image, each pixel drawn will lie either exactly on the true line or to one side or the other of that line. The amount by which the pixel actually drawn deviates from the true line is the error at that point. As the line drawing progresses from one pixel to the next, the error can be used to tell when a more accurate approximation is available (by placing a given pixel one unit away from its predecessor in either the horizontal or the vertical direction, or both). A schematic illustration of the algorithm output is shown in Figure 3.27 in which three true lines with the same length and origin, although different directions, are approximated by different patterns of shadowed pixels in the background matrix.

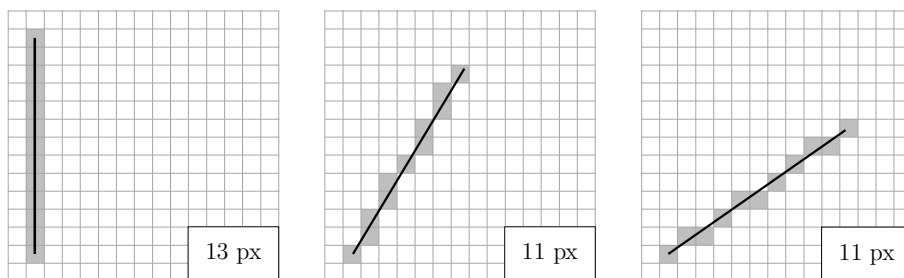


Figure 3.27: Output from the Bresenham's algorithm for three lines with the same length and origin, although different angles. The number of pixels and the selection pattern is distinct between the three examples.

Once a set of pixels is determined for a given line, the black and white values are sequentially stored in a vector from the inner to the outer circle. That done, the detection of the front is immediate; running through that vector, the front coincides with the first white pixel to be found. If only white pixels are present, it means that the current didn't arrive yet to the inner circle and the position of the front is considered to be fixed there. By contrast, when a line is full of black pixels inside the detection region, the front position is saved as if it had stopped in the limit set by the outer circle. This process is performed for all the directions in the range of analysis and the x and y coordinates of the front for a given instant are stored in two distinct vectors. Repeating the same operations for all the frames in analysis, the pair of vectors with the coordinates of the front are stored in a 3D matrix which dimensions are $d \times f \times 2$ where d is the number of directions, f is the number of frames analysed and the third dimension means the number of coordinates stored (x and y).

3.4.2.2 Linear propagation

The detection of the front in the far field is similar to the methodology previously described. However, the region of analysis is larger and the storage of the coordinates follows a simpler procedure. According to the details of the facility presented in section 3.2.1, the use of the tilted mirror allows for top view recordings in which the landscape orientation of the camera coincides with the longitudinal direction of the channel. Since the distortion correction has been performed for all the images, each line of pixels represents a parallel direction to the sidewalls of the tank. That said, the detection region in the far field is defined in the same way of the near field (i.e., two borders perpendicular to the flow direction and other two aligned with it). As shown in Figure 3.28, the top and bottom lines set the width of the front detection (being defined as close as possible to the glass sidewalls⁷) while the left and right lines set the length of the detection.

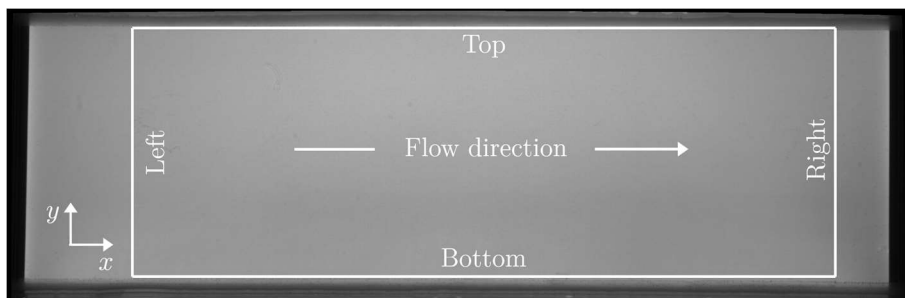


Figure 3.28: Region of detection in the far field (smooth bed example).

⁷ The tracking of the current propagating over the sealant lead to wrong results with the approach herein described. By ignoring this region, the front length has been reduced in about 3% on each side.

By using the reference grid in the bottom of the tank (see Figure 3.18), the distance between the left and right lines is kept constant (45 cm) with the first, i.e. the upstream edge, being one metre away from the Perspex wall (AD). Likewise, the conversion of the original images to the matrixes of black and white values follows the exact same steps detailed above and a sample of the final result for the far field is shown in Figure 3.29.

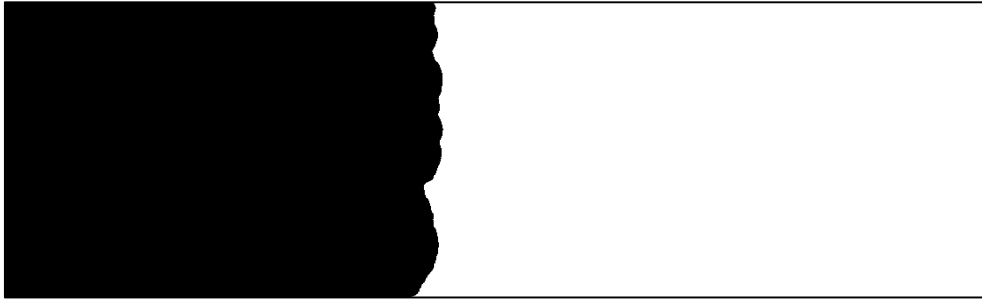


Figure 3.29: Far field's example of binary matrix used for the current's front detection.

Regarding the procedure to find the coordinates of the front, some simplifications can be taken into account. As depicted in the image above, the overall shape of the front can be considered perpendicular to the sidewalls of the tank. Hence, the lines of the image are aligned with the flow direction along which the detection is performed. In this sense, the position of the front over the time can be stored in a single 2D matrix⁸ which dimensions are $f \times l$ with f being the number of frames analysed and l the number of lines (i.e., the width of the current in pixels). As it has been done for the near field analysis, the detection process starts before the current arrives at the detection region and only finishes after the front is fully outside of it.

Finally, each detected line (i.e., set of points) was plotted over the matching original image. This approach has been performed for the whole set of frames which were later compiled in video, allowing for a visual validation of the algorithm's performance. Samples for the near field (radial propagation) can be observed in section 4.1.1 while the far field detection is represented in section 4.2.1. Both examples refer to the smooth configuration, although a similar set for the semi and multi-rough beds is available in Appendix C.

⁸ Since the analysis is performed line-by-line, only x coordinates are stored in this matrix while the matching y coordinate is implicit in the line index.

3.4.3 Depth of the current

As presented in section 2.3, the definition for the depth of a gravity current is an ambiguous topic as it can be assessed from density contrasts, colour gradients, among others. In the present work, the current's depth can be only determined from profile views of the flow which were acquired with the PIV technique. That being said, since tracer particles have been added solely to the dense fluid that produces the gravity current, a new methodology for the definition of its depth is proposed; it consists of evaluating the upper boundary of the current as the lowest limit above which there is only ambient fluid and below which seeding particles can still be observed.

As the ambient fluid is not seeded, the entrainment of freshwater into the current necessarily imposes a sparser distribution of tracing particles in the denser region. Hence, it is assumed that seeding is present in a concentration that is high enough to accommodate this reduction, still allowing for its detection. Moreover, it is considered that the reverse process (detrainment) is sufficiently low and the tracing material is not transported from the current to the ambient fluid. In any case, and according to the methodology described in the following lines, the algorithm runs along regions which are expected to comprise a minimum number of particles. In this context, errors due to spurious detections may be avoided by taking the distribution of a whole set inside that region and discarding the outliers based on a given criterion. The procedure herein detailed has been developed for the PIV acquisition performed along the vertical profile in the far field. Nonetheless, it can be adjusted to other profile acquisitions with minor (or any) modifications. From the sample shown in Figure 3.30, it is possible to distinguish five main elements: the bottom of the tank and the region below (1), the gravity current (2) propagating in the ambient fluid (3), the free surface (4) and the region above (5).

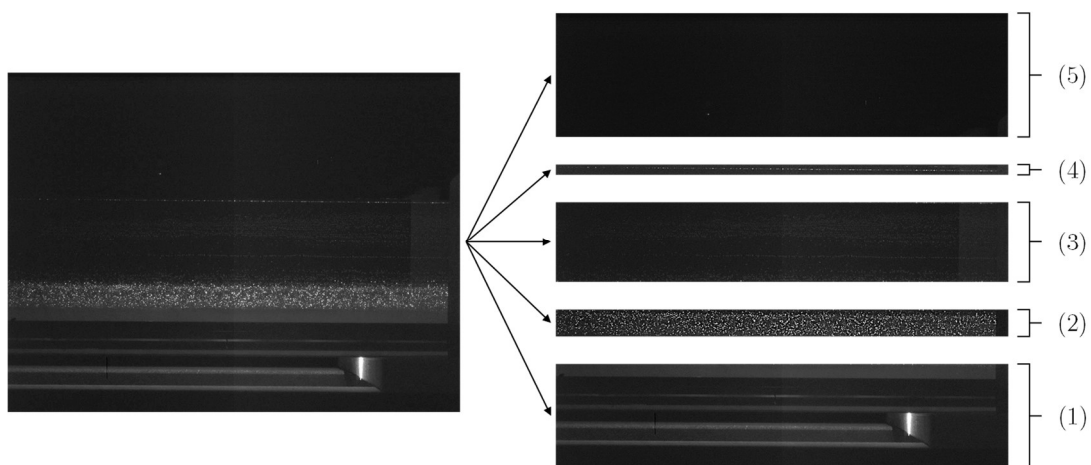


Figure 3.30: Bright-enhanced sample of a raw PIV acquisition and identification of the following elements: (1) tank's bottom, (2) gravity current, (3) ambient fluid, (4) free surface and (5) the region above.

As previously mentioned, a well-performed PIV acquisition leads to raw images where the contrast between the seeding particles and all the other elements is high, i.e. the seeding is typically represented by bright points over a dark background. For a better understanding, the bright levels of the actual sample shown in Figure 3.30 have been enhanced to expose some of the background elements mentioned above.

The depth of the current is the distance between the bottom⁹ and the upper limit defined in the beginning of this section. While the former is taken as a straight line, the latter must follow the depth variation that is observed along the current (especially in the frontal zone). Therefore, taking each image as a matrix, the problem is to find the line indexes that match these two boundaries. Then, counting the number of pixels between them, the distance (i.e., depth) is determined.

Since the bottom is fixed during the whole acquisition for each type of bed, its line index can be entered by the user who can read it from any of the images in analysis. By contrast, the identification of the upper boundary is automatically and the first step consists of separating the seeding particles (bright pixels) from the other elements. Thus, a grey value threshold is set and all pixels brighter than that are converted to full-white (255) while the remaining are set to full-black (0). This binary approach doesn't ensure that reflections or other bright elements apart from the seeding are discarded. Consequently, a second condition is imposed, limiting the detection to the region comprised between the bottom of the tank and the free surface (which line index is also entered by the user). From here, the detection shares some of the principles mentioned for the front tracing algorithm described in the previous section 3.4.2. The image is analysed column-by-column from the top to the bottom (i.e., from the free surface to the tank's bottom) and the line indexes of the first non-null detections are saved.

As depicted in Figure 3.31, two major problems may occur. The first is the situation in which any seeding particle is detected either because the current didn't arrive at the column in analysis or the seeding concentration is too low (see Figure 3.31a). In both cases, the column is said to be empty and the upper limit is set equal to the bottom by default. The second problem is the detection of bright pixels in the ambient fluid (due to impurities or reflections, for instance) and seeding particles that are too deep in the inner region of the current with any seeding above (see Figure 3.31b).

⁹ According to what has been previously stated, the bottom reference is the upper face of the glass panel for the smooth bed and the top of the bed crests for the rough configurations.

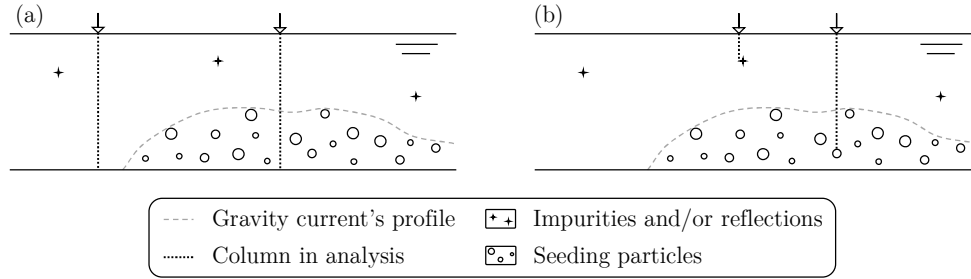


Figure 3.31: Example of algorithm failure due to empty-column (a) and outlier (b) detections.

The solution to these problems is to analyse the image in slices (i.e., groups of adjacent columns) and interpret the information of each as a whole. Then, both low and high outliers are rejected taking into account the distribution of all detections in that slice while the mean value of the remaining values can be taken as a good approximation. This approach is also valid for the situation of the first problem in which the current didn't arrive since the mean value will be equal to the line index of the bottom and the current depth is null in that part of the image.

In the present case, the width of these slices was set to 50 pixels as a compromise solution between the accuracy of the algorithm (in the sense that it is not influenced by wrong detections) and the fitting of the upper limit to the profile of the current. An example of the algorithm's output is shown in Figure 3.32 while the results are discussed in section 4.2.2.

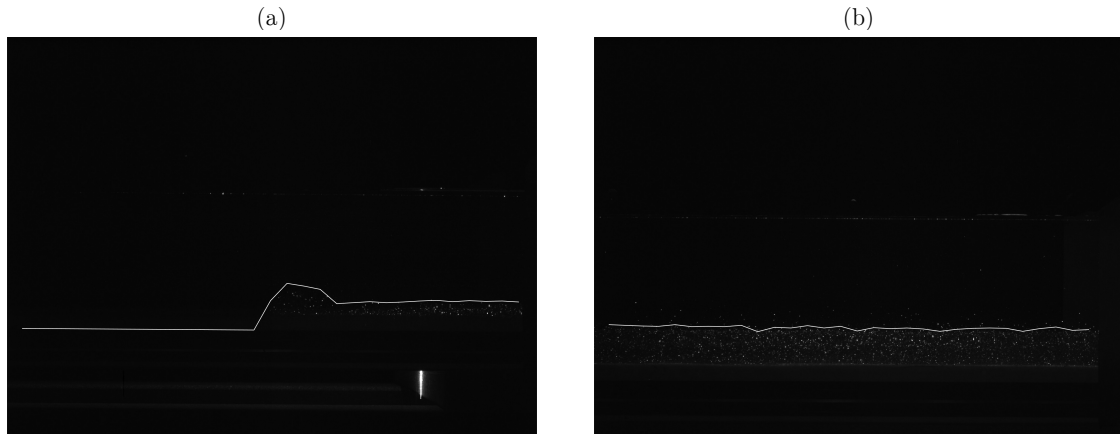


Figure 3.32: Examples of automatic profile detections comprising the head region for the smooth configuration (a) and the body of the current propagating over the semi-rough bed (b).

Chapter 4

Results

4.1 Flow visualization in the near field

4.1.1 Initial propagation

Once the discharge starts, it is noticeable that the current does not propagate in a perfect radial pattern before travelling the full width of the tank. Actually, the tracking of the front performed around the outlet (see section 3.4.2.1) reveals a higher mean velocity along the longitudinal direction, xx . This asymmetry can be observed in the detection samples shown in Figure 4.1 where the white line matches the position of the front or the limits of the detection region (concentric to the outlet) when the front is not comprised between them.

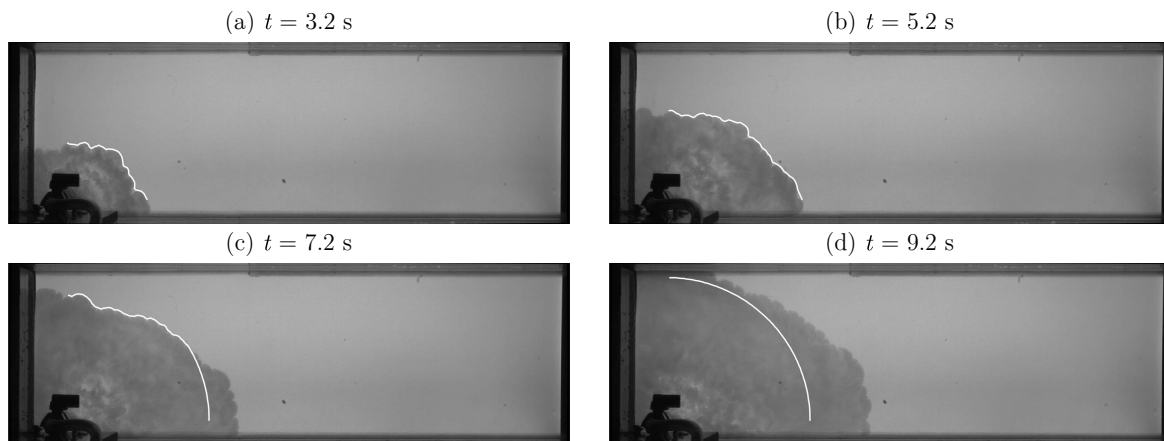


Figure 4.1: Front detection in the near field t seconds after the beginning of the discharge (smooth bed experiments).

The samples above respect to the smooth bed, although a similar effect can be visualized for both rough configurations as shown in Appendix C. That being said, the spatial distribution of the front's mean velocity for each type of bed is shown in Figure 4.2 where the horizontal axis represents the direction of analysis (0° for the yy and 90° for the xx). In all three plots, it is possible to observe a U-shape distribution meaning higher velocities along the confining walls AB and AD (see Figure 3.7 for referencing). This first result demonstrates the constraining effect of the corner DAB which forces the dense fluid to

flow around the outlet and the discharge's jet. In particular, the highest velocity along the sidewall AB (direction of 90°) is explained by the fact that the outlet is not equally distant from these confining walls¹⁰. Nonetheless, for the same geometrical configuration, this difference is more evident for the smooth bed and less pronounced in the multi-rough configuration for which the velocity along yy is similar to that along xx . This attenuation might be caused by the loss of momentum that results from dense fluid flowing through the voids between the particles on the bed. Likewise, the effect of bottom roughness also becomes noticeable in the mean velocity of the front, U_f , although a slightly higher value has been obtained for the multi-rough bed in comparison to the semi-rough.

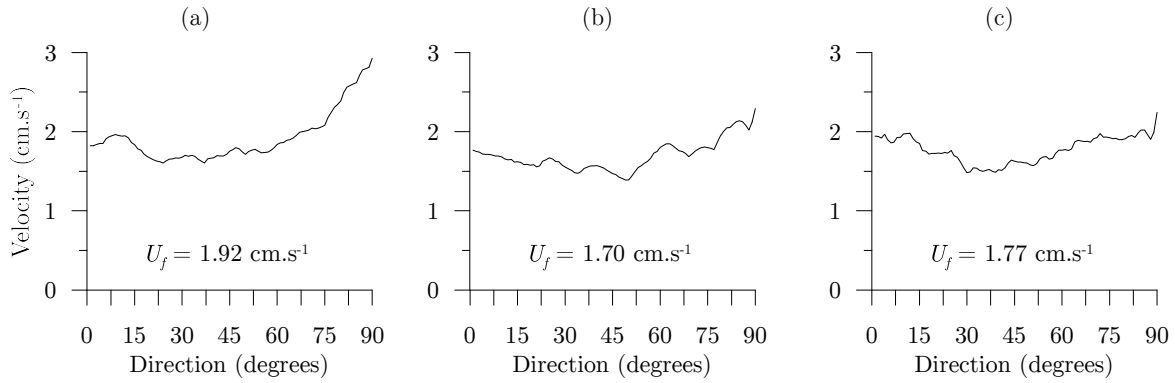


Figure 4.2: Front's mean velocity, U_f , and its spatial distribution in the region around the discharge for the three bed configurations: (a) smooth, (b) semi-rough and (c) multi-rough.

As depicted in Figure 4.4a, 8 s after the beginning of the discharge, the current reaches the sidewall CD and the accumulation of mass starts. According to Simpson (1997), this is due to the transfer of momentum from the horizontal to the vertical direction, i.e. the brine runs up the sidewall and the local depth increases ($t = 12$ s). Since the high-speed video technique does not allow for an insight on the current's depth, a PIV profile has been recorded perpendicularly to the sidewall CD (for $x = 5$ cm) in order to confirm this hypothesis. Despite the highly tri-dimensional flow, it is possible to observe upward velocity vectors at the time of impact (see Figure 4.3).

Meanwhile, dense fluid keeps flowing towards the wall and the accumulation zone becomes larger. At this point ($t = 13$ s – see Figure 4.4), the pressure gradient cannot be sustained for longer and the elevated fluid generates a wave that is probably a combination between a purely non-linear wave – which would generate a shock – and a non-linear-dispersive wave – a soliton. However, the classification of the exact nature of these waves is out of the scope of this thesis.

¹⁰ Walls AB and AD are distanced, respectively, 25 and 35 mm from the outlet (see section 3.2.1).

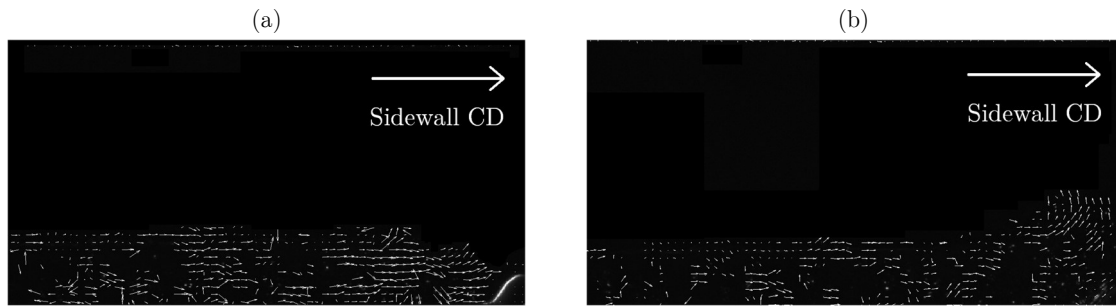


Figure 4.3: PIV acquisition along the profile EE' for: (a) $t = 11$ s and (b) $t = 12$ s.

The asymmetrical pattern of mass accumulation (resulting from the radial spreading of the current before its impact on the wall) is replicated in the shape of the reflected wave and the curvature of its crest is preserved while travelling from the sidewall CD to AB ($t = 14$ s and $t = 16$ s). In the meantime, the current's front spans along the width of the channel, although still denoting its radial genesis; for $t = 18$ s, the longitudinal distance travelled along the left side of the channel (CD) is lower in comparison to that along the right (AB).

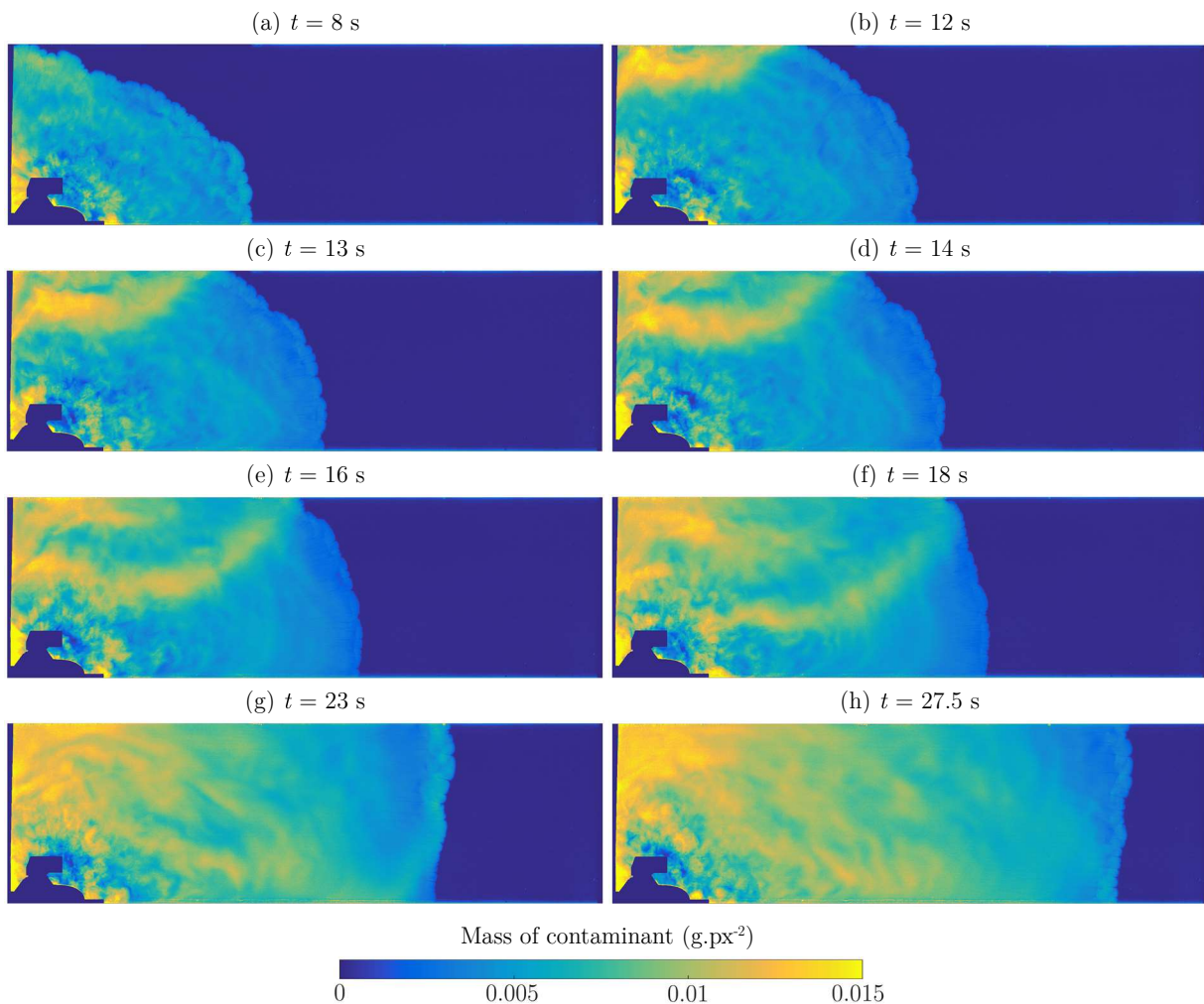


Figure 4.4: Contaminant mass distribution in the near field t seconds after the discharge.

Therefore, since the reflected wave is formed in the sidewall CD and it travels at a higher velocity than the current's front, they successively merge from the left to the right side, i.e. from the top to the bottom in the maps of Figure 4.4. During this process, two main effects can be observed: an increase in the front's propagation velocity and an accumulation of mass in the head region. The first can be observed between $t = 18$ s and $t = 23$ s, as the left side of the front overtakes the right side. In turn, the second effect is depicted in the highlighted head (meaning higher contaminant mass values) which is noticeable for $t = 23$ s. Nonetheless, the constant entrainment of freshwater causes the dilution of this accumulation and the highlighted region vanishes after about 3.5 s (for $t = 27.5$ s).

4.1.2 Effects on the front structures

In light of the results above, a further analysis of the current's front propagation was carried out. Despite the linear detection algorithm presented in section 3.4.2.2 has been detailed for the far field (with results being discussed in section 4.2.1) the routine was adapted to be used in the near field also. The main goal is to assess the effects of the merging process between the front of the current and the main reflected wave described in the previous section.

Since the detection is performed line by line, the plots shown in Figure 4.5 represent the time distribution (xx axis) of the quasi-instantaneous velocity along the width of the tank (yy axis). The first feature to be noticed is the earlier detection along the right sidewall – bottom of the plots – which is in accordance with the shape of the front before the arrival of the reflected wave. During these first instants, diagonal darker strings can be observed rising from the most forward positions (i.e., the first to be detected) which correspond to the lobes formation. These lines extent for some seconds suggesting a continual higher local velocity that can be interpreted as a growing lobe. They essentially develop in the direction of the most backward positions which is also in accordance with the previous hypothesis since the lobe can develop laterally if it is not constrained by another one. That being said, and looking at Figure 4.5, this type of instability (lobes and clefts) is more pronounced as more rough is the bed.

According to the previous section, the reflected wave does not merge simultaneously with the whole front. Hence, the effect on the velocity is represented by the oblique shadowed zone which can be observed in all the plots of Figure 4.5. Moreover, while the purely non-linear front suggests some displacement from the right sidewall to the left (marked by the rising strings), the reflected wave travels in the opposite direction from the sidewall CD to AB. When these two entities merge, there is a clear transfer of momentum from

the reflected wave to the structures at the front of the current. Yet again, this can be observed in all three scenarios for which the dark strings' pattern becomes aligned with the propagation of the reflected wave.

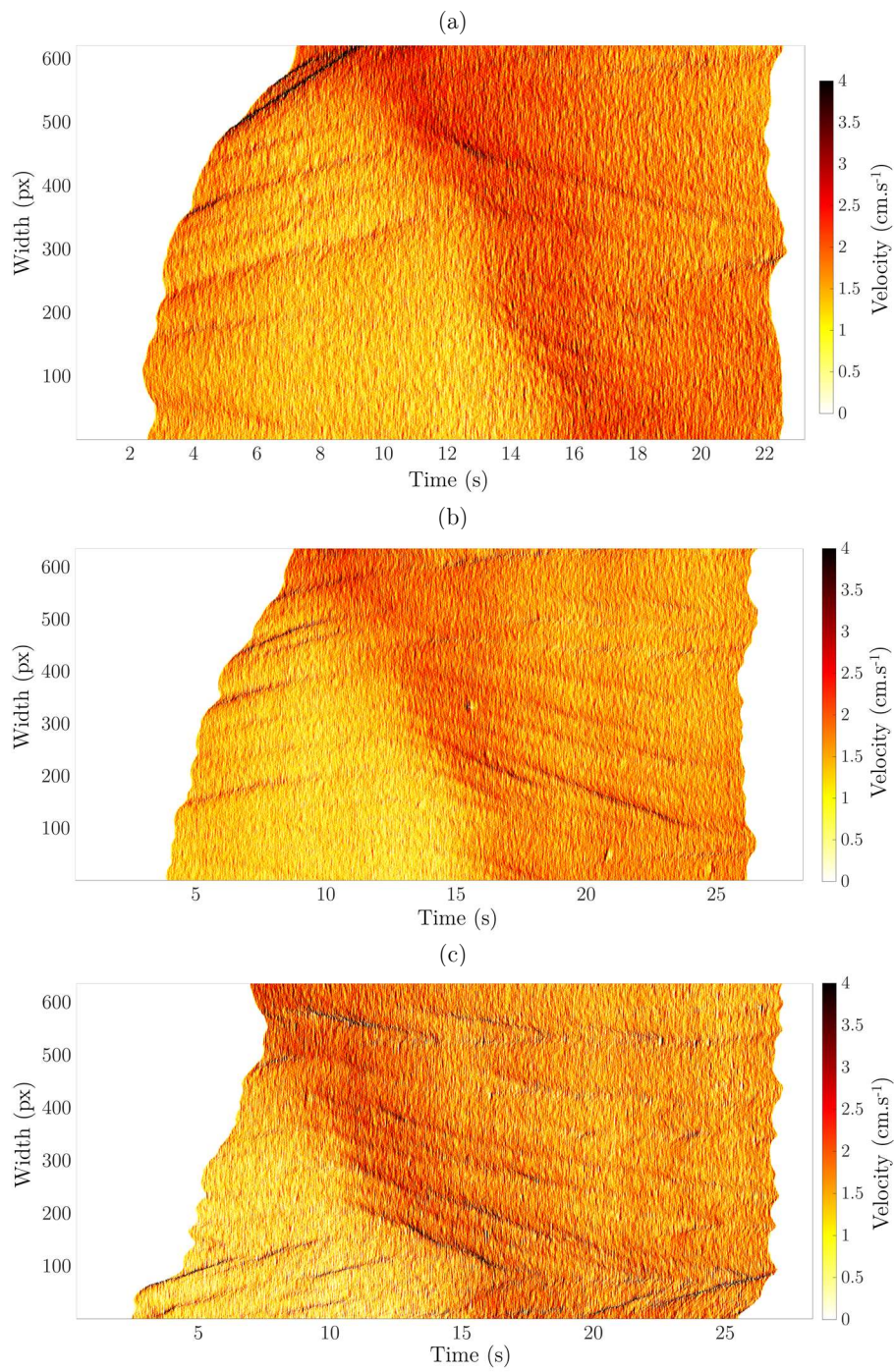


Figure 4.5: Time-width distribution of the quasi-instantaneous velocities of the front in the near field for the (a) smooth, (b) semi-rough and (c) multi-rough beds.

4.1.3 Effects on the body of the current

As the current's front advances (leaving the recording area) the contaminant mass increases all over the field of view as it is depicted in Figure 4.6. However, the transversal PIV acquisition mentioned in section 4.1.1 does not reveal an increase in the current's depth. This result is in accordance with the observations of Britter and Simpson (1978) and Hallworth et al. (1996) for which the extent of mixing in steady gravity currents (as it can be herein considered) was seen to be lower than for unsteady flows.

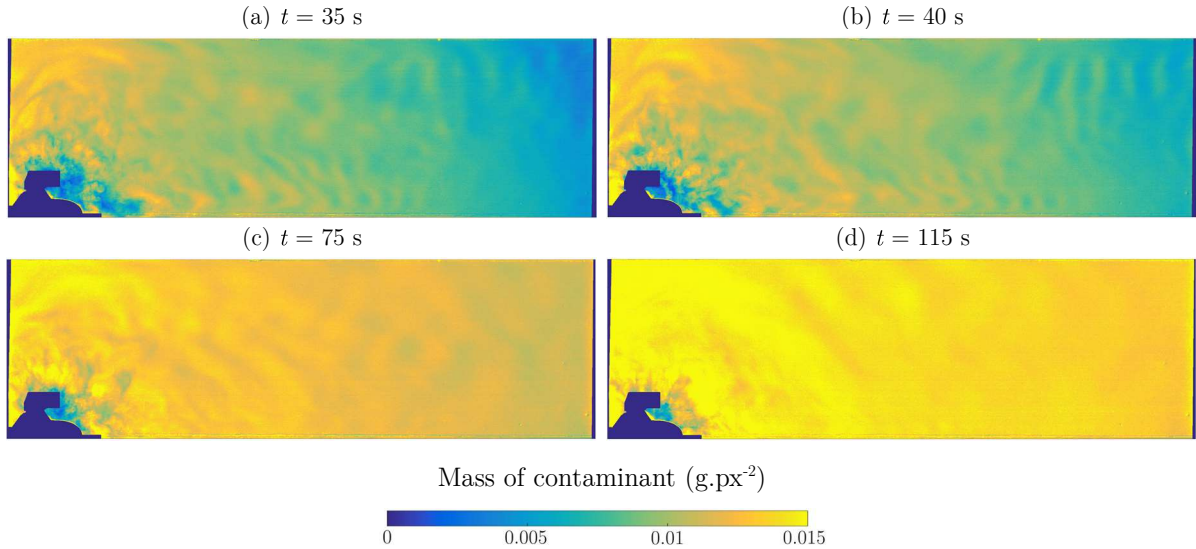


Figure 4.6: Contaminant mass distribution in the near field t seconds after the discharge.

Moreover, the contaminant accumulation is particularly enhanced in the vicinity of the corner ACD where the entrainment of ambient fluid is attenuated by the presence of the recirculation cell that is formed in that zone. This flow structure can be observed in the velocity fields of Figure 4.7 which respect to the horizontal acquisition performed 6 mm above the bottom for the smooth bed (see section 3.2.2). In those plots, a reduction in the overall velocity of the flow can also be noticed. The two jets around the outlet remain until the end of the experiments, for the three bed configurations. Nevertheless, the one along the yy direction tends to be deflected to the xx direction as the recirculation cell grows. Because of this, the formation of new reflections is strongly reduced, although not completely inhibited since wavelike patterns can still be observed in the right side of the near field mass maps (e.g., for $t = 40$ s in Figure 4.6).

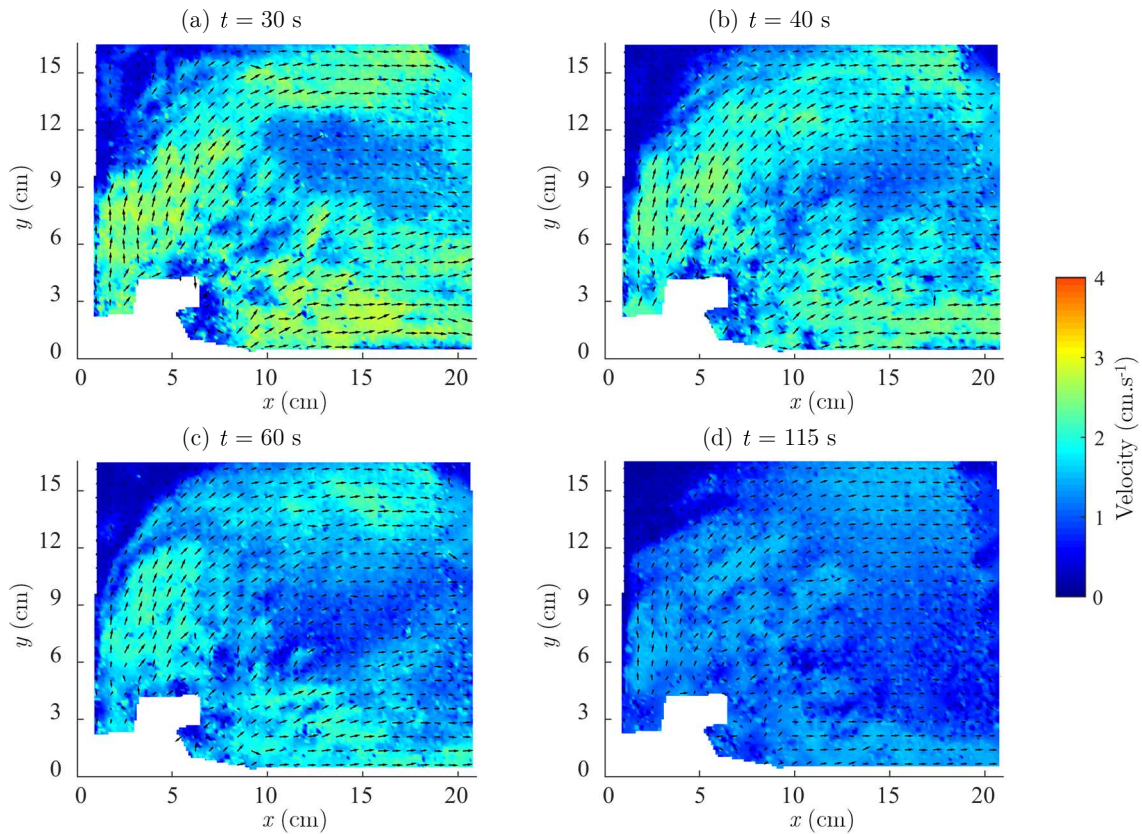


Figure 4.7: Horizontal velocity fields in the near field t seconds after the beginning of the discharge.

4.2 Flow visualization in the far field

4.2.1 The behaviour of the front

When the current flows from the near to the far field, the shape of the front becomes more linear, propagating perpendicularly to the sidewalls of the tank. As seen before, part of this uniformization process is induced by the reflections that end up at the front, causing local accelerations that interfere with the structure of the lobes and clefts. In this sense, the present section is intended to analyse the effects of those reflections in the structures of the front when this latter propagates far from the discharge and the dissipation at the bottom is relevant. Like what have been presented in section 4.1.2, the analysis makes use of the linear detection algorithm which output for the smooth bed is illustrated in Figure 4.8. Samples of these contours for the semi and multi-rough beds can also be found in Appendix C.

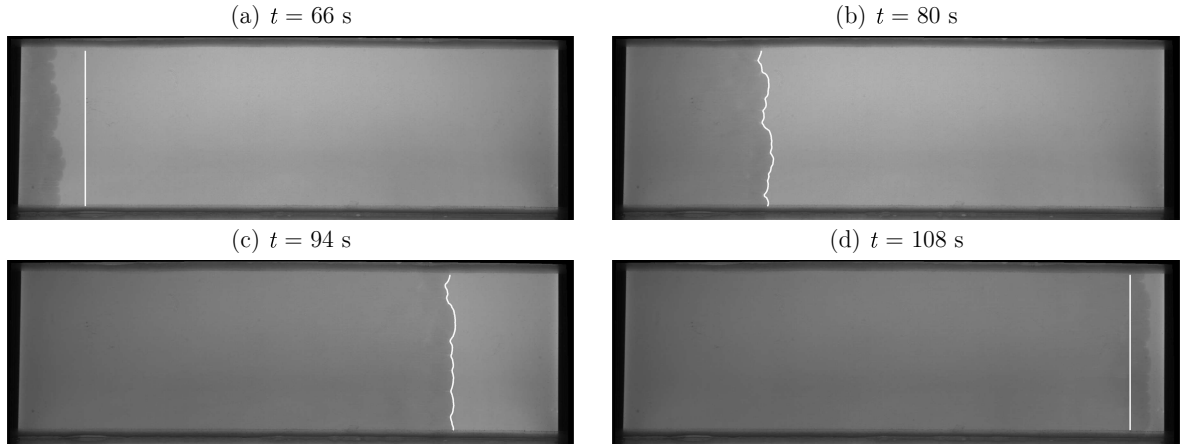


Figure 4.8: Front detection in the far field t seconds after the beginning of the discharge (smooth bed experiments).

The first velocity calculation was performed using the mean position of each contour (i.e., the front's centre of mass) for a given instant of time. The results of the front's mean velocity for each type of bed are presented in Figure 4.9.

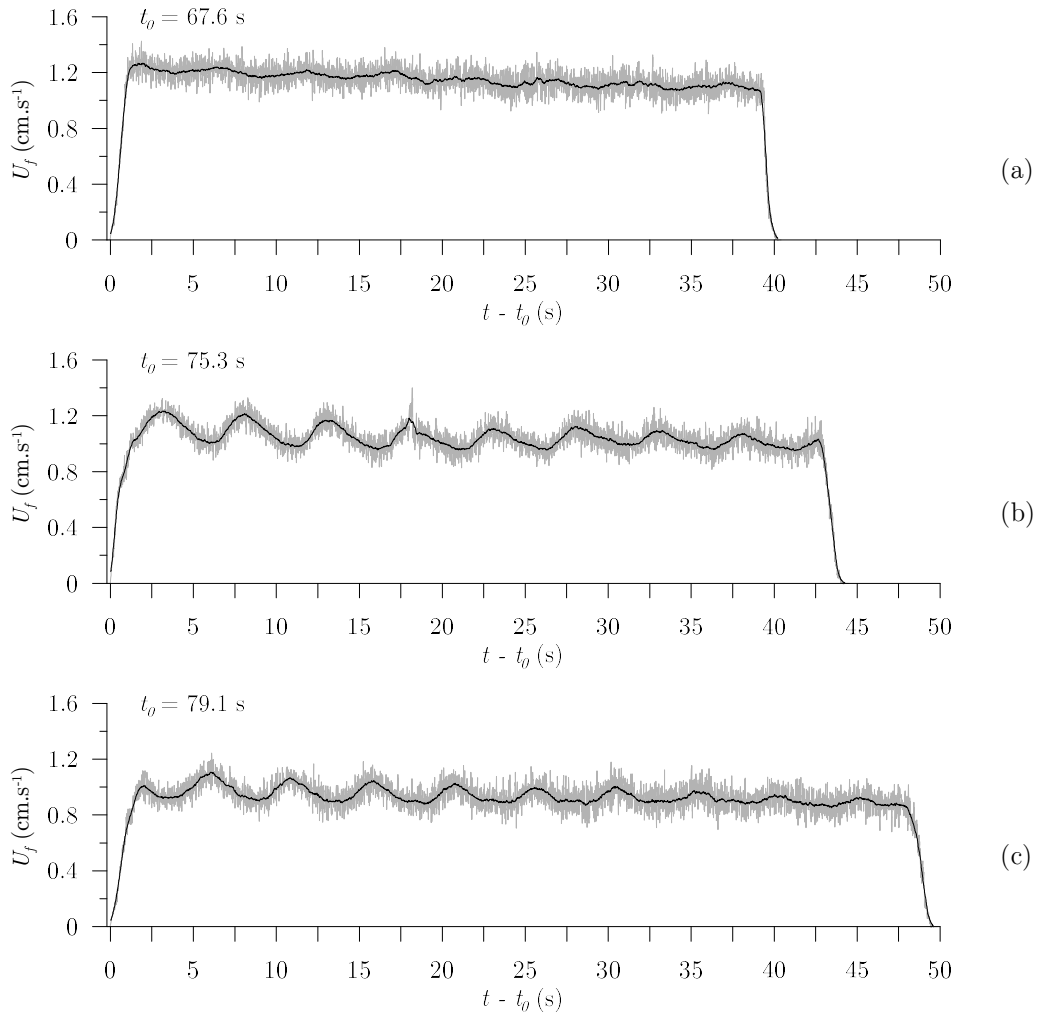


Figure 4.9: Mean velocity of the front, U_f , for the (a) smooth, (b) semi-rough and (c) multi-rough beds (black line represents the moving average).

As depicted in the previous plots, the highest values are observed for the smooth configuration ($U_f = 1.118 \text{ cm.s}^{-1}$), followed by the semi-rough ($U_f = 1.019 \text{ cm.s}^{-1}$) and multi-rough ($U_f = 0.908 \text{ cm.s}^{-1}$) beds. These results are in accordance with the observations of Peters and Venart (1999), Batt (2008) and La Rocca et al. (2008) for which a decrease on the front velocity is observed in the presence of rough surfaces. However, attention is given to the low-frequency oscillations which are not mentioned in any of these works. Despite the noise of the signals, these oscillations are observed for all three plots with emphasis on the rough configurations. Hence, a further analysis was carried out. As it has been done for the dense fluid discharge system (section 3.2.2), the power spectral density of the front's velocity fluctuations was obtained using the periodogram as spectral estimator. The results are shown in Figure 4.10 below.

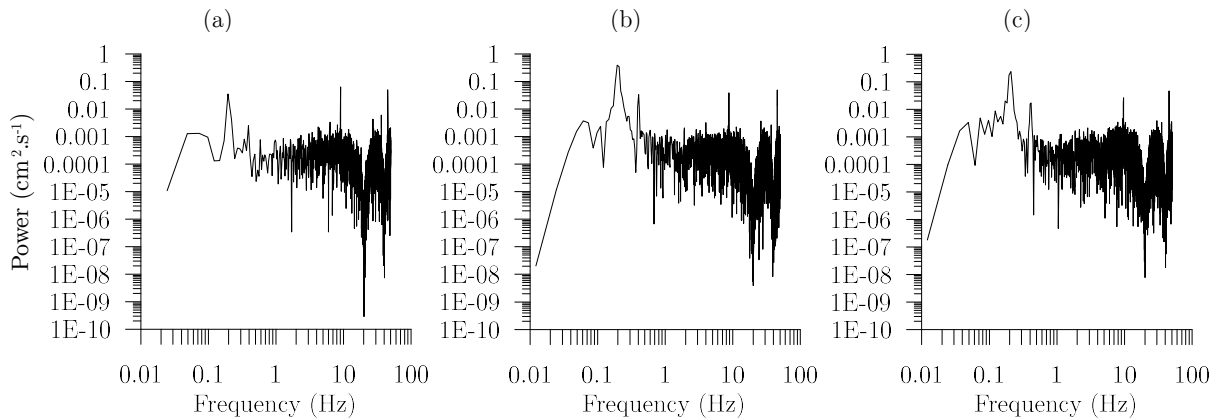


Figure 4.10: Power spectra plots (log-log) of the front's velocity for: (a) smooth, (b) semi and (c) multi-rough beds.

The frequency of the peak is similar for the three cases (0.2 Hz), although the energy is one order of magnitude below for the smooth bed. Since the temporal resolution of the data is constant, these velocity oscillations are caused by differences in the distance travelled by the front's centre of mass which in turn might be due to two reasons: (1) the lobes and clefts formation and (2) the propagation of the reflections occurring in the near field.

Assuming the first hypothesis, during the formation of a cleft, the front is detected in a backward position relatively to the rest of the current's front, thus contributing to a delay of the mean advancing ratio. By contrast, when two clefts merge, that contribution is reduced and a higher mean velocity is detected. Concerning the second hypothesis, the velocity fluctuations might result from the arrival of reflections at the current's front as it has been shown in section 4.1.2. In that scenario, the reflected waves mainly propagate in a non-parallel path with respect to the sidewalls of the tank due to the asymmetrical configuration of the experiments. Hence, their arrival at the far field is expected to result from a sloshing-like effect, i.e. after multiple reflections on the sidewalls. Taking into account the plots of the Figure 4.5, these waves would not arrive parallel to the current's front and local increases on the front's velocity would

be registered sequentially along the width of the channel. A similar width-time distribution of the quasi-instantaneous velocity of the front for each bed is presented in Figure 4.11¹¹ below.

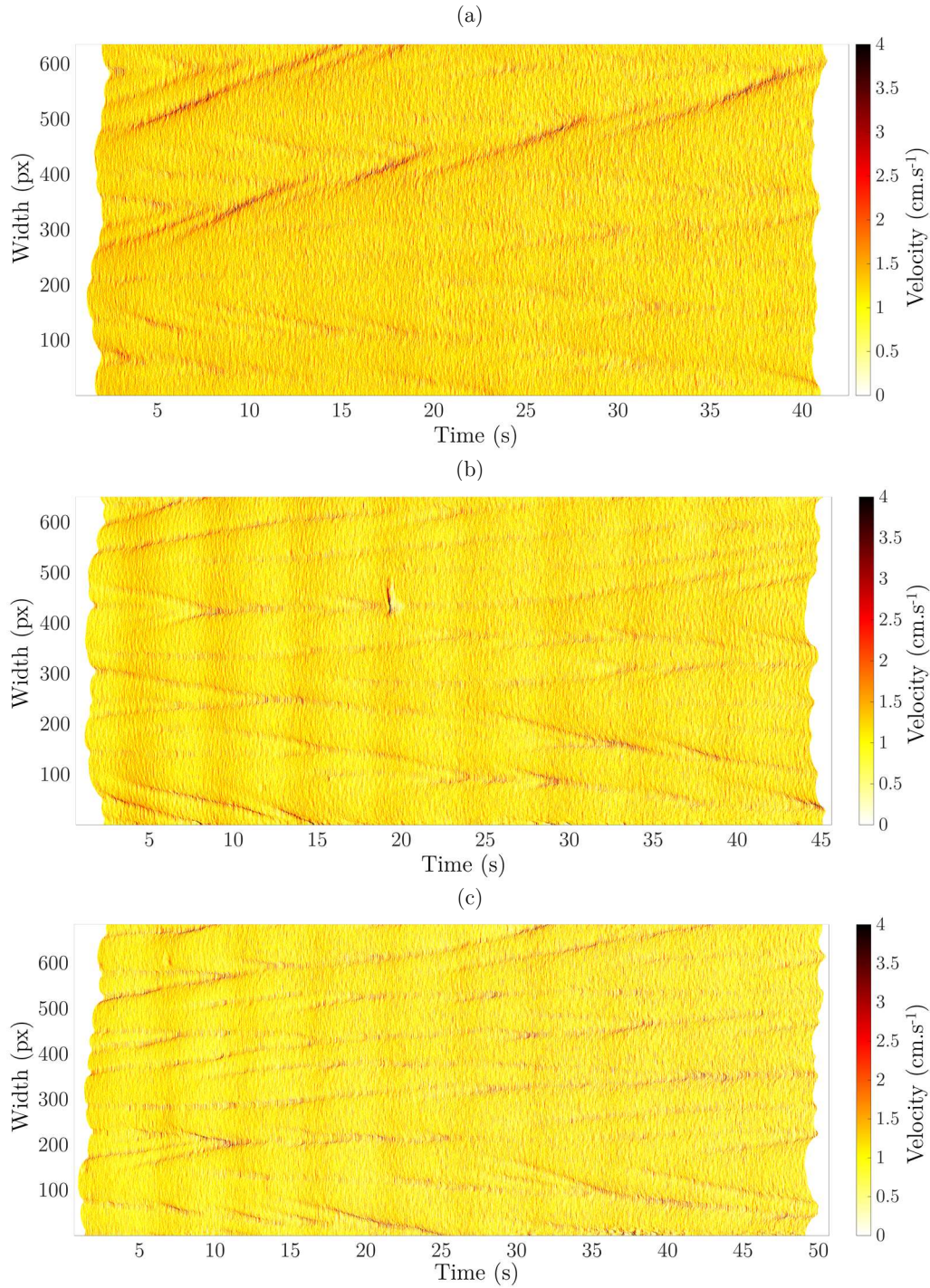


Figure 4.11: Time-width distribution of the quasi-instantaneous velocities of the front in the far field for the (a) smooth, (b) semi-rough and (c) multi-rough beds.

¹¹ The dark vertical segment in the semi-rough plot is a set of spurious values resulting from a failed detection. This local error is also noticed on the front's mean velocity shown in Figure 4.9b (represented by the peak for $t - t_0 \approx 18$ s).

Once again, the darker strings in these plots seem to be related with the lobes and clefts formation. Actually, despite the plots represent quasi-instantaneous velocities, the pattern in the semi and multi-rough configurations resemble the drawings from Simpson (1972) for the time-evolution of lobes (see Figure 2.3). Moreover, the observations of Batt (2008) regarding the effects of bed roughness on the size of the turbulence structures and billows appear to be replicated in the plots above as the pattern of the multi-rough configuration looks more fragmented than in the semi-rough. In turn, the oblique dark strings on the smooth plot do not share the same characteristics with the rough ones. Those marks might be related with the arrival of reflected waves at the current's front, although there is not a clear evidence of it.

4.2.2 The structure of the current's body

When the current travels the full length of the tank, a new reflection occurs in the end wall. As shown before, at this point, the flow can be considered unidimensional and the impact occurs along the normal to this wall. In light of this, the present section draws attention to the evolution of the current's depth (according to the methodology introduced in 3.4.3) and the structure of the velocity field, resulting both data from the PIV profile recorded along the mid-width section in the far field.

The evolution of the current's depth for the three bed configurations is shown in Figure 4.12. These plots were obtained from the average of the heights measured in each frame, thus they can be considered as a point measure. Looking at the first instants of detection, as the current starts to fill the width of the image, the depth evolution is marked by a steep increase during 15-20 seconds. From that point, the increasing rate is significantly lower, allowing for an estimation of the current's depth evolution in the body region. Although the transition happens in the three experiments, it is smoother for the multi-rough configuration. This result suggests that dense fluid gradually fills the voids between the beads on the bed, leading to a slower increase of the depth. Also, the drag induced by the bottom roughness should lead to a higher depth which is not evident, namely for the semi-rough configuration. Once again, it might be explained by the entrainment of dense fluid in the bed since the depth is measured from the top of the bed crests.

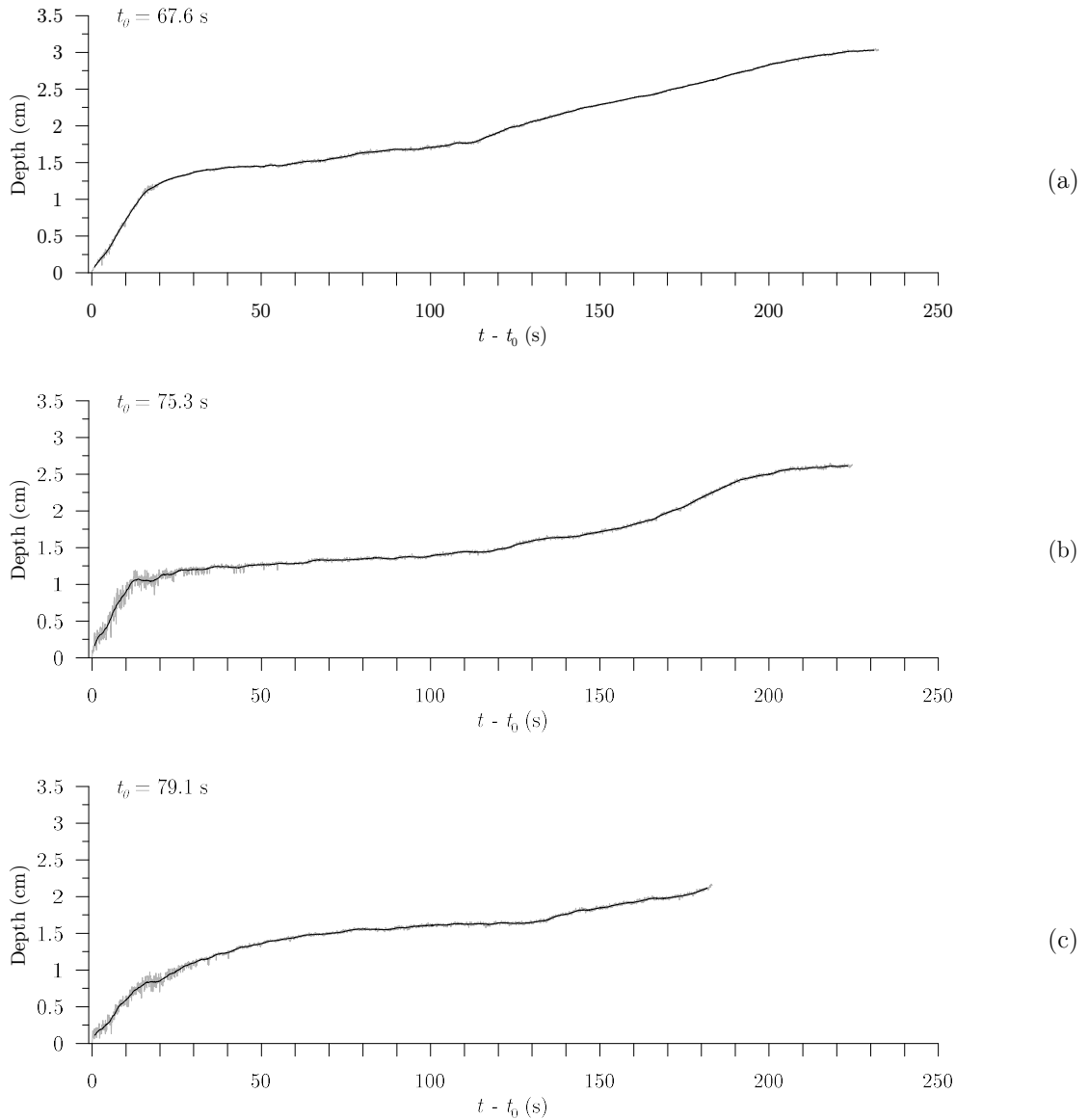


Figure 4.12: Current depth evolution for the (a) smooth, (b) semi-rough and (c) multi-rough bed configurations (black line represents the moving average).

Regarding the inner structure of the current during the reflection on the end wall of the tank, the velocity fields shown in Figure 4.13 respect to the smooth bed experiments. That being said, before the current arrives at the end wall, a quasi-steady velocity field can be observed ($t - t_0 = 64$ s). Then, the effect of the impact starts to propagate upstream in the form of a region of lower velocities that expands from the left side on the velocity fields ($t - t_0 = 118$ s) along the full depth of the current. This is also reflected in the increase of the current's depth which is visible in the plots of Figure 4.12 as an inflection point that occurs at about $t - t_0 = 110$ s (smooth), $t - t_0 = 115$ s (semi-rough) and $t - t_0 = 135$ s (multi-rough). This values are in accordance with the propagation velocities of each experiment. At a given instant, a backflow can be observed entering the field of view which occurs for $t - t_0 = 170$ s (smooth), $t - t_0 = 170$ s (semi-rough) and $t - t_0 = 180$ s (multi-rough). From this point, two layers flowing in opposite directions

can be distinguished in the gravity current (Figure 4.13e) and the continuous replenishment of dense fluid causes an increase in the velocity of the layer underneath.

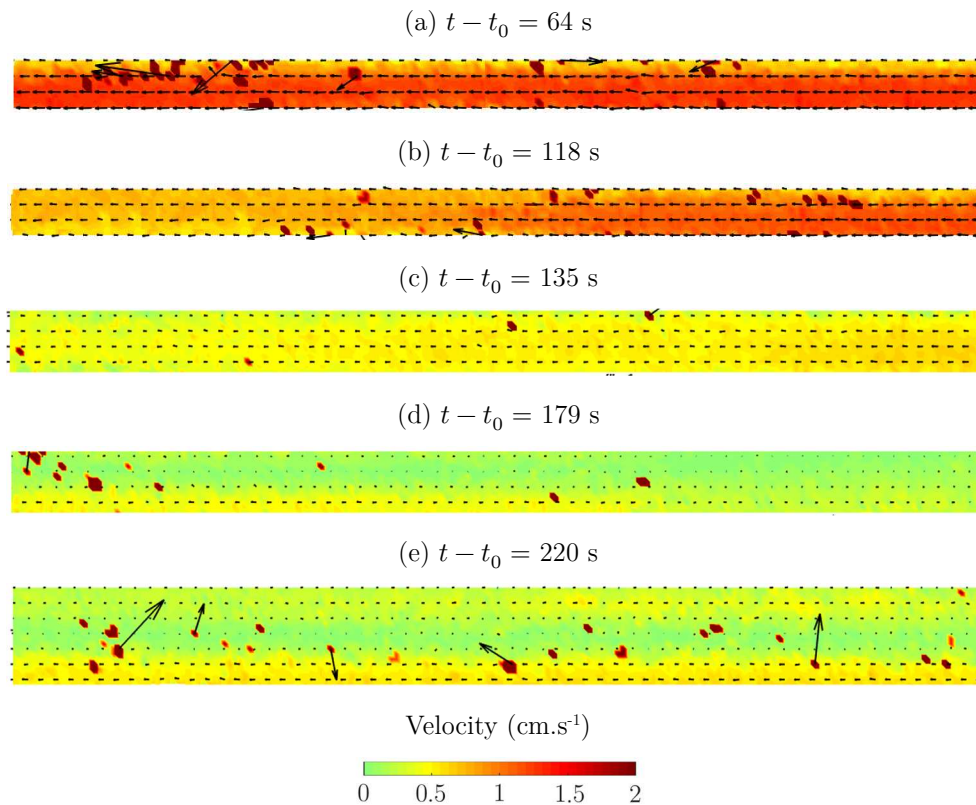


Figure 4.13: Velocity fields of the current propagating in the far field (smooth bed experiments).

The above-mentioned description of the reflection on the end wall of the tank does not coincide with a soliton in the sense of a well-defined wave. Actually, when the current reaches the rigid boundary, the available momentum is not high enough to origin the accumulation of mass that and the reflection occurs in the form of an intrusion that propagates in the interface between the body of the current and the ambient fluid.

Chapter 5

Conclusions

5.1 Summary

The present work intended to observe gravity currents in which the driving force is beyond the simple density gradient, i.e. currents that are subjected to the effects that arise from the interactions with the bottom roughness and the rigid boundaries.

Laboratory experiments revealed that typical structures characterizing these flows are affected by reflected waves, namely during the first moments when the friction at the bottom does not play such an important role. The mass distribution analysis suggests that those reflections are responsible for a transfer of mass to the front of the current which in turn lead to local accelerations. The same technique also allowed for the identification of regions of lower dilution. These latter appear as a consequence of the recirculation structures that could be observed in the flow velocity fields.

When the current propagates to the far field, there is a loss of momentum that is not only due to the friction at the bottom, but also to dense fluid that flows through the voids in the rough beds and inhibits the depth increase that provides the driving force. The decrease of the front's velocity for the rough configurations is in accordance with previous studies. However, the tracking methodology revealed oscillations that have not been mentioned in the past and which might be related to the reflections from the near field. Moreover, the results suggest a good agreement with the observations of Simpson (1972) – in what concerns the pattern of lobes and clefts formation – and Batt (2008) – regarding the extent of these structures.

5.2 Guidelines for future work

The present work provided a new contribution for the understanding of the interaction phenomena that arise from gravity currents flowing in complex geometries and different roughness beds. Nonetheless, the results obtained also raise new questions and suggestions for future works on this topic.

The main question concerns the front's velocity patterns observed in the far field. Despite the diagonal strings on the smooth configuration and the oscillations in the mean velocity for the rough beds, the genesis of these effects is not clear. In this sense, different discharge positions (including symmetrical configurations) could provide valuable information.

Regarding the mass distribution analysis herein developed, its application in rough configurations might become possible if the particles on the bottom are glued to the glass. This way, the volumes of dyed fluid required for calibration purposes could be taken out without affecting the delicate pixel-by-pixel methodology; the use of a bottom outlet that would allow for the washing of the glued particles can also be considered.

Finally, the data collected during the present experimental work has high resolution (both in space and time). Therefore, it might be used in the evaluation of the performance of numerical models for the simulation of stratified flows and/or in their calibration.

References

- Adrian, R. J. (2005). "Twenty years of particle image velocimetry." *Experiments in Fluids*, 39 (2), 159-169.
- Altinakar, S., Graf, W. H. and Hopfinger, E. J. (1990). "Weakly depositing turbidity current on a small slope." *Journal of Hydraulic Research*, 28 (1), 55-80.
- Altinakar, S., Graf, W. H. and Hopfinger, E. J. (1996). "Flow structure in turbidity currents." *Journal of Hydraulic Research*, 34 (5), 713-718.
- Batt, R. L. (2008), The influence of bed roughness on the dynamics of gravity currents, PhD Thesis. University of Leeds.
- Benjamin, T. B. (1968). "Gravity currents and related phenomena." *Journal of Fluid Mechanics*, 31 (02), 209-248.
- Bhaganagar, K. (2014). "Direct numerical simulation of lock-exchange density currents over the rough wall in slumping phase." *Journal of Hydraulic Research*, 52 (3), 386-398.
- Britter, R. E. and Simpson, J. E. (1978). "Experiments on the dynamics of a gravity current head." *Journal of Fluid Mechanics*, 88 (02), 223-240.
- Buckee, C., Kneller, B. and Peakall, J. (2001). "Turbulence structure in steady, solute-driven gravity currents." *Particulate gravity currents*, 173-187.
- Cenedese, C. and Adduce, C. (2010). "A new parameterization for entrainment in overflows." *Journal of Physical Oceanography*, 40 (8), 1835-1850.
- Cenedese, C., Nokes, R. and Hyatt, J. (2016). "Lock-exchange gravity currents over rough bottoms." *Environmental fluid mechanics*, 1-15.
- Cesare, G. D., Schleiss, A. and Hermann, F. (2001). "Impact of turbidity currents on reservoir sedimentation." *Journal of Hydraulic Engineering*, 127 (1), 6-16.
- Ding, A., Wang, T., Zhao, M., Wang, T. and Li, Z. (2004). "Simulation of sea-land breezes and a discussion of their implications on the transport of air pollution during a multi-day ozone episode in the Pearl River Delta of China." *Atmospheric Environment*, 38 (39), 6737-6750.
- Doronzo, D. M., Martí, J., Dellino, P., Giordano, G. and Sulpizio, R. (2016). "Dust storms, volcanic ash hurricanes, and turbidity currents: physical similarities and differences with emphasis on flow temperature." *Arabian Journal of Geosciences*, 9 (4), 1-9.
- Ellison, T. H. and Turner, J. S. (1959). "Turbulent entrainment in stratified flows." *Journal of Fluid Mechanics*, 6 (03), 423-448.
- Firoozabadi, B., Afshin, H. and Sheikhi, J. (2009). "Experimental investigation of single value variables of three-dimensional density current." *Canadian Journal of Physics*, 87 (2), 125-134.
- Hacker, J., Linden, P. F. and Dalziel, S. B. (1996). "Mixing in lock-release gravity currents." *Dynamics of Atmospheres and Oceans*, 24 (1-4), 183-195.

- Hallworth, M. A., Huppert, H. E., Phillips, J. C. and Sparks, R. S. J. (1996). "Entrainment into two-dimensional and axisymmetric turbulent gravity currents." *Journal of Fluid Mechanics*, 308 289-311.
- Haynes, W. M. (2014). *CRC handbook of chemistry and physics*. CRC press.
- Huppert, H. E. (2006). "Gravity currents: a personal perspective." *Journal of Fluid Mechanics*, 554 299-322.
- Huppert, H. E. and Simpson, J. E. (1980). "The slumping of gravity currents." *Journal of Fluid Mechanics*, 99 (04), 785-799.
- Keane, R. D. and Adrian, R. J. (1990). "Optimization of particle image velocimeters. I. Double pulsed systems." *Measurement Science and Technology*, 1 (11), 1202.
- Kestin, J., Khalifa, H. E. and Correia, R. J. (1981). "Tables of the dynamic and kinematic viscosity of aqueous NaCl solutions in the temperature range 20–150 C and the pressure range 0.1–35 MPa." *Journal of physical and chemical reference data*, 10 (1), 71-88.
- Khavasi, E., Afshin, H. and Firoozabadi, B. (2012). "Effect of selected parameters on the depositional behaviour of turbidity currents." *Journal of Hydraulic Research*, 50 (1), 60-69.
- Kneller, B. and Buckee, C. (2000). "The structure and fluid mechanics of turbidity currents: a review of some recent studies and their geological implications." *Sedimentology*, 47 (s1), 62-94.
- Kneller, B. C., Bennett, S. J. and McCaffrey, W. D. (1999). "Velocity structure, turbulence and fluid stresses in experimental gravity currents." *Journal of Geophysical Research*, 104 (C3), 5381-5391.
- Krug, D., Holzner, M., Lüthi, B., Wolf, M., Kinzelbach, W. and Tsinober, A. (2015). "The turbulent/non-turbulent interface in an inclined dense gravity current." *Journal of Fluid Mechanics*, 765 303-324.
- La Rocca, M., Adduce, C., Sciortino, G. and Pinzon, A. B. (2008). "Experimental and numerical simulation of three-dimensional gravity currents on smooth and rough bottom." *Physics of Fluids*, 20 (10), 106603.
- Lalas, D. P., Asimakopoulou, D. N., Deligiorgi, D. G. and Helmis, C. G. (1983). "Sea-breeze circulation and photochemical pollution in Athens, Greece." *Atmospheric Environment (1967)*, 17 (9), 1621-1632.
- Lauterborn, W. and Vogel, A. (1984). "Modern optical techniques in fluid mechanics." *Annual Review of Fluid Mechanics*, 16 (1), 223-244.
- Linden, P. F. (1999). "The fluid mechanics of natural ventilation." *Annual Review of Fluid Mechanics*, 31 (1), 201-238.
- Lowe, R. J., Linden, P. F. and Rottman, J. W. (2002). "A laboratory study of the velocity structure in an intrusive gravity current." *Journal of Fluid Mechanics*, 456 33-48.
- Martin, J. E. and García, M. H. (2009). "Combined PIV/PLIF measurements of a steady density current front." *Experiments in Fluids*, 46 (2), 265-276.

- Meng, X., Wang, Y., Liu, T., Xing, X., Cao, Y. and Zhao, J. (2016). "Influence of radiation on predictive accuracy in numerical simulations of the thermal environment in industrial buildings with buoyancy-driven natural ventilation." *Applied Thermal Engineering*, 96 473-480.
- Middleton, G. V. (1993). "Sediment deposition from turbidity currents." *Annual Review of Earth and Planetary Sciences*, 21 89-114.
- Morozov, E. G., Trulsen, K., Velarde, M. G. and Vlasenko, V. I. (2002). "Internal tides in the Strait of Gibraltar." *Journal of Physical Oceanography*, 32 (11), 3193-3206.
- Nogueira, H. I. S., Adduce, C., Alves, E. and Franca, M. J. (2013a). "Analysis of lock-exchange gravity currents over smooth and rough beds." *Journal of Hydraulic Research*, 51 (4), 417-431.
- Nogueira, H. I. S., Adduce, C., Alves, E. and Franca, M. J. (2013b). "Image analysis technique applied to lock-exchange gravity currents." *Measurement Science and Technology*, 24 (4), 047001.
- Nogueira, J., Lecuona, A. and Rodriguez, P. A. (1997). "Data validation, false vectors correction and derived magnitudes calculation on PIV data." *Measurement Science and Technology*, 8 (12), 1493.
- Oehy, C. D. and Schleiss, A. J. (2007). "Control of turbidity currents in reservoirs by solid and permeable obstacles." *Journal of Hydraulic Engineering*, 133 (6), 637-648.
- Özgökmen, T. M., Fischer, P. F., Duan, J. and Iliescu, T. (2004). "Entrainment in bottom gravity currents over complex topography from three-dimensional nonhydrostatic simulations." *Geophysical Research Letters*, 31 (13),
- Parish, T. R. and Cassano, J. J. (2003). "The role of katabatic winds on the Antarctic surface wind regime." *Monthly Weather Review*, 131 (2), 317-333.
- Parker, G., Garcia, M., Fukushima, Y. and Yu, W. (1987). "Experiments on turbidity currents over an erodible bed." *Journal of Hydraulic Research*, 25 (1), 123-147.
- Peters, W. D. and Venart, J. E. S. (1999), Rough-surface gravity current flows, Thesis. University of New Brunswick, Department of Mechanical Engineering.
- Phillips, J. C. and Woods, A. W. (2004). "On ventilation of a heated room through a single doorway." *Building and environment*, 39 (3), 241-253.
- Pickering, C. J. D. and Halliwell, N. A. (1984). "Laser speckle photography and particle image velocimetry: photographic film noise." *Applied optics*, 23 (17), 2961-2969.
- Piper, D. J. W. and Normark, W. R. (2009). "Processes that initiate turbidity currents and their influence on turbidites: a marine geology perspective." *Journal of Sedimentary Research*, 79 (6), 347-362.
- Raffel, M., Willert, C. E., wereley, s. and Kompenhans, J. (2007). *Particle Image Velocimetry: A Practical Guide*. Springer Berlin Heidelberg.
- Rahmstorf, S. (2002). "Ocean circulation and climate during the past 120,000 years." *Nature*, 419 (6903), 207-214.

- Roscoe, R. (1952). "The viscosity of suspensions of rigid spheres." *British Journal of Applied Physics*, 3 (8), 267.
- Rottman, J. W. and Simpson, J. E. (1983). "Gravity currents produced by instantaneous releases of a heavy fluid in a rectangular channel." *Journal of Fluid Mechanics*, 135 95-110.
- Sequeiros, O. E., Spinewine, B., Beaubouef, R. T., Sun, T., García, M. H. and Parker, G. (2010). "Characteristics of velocity and excess density profiles of saline underflows and turbidity currents flowing over a mobile bed." *Journal of Hydraulic Engineering*, 136 (7), 412-433.
- Shin, J. O., Dalziel, S. B. and Linden, P. F. (2004). "Gravity currents produced by lock exchange." *Journal of Fluid Mechanics*, 521 1-34.
- Simpson, J. E. (1969). "A comparison between laboratory and atmospheric density currents." *Quarterly Journal of the Royal Meteorological Society*, 95 (406), 758-765.
- Simpson, J. E. (1972). "Effects of the lower boundary on the head of a gravity current." *Journal of Fluid Mechanics*, 53 (04), 759-768.
- Simpson, J. E. (1982). "Gravity Currents in the Laboratory, Atmosphere, and Ocean." *Annual Review of Fluid Mechanics*, 14 (1), 213-234.
- Simpson, J. E. (1997). *Gravity currents: In the environment and the laboratory*. Cambridge University Press.
- Simpson, J. E. and Britter, R. E. (1979). "The dynamics of the head of a gravity current advancing over a horizontal surface." *Journal of Fluid Mechanics*, 94 (03), 477-495.
- Stacey, M. W. and Bowen, A. J. (1988). "The vertical structure of density and turbidity currents: theory and observations." *Journal of Geophysical Research: Oceans*, 93 (C4), 3528-3542.
- Stagnaro, M. and Pittaluga, M. B. (2014). "Velocity and concentration profiles of saline and turbidity currents flowing in a straight channel under quasi-uniform conditions." *Earth Surface Dynamics*, 2 (1), 167.
- Theiler, Q. and Franca, M. J. (2016). "Contained density currents with high volume of release." *Sedimentology*, 63 (6), 1820-1842.
- Thomas, L. P., Dalziel, S. B. and Marino, B. M. (2003). "The structure of the head of an inertial gravity current determined by particle-tracking velocimetry." *Experiments in Fluids*, 34 (6), 708-716.
- Tropea, C., Yarin, A. L. and Foss, J. F. (2007). *Springer handbook of experimental fluid mechanics*. Springer Science & Business Media.
- Turner, J. S. (1973). *Buoyancy effects in fluids*. Cambridge University Press.
- Ungarish, M. (2007). "Axisymmetric gravity currents at high Reynolds number: On the quality of shallow-water modeling of experimental observations." *Physics of Fluids*, 19 (3), 036602.
- Ungarish, M. (2009). *An introduction to gravity currents and intrusions*. CRC Press.

- Vitasse, Y., Klein, G., Kirchner, J. W. and Rebetez, M. (2016). "Intensity, frequency and spatial configuration of winter temperature inversions in the closed La Brevine valley, Switzerland." *Theoretical and Applied Climatology*, 1-11.
- Wereley, S. T. and Meinhart, C. D. (2000). "Accuracy improvements in particle image velocimetry algorithms."
- Westerweel, J. (1994). "Efficient detection of spurious vectors in particle image velocimetry data." *Experiments in Fluids*, 16 (3-4), 236-247.
- Willert, C., Stasicki, B., Klinner, J. and Moessner, S. (2010). "Pulsed operation of high-power light emitting diodes for imaging flow velocimetry." *Measurement Science and Technology*, 21 (7), 075402.
- Zhu, J. B., Lee, C. B., Chen, G. Q. and Lee, J. H. W. (2006). "PIV observation of instantaneous velocity structure of lock release gravity currents in the slumping phase." *Communications in Nonlinear Science and Numerical Simulation*, 11 (2), 262-270.

Appendices

Appendix A: Spectral analysis of the discharge

The power spectral density of the discharge fluctuations was obtained using the periodogram as spectral estimator. These fluctuations were obtained by subtracting the trend of the signal which was approximated by a fourth-degree polynomial. The spectra for each run is shown in Figure A.1 below.

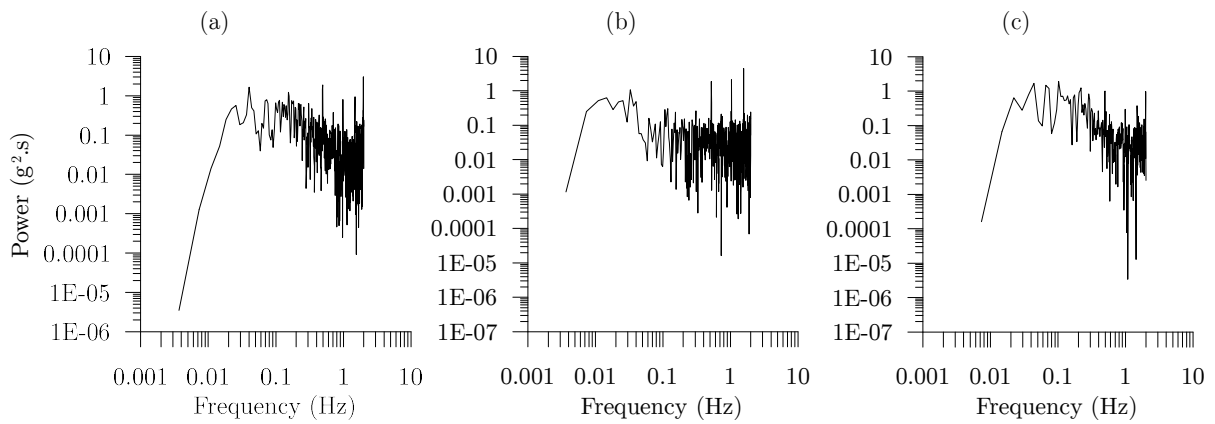


Figure A.1: Power spectra plots (log-log) of the mass variation for: (a) Run 1, (b) Run 2 and (c) Run 3.

As it can be observed, the dominant spike in the front's velocity analysis is not replicated in the spectra above. Therefore, the discharge system is considered not to be the genesis of those oscillations.

Appendix B: Calibration maps

The coefficient maps that result from the calibration of the near field are shown in Figure B.1 below.

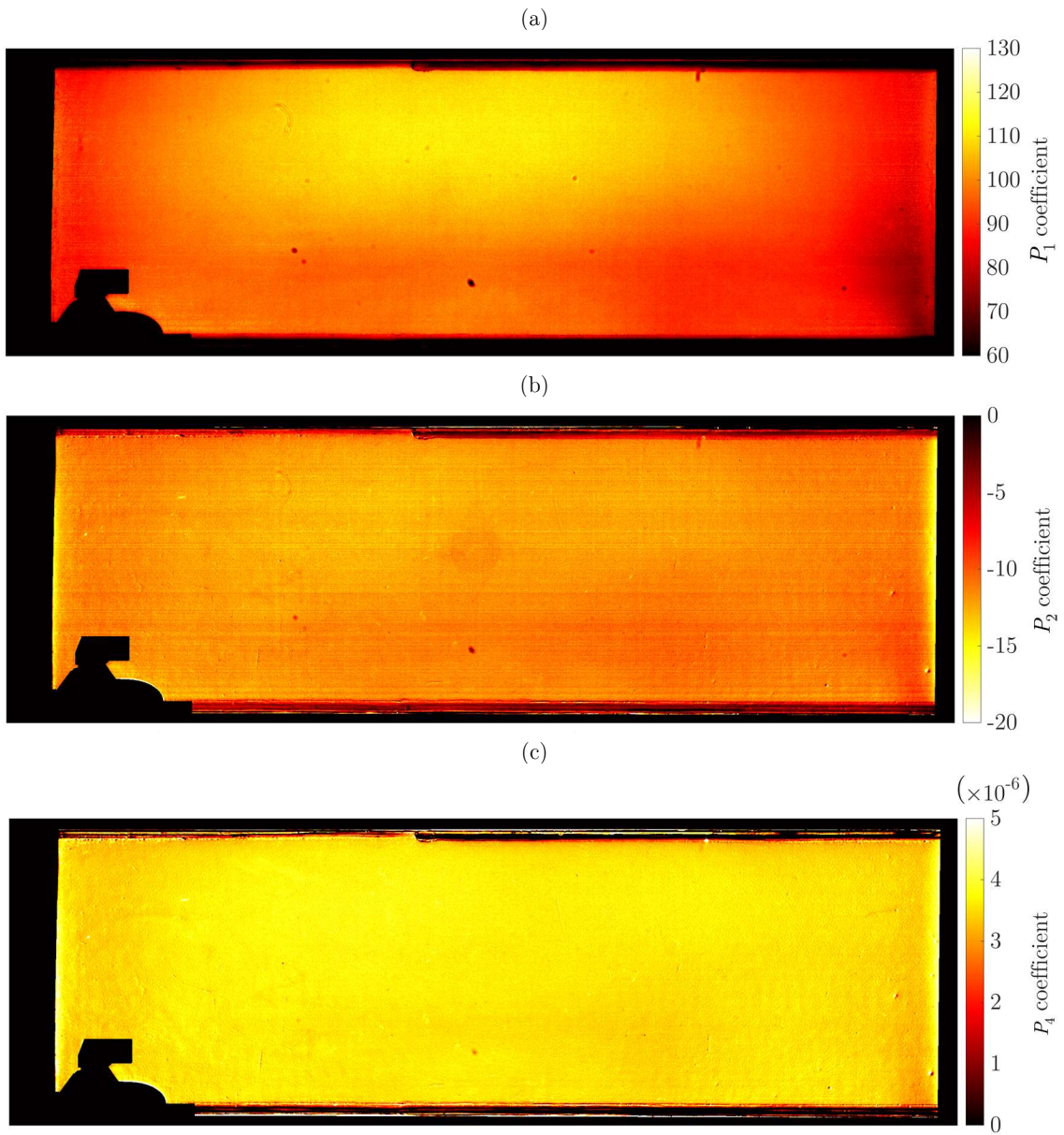


Figure B.1: Plots of the coefficients P_1 (a), P_2 (b) and P_4 (c) of the calibration curves adopted in the near field.

The coefficient maps that result from the calibration of the far field are shown in Figure B.2 below.

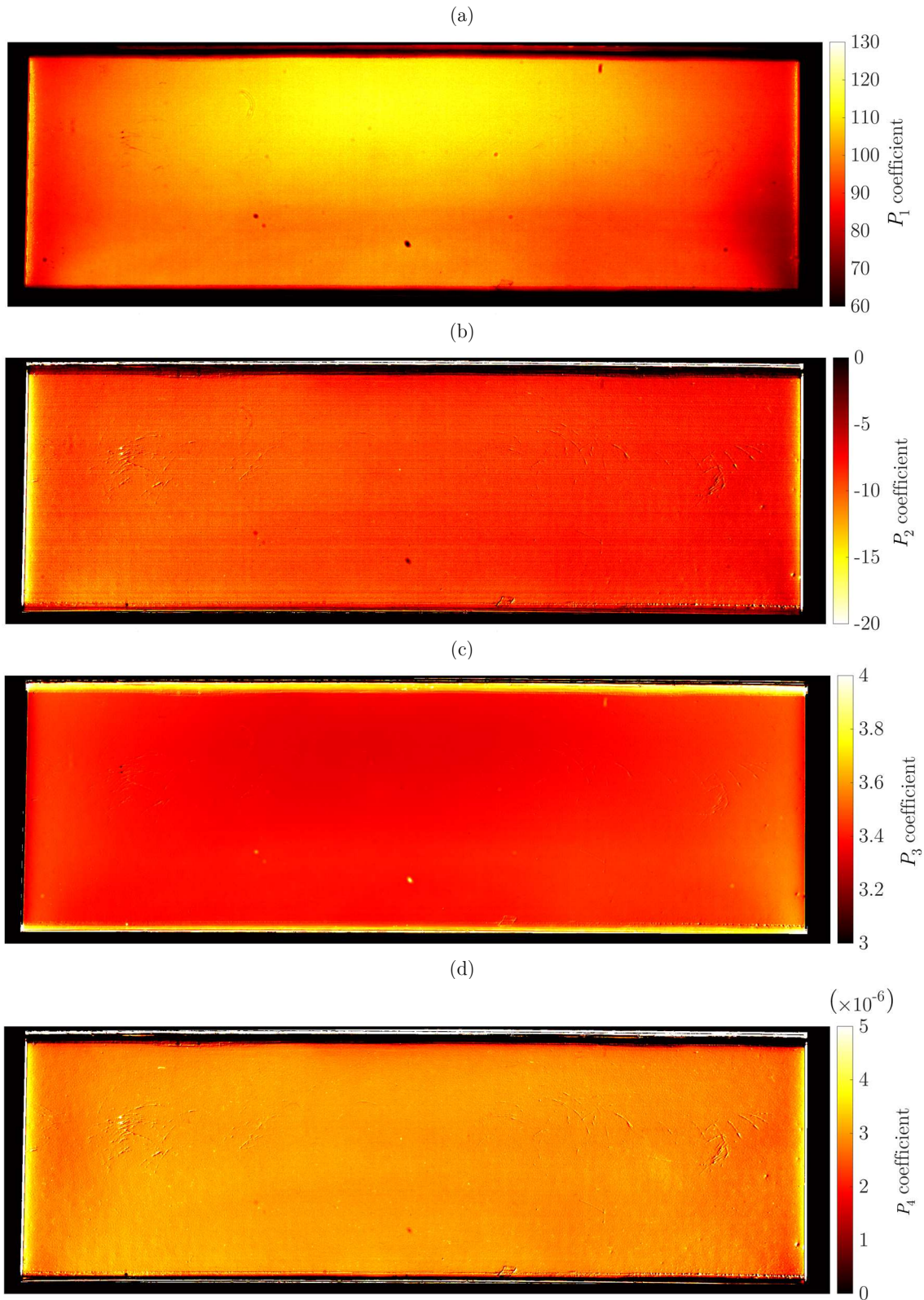


Figure B.2: Plots of the coefficients P_1 (a), P_2 (b), P_3 (c) and P_4 (d) of the calibration curves adopted in the far field.

The plot of the Pearson correlation coefficients obtained in the calibration of the far field are shown in Figure B.3 below.

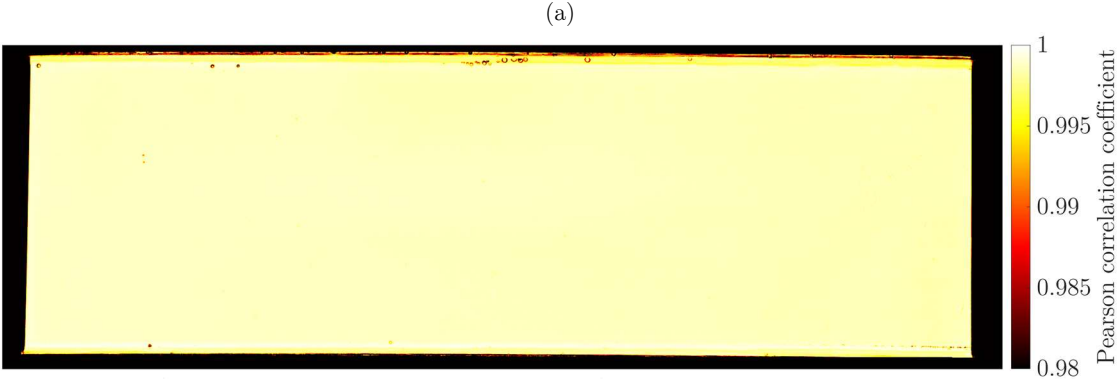


Figure B.3: Plot of the Pearson correlation coefficient of the calibration curves obtained in the far field.

Appendix C: Front detection

The detection performed in the near field of the semi-rough experiments is illustrated in Figure C.1 below.

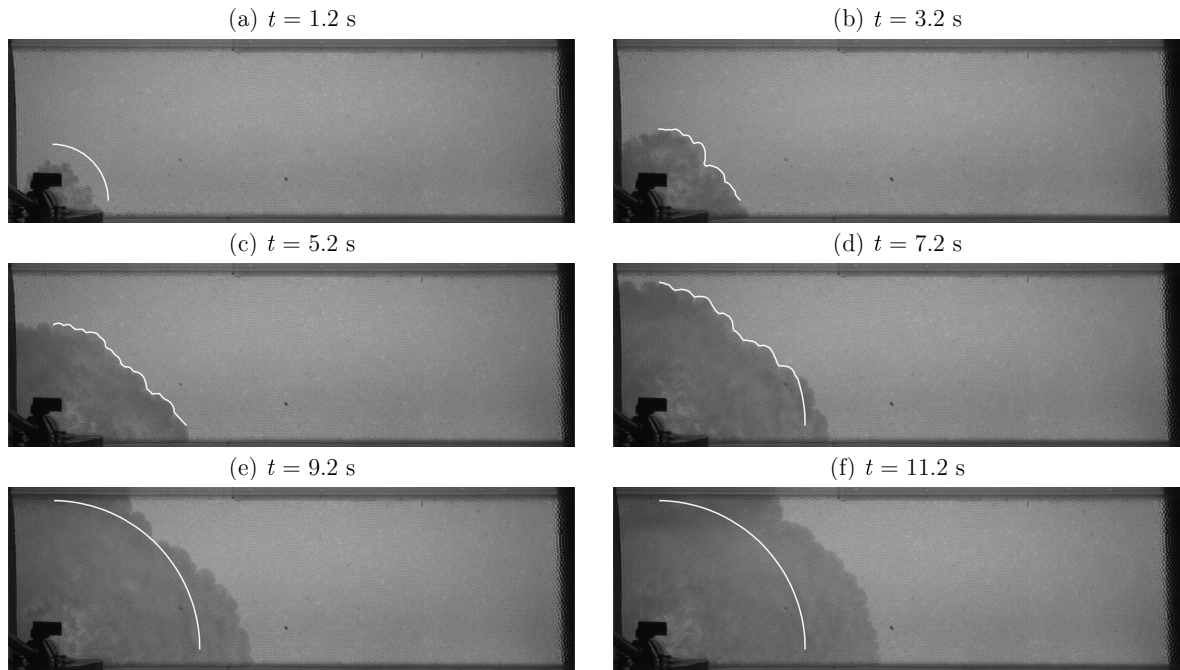


Figure C.1: Front detection in the near field t seconds after the beginning of the discharge (semi-rough bed).

The detection performed in the near field of the multi-rough experiments is illustrated in Figure C.2 below.

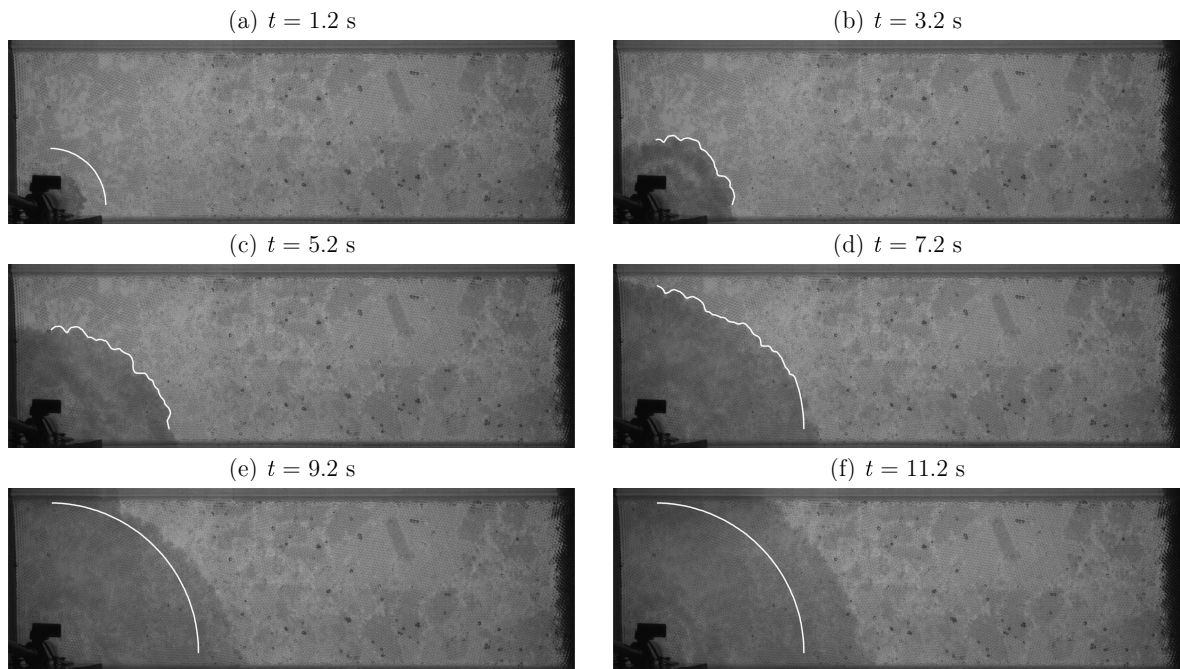


Figure C.2: Front detection in the near field t seconds after the beginning of the discharge (multi-rough bed).

The detection performed in the far field of the semi-rough experiments is illustrated in Figure C.3 below.

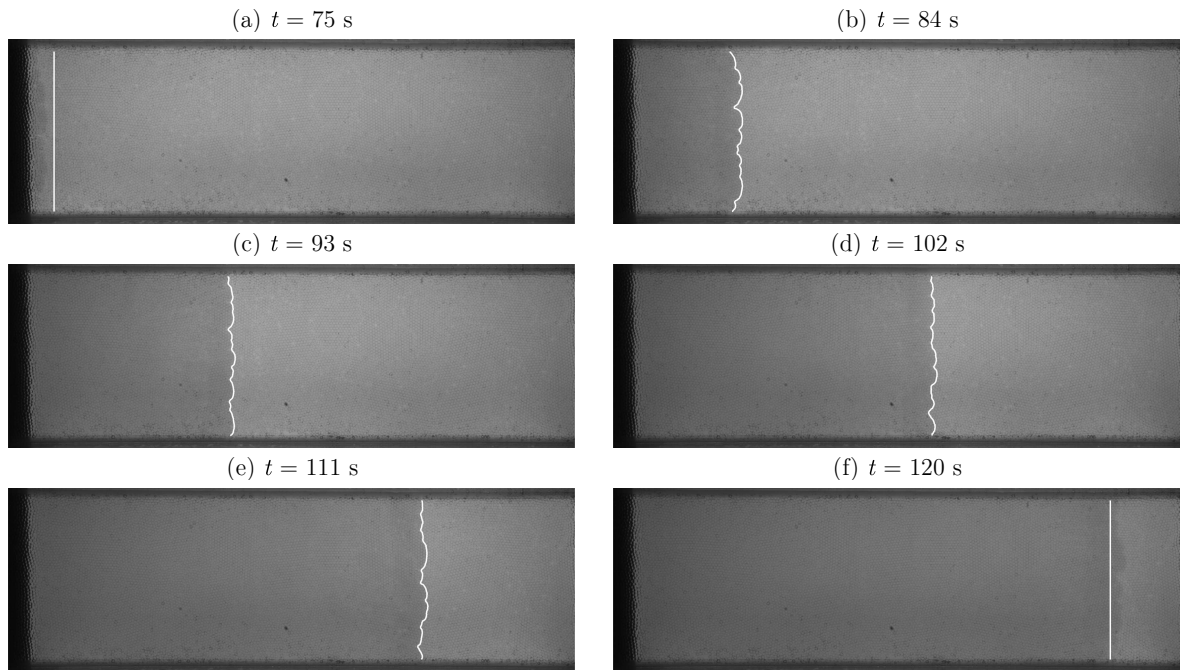


Figure C.3: Front detection in the far field t seconds after the beginning of the discharge (semi-rough bed).

The detection performed in the far field of the multi-rough experiments is illustrated in Figure C.4 below.

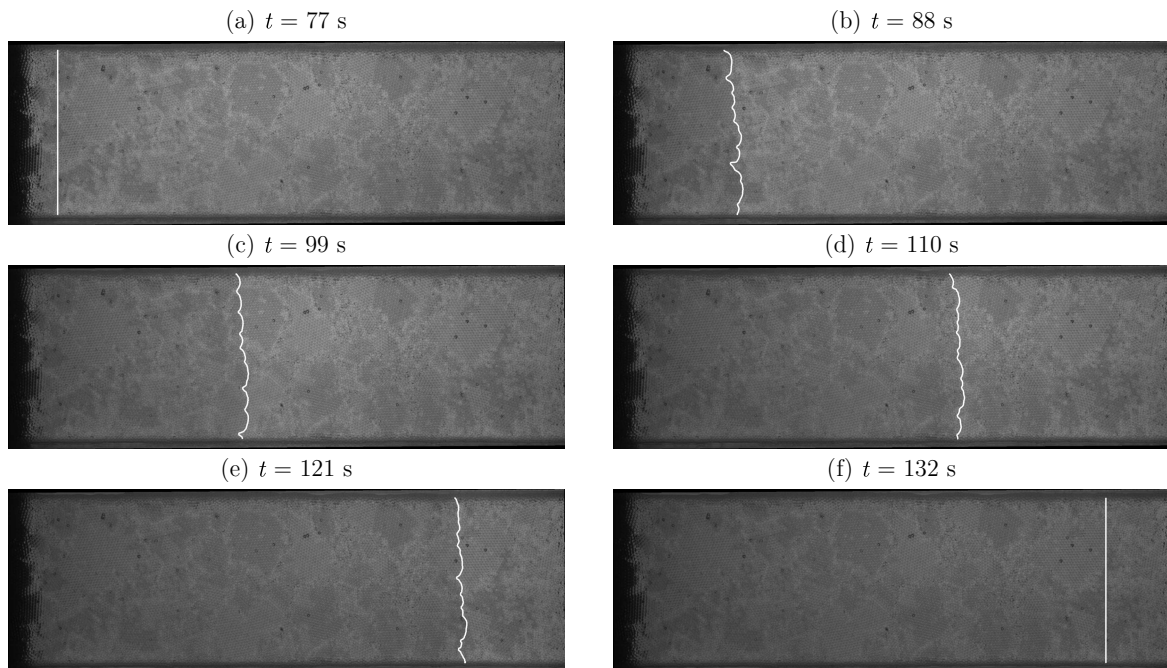


Figure C.4: Front detection in the far field t seconds after the beginning of the discharge (multi-rough bed).